

Thermal history dependent electronic properties of κ -(BEDT-TTF)₂Cu[N(CN)₂]X (X=Br,Cl) near the Mott-metal-insulator transition

Von der thermischen Vorbehandlung abhängige elektronische Eigenschaften von κ -(BEDT-TTF)₂Cu[N(CN)₂]X (X=Br,Cl) nahe des Mott-Metall-Isolator Übergangs

Florian Michael Kollmannsberger

Thesis for the attainment of the academic degree

Master of Science (M.Sc.)

at the Department of Physics of the Technical University of Munich.

Examiner:

Prof. Dr. Rudolf Gross

Supervisor:

Prof. Dr. Rudolf Gross

Submitted:

Munich, 21.08.2023

I hereby declare that this thesis is entirely the result of my own work except where otherwise indicated. I have only used the resources given in the list of references.

Munich, 21.08.2023

Florian Michael Kollmannsberger

Contents

1	Introduction	1
2	Crystal Structure	3
2.1	Crystal Structure of κ -(BEDT-TTF) ₂ Cu[N(CN) ₂]Cl and κ -(BEDT-TTF) ₂ Cu[N(CN) ₂]Br	3
2.2	Occupation of eclipsed and staggered state of the endgroups	4
2.3	Anisotropy of crystal lattice	5
2.4	Fermi surface	5
2.5	Changes of the band structure depending on ordering of endgroups	6
2.6	Phase diagram	7
2.6.1	Similarity between pressure and disorder for moving in the phase diagram	9
3	Theory	11
3.1	Matthiesen's Rule and Drude Sommerfeld model	11
3.2	Mott insulator	12
3.3	Glass model	13
3.4	Shubnikov de Haas oscillations	14
3.4.1	Electrodynamics in a magnetic field	14
3.4.2	Shubnikov-de-Haas oscillations	15
3.5	Theory for U/t change from effective mass	16
4	Experimental methods	19
4.1	Measuring resistance of the samples	19
4.1.1	Naming samples	19
4.1.2	Integrating new lock-in amplifier	20
4.1.3	Problems with auto range on Keithley 2000 multimeters in case of huge changes of resistance with time and temperature and certain resistances	21
4.2	Sample preparation	22
4.3	Thermometry and stabilising temperature	22
4.3.1	Thermometry	22
4.3.2	Comparing thermometers and measuring T _c of Niob	22
4.3.3	Stabilizing temperature	23
4.4	Quenching methods	24
4.4.1	Cooling the sample by turning off the heater	24
4.4.2	Cooling by moving the sample holder	24
4.4.3	Using the sample as a restive heater to heat itself	25
4.5	Heat pulsing	25
4.5.1	Description of the heat pulse setup	26
4.6	He 3 gas system	28
4.6.1	³ He System in Garching	28
4.6.2	³ He system in Dresden	29
4.6.3	Proposed improvement to ³ He system in Dresden	30
4.7	Measuring SdH	31
4.7.1	Characterising samples in Garching	31
4.7.2	Measuring effective electron masses at the high field laboratory in Dresden.	32

4.8	Pressure Cell and He Gas Pressure System	35
4.8.1	The ^4He gas pressure setup	35
4.8.2	The pressure cell	36
5	Experimental Results	39
5.1	Change in resistance over temperature depending on thermal treatment	39
5.2	Annealing and change in resistance	41
5.2.1	Fit with one and two exponentials	41
5.2.2	Annealing rates	41
5.2.3	Annealing under pressure	43
5.2.4	Change of amplitude during annealing	43
5.3	Heat pulses	46
5.3.1	Reversibility of the heat pulse	46
5.3.2	Rates of cooling and heating during and after the heat pulse	46
5.3.3	Achievable disorder depending on the maximal temperature of the heat pulse	47
5.4	Hysteresis in the resistance in the glass transition range	51
5.4.1	Hysteresis in $\kappa\text{-Br}$	51
5.4.2	Hysteresis in $\kappa\text{-Cl}$	54
5.4.3	Change of the hysteresis in $\kappa\text{-Cl}$ under pressure	55
5.4.4	Conclusions on the hysteresis in the glass transition range	55
5.5	$\kappa\text{-Cl}$ under pressure	58
5.5.1	Resistance over pressure at room temperature	58
5.5.2	Resistance over pressure near the superconducting transition	58
5.5.3	Shift in the step in resistance	62
5.5.4	Shift in the hysteresis above superconducting transition upon disordering	63
5.5.5	Shift in the transition between metal and insulator close to the critical point upon disordering	64
5.6	Hysteresis in the resistance above T_c	67
5.7	T_c dependence on thermal treatment	69
5.7.1	T_c value	69
5.7.2	Change in Broadness of transition	73
5.8	Oscillations in magneto resistance	76
5.8.1	Critical field of superconductivity	76
5.8.2	Change in frequency	76
5.8.3	Effective masses	79
5.8.4	Conclusions on measuring effective mass	79
6	Summary and Outlook	83
A	Appendix	85
A.1	Table of Samples	85
A.2	Hints on soldering small wires	85
A.3	Heat pulse program and data evaluation	89
A.3.1	The measurement program.	89
A.3.2	The heat pulse program.	90
A.3.3	The steps when applying a heat pulse	90
A.3.4	Getting from R(time) to T(time)	91
A.4	Remainder of figures from $\kappa\text{-Cl}$ under pressure	97
	Bibliography	103

1 Introduction

Mott insulators are interesting compounds, as in these materials under conditions, where one would expect a metal from standard band theory, one finds instead an insulator. A Mott insulator is a prominent manifestation of strong electron correlations as these strong correlations in combination with half filling of the band and a small bandwidth lead to the insulating state. These strong correlations go beyond the standard Fermi liquid model. This then leads to exotic states in cuprate superconductors and organic metals near the Mott instability like unconventional superconductivity and quantum spin liquids. As of today, the evolution of the charge carrier properties and correlations upon approaching the Mott-metal-insulator-transition (MIT) from the metallic side is not really settled. There are many theories[1, 2, 3, 4] trying to predict the charge carrier properties, however, there is a lack of systematic experimental studies in the vicinity of the MIT, to verify these theories. Recently Oberbauer et al. [5] performed a systematic study of magnetic-quantum-oscillations in κ -(BEDT-TTF)₂Cu[N(CN)₂]Cl (short κ -Cl) in close proximity to the MIT. They found magneto-quantum oscillations near the MIT in the organic charge transfer salt κ -Cl, where BEDT-TTF stands for bis(ethylenedithio)-tetrathiafulvalene. Magneto-quantum oscillations are a very useful probe of the electronic properties, among others of the effective cyclotron mass of the charge carriers. The renormalized effective mass of the charge carriers then can be used as a measure of the correlation strength. One of the advantages of using organic charge transfer salts like κ -Cl is that by physical pressure, one can easily tune the ratio U/W, with repulsion strength U and bandwidth W as shown by Limelette et al. [6].

The ethylene endgroups in the BEDT-TTF molecule have two possible conformations, where the conformation can be frozen in when going through a glass transition, as shown by Su et al. [7]. The way one approaches and cools through the glass transition, which we call thermal history, then determines the frozen-in conformation. Hartman et al. [8] among others gave evidence, that through different thermal histories, one can move the materials in the phase diagram of the κ -(BEDT-TTF)₂X salts. Hartman et al. [8] argue that the change in the phase diagram acts the same way as reducing the hydro-static pressure applied to the sample. We therefore now want to study in this thesis the effect of the thermal history on electronic properties in κ -(BEDT-TTF)₂Cu[N(CN)₂]Br (short κ -Br), which lies on the metallic side of the MIT opposite to κ -Cl. There have been some reports [8, 9, 10] among others, on κ -Br, but mostly for the deuterated version of κ -Br, where the hydrogen atoms in BEDT-TTF have been replaced by deuterium atoms. We now want to study the effects of the thermal history on the resistive properties and the superconductivity as κ -Br is an ambient pressure superconductor. We further want to take a further insight into magnetic quantum oscillations especially into the carrier effective cyclotron mass. To do this we want to study the thermal history effects over the accessible range, from the as-good-as-possible ordered conformations of the ethylene endgroups to generating the strongest disordered conformations by reproducing and further optimizing the heat pulse technique invented by Hartman et al. [8]. For κ -Cl we want to study the effect of disordering on the position of the material in the phase diagram. κ -Cl has the advantage that one can tune the ground state by pressure by applying only a few hundred bar. κ -Cl is an insulator at ambient pressure but can be turned into a metal upon applying a hydro-static pressure of 200 bar according to our measurements and [11]. Further we want to study the relaxation rates at the glass transition to prepare future experiments on the effects of thermal history in κ -Cl.

2 Crystal Structure

2.1 Crystal Structure of κ -(BEDT-TTF)₂Cu[N(CN)₂]Cl and κ -(BEDT-TTF)₂Cu[N(CN)₂]Br

To understand the nature of the compounds discussed in this thesis, we first look at their crystal structure and components. Figure 2.1 shows the crystal structure of the two compounds κ -(BEDT-TTF)₂Cu[N(CN)₂]Cl and κ -(BEDT-TTF)₂Cu[N(CN)₂]Br. For simplicity we will from now on abbreviate them by κ -Cl and κ -Br.

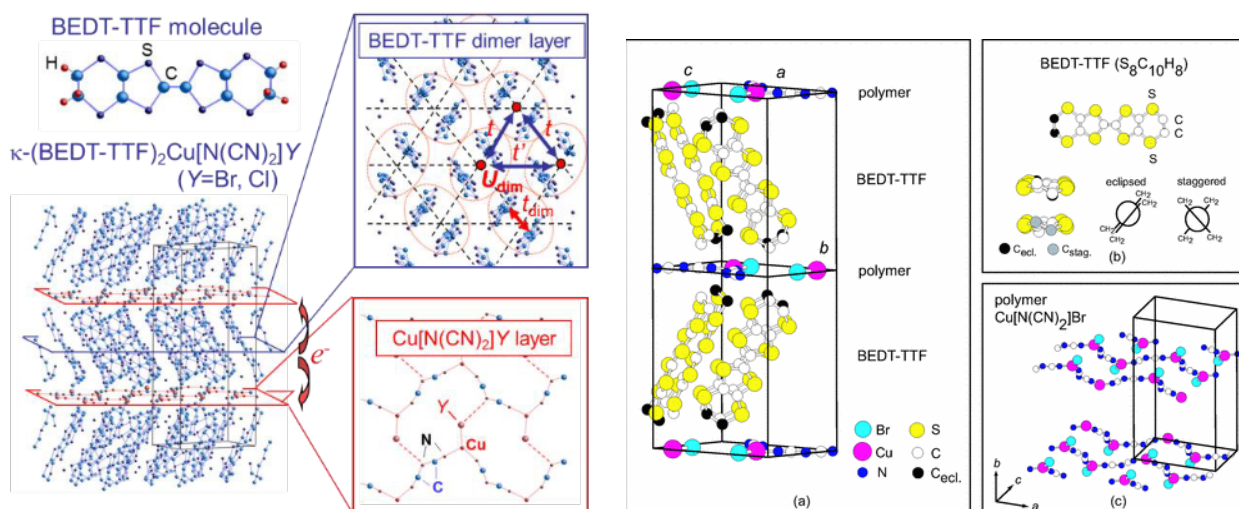


Figure 2.1 Left: Crystal structure of κ -(BEDT-TTF)₂Cu[N(CN)₂]Y, where Y = Br or Cl, from Sasaki [12]. **Right:** Changes in the conformation of the ethylene end groups and the surroundings of the end groups from [13]

The κ -Br and κ -Cl structures we investigate are crystals made from alternating layers of bis-ethylenedithiotetrathiafulvalene (BEDT-TTF or ET) molecule dimers and polymeric anion Cu[N(CN)₂]Y. The ET molecules form an an-isotropic triangular lattice, from Wolter et al. [12]. The lattice parameters at room temperature for κ -Br are $a(\text{\AA}) = 12.942$, $b(\text{\AA}) = 12.884$, $c(\text{\AA}) = 12.869$, with the unit cell volume $V(\text{\AA}^3) = 3315$, from Wolter et al. [13]. The central two C atoms as well as the C-C bonded atoms that are solely connected S atoms are connected by a double bond. Together with the S atoms the C atoms form rings in which the s- and p-orbitals are hybridised to form σ and π molecular orbitals. The σ orbitals are located in the plane of the molecule while the π orbitals are parallel to the plane of the molecule. The π orbitals form a system of delocalized electrons and due to their overlap with the neighboring dimmers then form electron bands. The electrons from the bands are partially transferred to the accepting anion, leading to a partial filling of the band. The anions have closed electron shells, therefore no partially occupied bands, and therefore do not contribute to the conductivity. The electron movement is therefore restricted to the layers of the ET molecules, with hopping in between the layers.

Looking at the right side of figure 2.1, we see that the ethylene endgroups of the ET molecules can have different orientations relative to each other. We have the staggered conformation where the C-C bonds of the ethylene endgroups are at an angle to each other and the eclipsed conformation where the C-C bonds of the endgroups are parallel to each other. Guterding et al. [14] report that which conformation of the ethylene endgroup is lower in energy depends on the halogen atom in κ -(BEDT-TTF)₂Cu[N(CN)₂]Y, where for Y = Cl and Y = Br the eclipsed state is the ground state. Further they report that they found

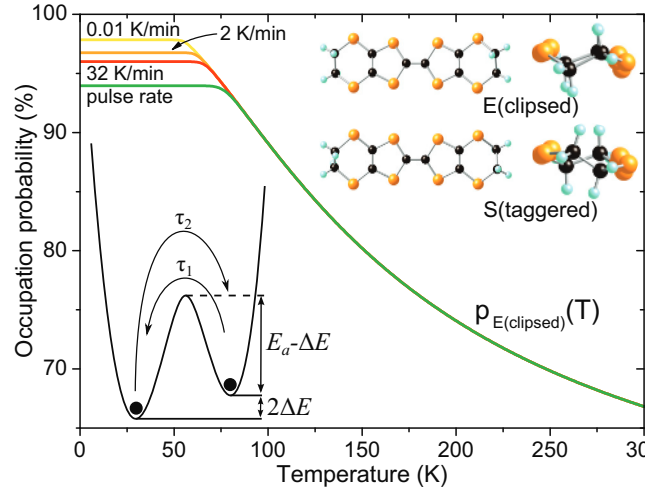


Figure 2.2 From [8]

via density functional theory (DFT) calculations that the energy difference between eclipsed and staggered state is 72 meV for κ -Cl and 110 meV for κ -Br.

2.2 Occupation of eclipsed and staggered state of the endgroups

Hartman et al. [8] discuss the occupation probability of the eclipsed ground state and the excited staggered state of the ethylene endgroup. For a description of the occupation probabilities we will follow their paper. They give the occupation probability of the eclipsed ground state in the thermal equilibrium by

$$\rho_E^\infty(T) = \frac{1}{1 + e^{-\frac{2\Delta E}{k_B T}}} \quad (2.1)$$

in the double well potential shown in Fig 2.2. ΔE is the energy difference between ground and excited state. When in a non thermal equilibrium the system relaxes back to equilibrium with the effective rate

$$\tau_{eff} = \left(\frac{1}{\tau_1} + \frac{1}{\tau_2} \right) = v_0^{-1} e^{\frac{E_a}{k_B T}} \left(e^{\frac{\Delta E}{k_B T}} + e^{-\frac{\Delta E}{k_B T}} \right)^{-1}, \quad (2.2)$$

where E_a is the energy barrier between ground and excited state and v_0^{-1} the attempt frequency, which they say is usually associated with phonon frequencies.

This now allows to state the time dependent occupation probability of the eclipsed state when rapidly changing the temperature from T_0 to T_1

$$\rho_E(t) = \rho_E^\infty(T_1) - [\rho_E^\infty(T_1) - \rho_E^\infty(T_0)] \cdot e^{-\frac{t}{\tau_{eff}}}. \quad (2.3)$$

We can see from fig.2.2 that 90% of the ethylene end-groups are in the ground state at the glass transition for κ -Br. Guterding et al. [14] report that 20% of the ethylene end groups at room temperature are in the excited state for κ -Cl. As most of the ethylene endgroups are in the eclipsed ground state for low temperatures, we can treat the ethylene endgroups in the excited staggered state as defects. As Müller et al. [15] report there is a glass transition in κ -Br and κ -Cl where the ethylene endgroups freeze in in their conformation. Down to the glass transition the ethylene endgroups relax quickly to the ratios given by formula 2.1, however these dynamics decrease once reaching the glass transition. However at the glass transition the endgroups still can be ordered by keeping the sample at certain temperatures around the glass transition for an adequate amount of time, as shown in equation 2.3. This process we call annealing or ordering. The opposite process of decreasing the amount of ethylene endgroups in the ground state we call quenching or disordering.

2.3 Anisotropy of crystal lattice

We now want to discuss the basic parameters as transfer energy, Coulomb repulsion and bandwidth W , following Sasaki [12]. The natively quarter filled band is modified to an effective half filled band, arising from the strong dimer structure of the two ET molecules. The intradimer transfer energy t_{dim} is bigger than the interdimer transfer energies t and t' . The anisotropy of the triangular lattice of the dimers then changes with the ratio t/t' . It can be considered as a measure for the frustration of the triangular lattice. For κ -Br we have a ratio of t/t' of 0.7. κ -Br and κ -Cl are strongly correlated electron system, where several electronic and magnetic phases appear, as shown in section 2.6. These transition between these phases are controlled by the applied pressure and the chemical substitution of donor and anion molecules. This changes the conduction band width $W \sim 4t$ with respect to the effective Coulomb repulsion U_{dim} of a dimer. The value of the repulsion U_{dim} is estimated to approximately $U_{dim} \sim 2t_{dim}$. The value of U_{dim} is then about 0.4 eV for $t_{dim} = 0.2$ eV. This value of U_{dim} is comparable to the bandwidth $W \sim 4t$. This suggests that electron correlation effects are important. The strength of the electron correlations relative to the bandwidth can be controlled either by applying low pressure on the order of hundreds of bar or by substituting molecules partially. This can lead to a Mott insulator in case of $Y = Cl$ or a metal and superconductor in case of $Y = Br$, with a metal insulator transition in between. Sasaki [12] now suggests that molecular conductors with strongly correlated electrons can become potential candidates for investigating the randomness effect. This is to be done by developing an experimental method for introducing disorder into the crystals without modifying the electronic state. Only the scattering rates are changed. It was found by X-ray irradiation of κ -Br, that the Anderson localization insulating state, can be introduced by weak molecular disorder in the strongly correlated metallic/superconducting state, as shown by Sano et al. [16].

Müller et al. [17] report that

- the anisotropic change of in-plane lattice parameters at T_g , at the glass transition results in a smaller average ratio t_{inter}/t_{dim} of the inter- and intra-dimer transfer integrals for more rapid cooling, which in turn leads to a smaller effective W/U . Here t_{inter} is t and t' . This means that the strength of electronic correlations can be controlled by varying the degree of frozen-in disorder at T_g . The freezing of the structural degrees of freedom causes a decrease of the electronic bandwidth W with increasing cooling rate. This means that a Mott-metal-insulator transition can occur for a metallic system, when crossing the critical ratio $(W/U)_c$ of bandwidth to onsite Coulomb repulsion U . At the glass transition, the conformation of the ethylene endgroups is frozen in, therefore persists below T_g , but can be reversed when going near to or above the glass transition. This then allows to fine tune materials across the Mott-metal-insulator transition.
- The strong vibrations of the ethylene endgroups lead to an enhanced scattering contribution at temperatures above the glass transition. The frozen in configuration below T_g , is then a random lattice potential. This gives rise to an additional contribution to the residual resistivity and affects the superconducting state and transition temperature. The influence of the disorder from the ethylene endgroups on the strongly correlated π -carriers, then results in a Mott-Anderson transition.

2.4 Fermi surface

We want to have a look at the Fermi surface. For this we follow Weiß [9].

We have two open, slightly warped electron-like sheets normal to the k_c -axis. Further we have a cylindrical hole-like surface, along the k_b direction, where the elliptical cross section area is centered at X. Weiß reports that two main contributions to magneto-quantum oscillations should appear

- Oscillations of a frequency corresponding to the area encircled by the closed elliptical orbit. This orbit encompasses around 14% of the first Brillouin zone cross section area. It is named α -orbit by convention.

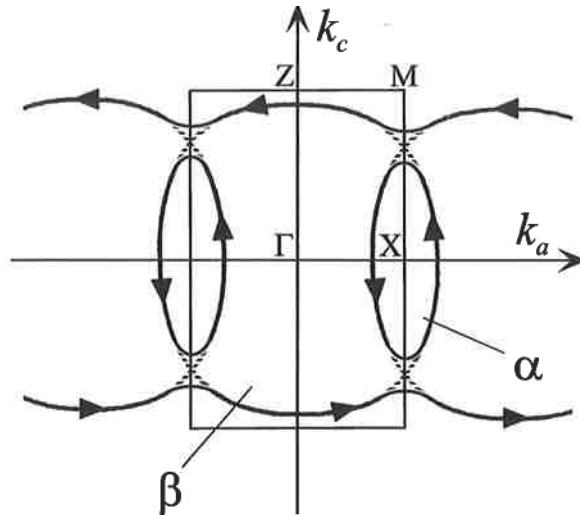


Figure 2.3 The Fermi surface of κ -Br from Weiß [9]

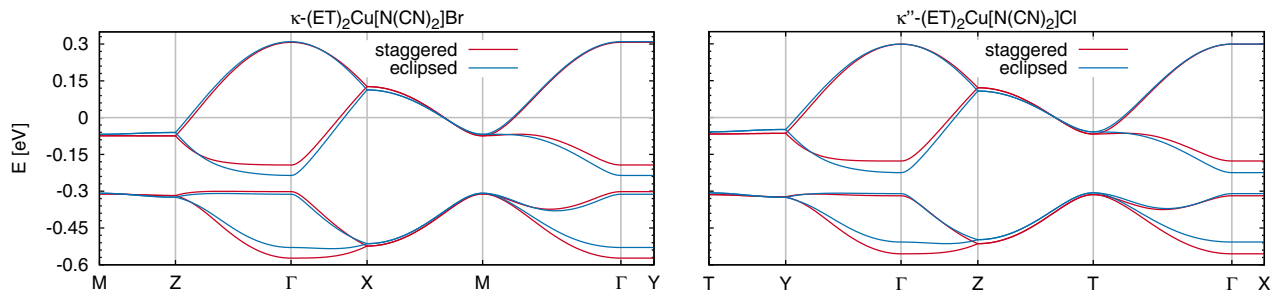


Figure 2.4 Change of the band structure from Guterding et al. [14]. We see that the bands change far away from the

- Oscillations with a frequency corresponding to 100% of the first Brillouin zone cross section area. This orbit is created by magnetic breakdown, which allows the electrons to overcome the gaps at the boundary of the first Brillouin zone, for sufficiently high magnetic fields. In case where the in-plane anisotropy can be ignored, it has perfect circular shape. This orbit by convention is named β -orbit. From a very strong anisotropy of the Fermi surface, the quasi-two-dimensional metals based on BEDT-TTF exhibit a strong enhancement of the magnetic breakdown manifestation. As the transverse bandwidth is expected to be much smaller than the magnetic breakdown gap, the magnetic breakdown orbit is expected to give the dominant contribution to the magnetic quantum oscillations.

Weiß claims to have been the first to measure these oscillations.

2.5 Changes of the band structure depending on ordering of endgroups

We want to briefly discuss the changes in the band structure depending on the change of the conformation of the ethylene endgroups following Guterding et al. [14]. They calculate the band structure using *ab initio* density functional theory (DFT) calculations, with full-potential local orbital basis to calculate the electron band structure. For the exchange correlation function they used the generalized gradient approximation (GGA). They find that for the ethylene endgroups for κ -Br and κ -Cl, the eclipsed conformation is the groundstate. The difference in the band structure between the compounds with eclipsed and staggered conformation is shown in fig. 2.4. The difference between both configurations lies in the electronic bandwidth. When going from eclipsed to staggered, the overall bandwidth increases, while in contrast the width

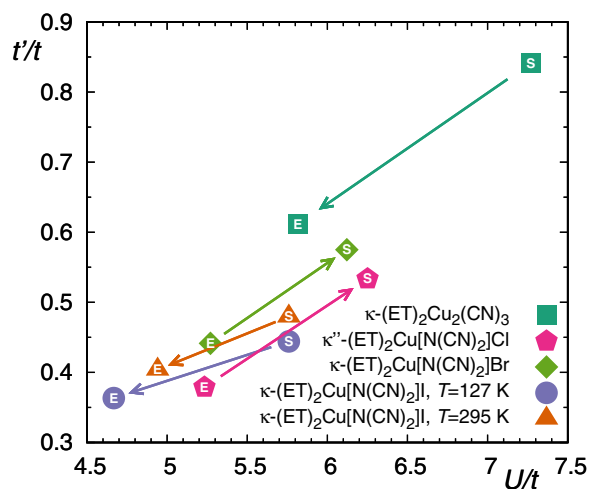


Figure 2.5 Change in U , t and t' from Guterding et al. [14]

of the two bands closes to the Fermi level decreases. This is very interesting for us as this predicts that increasing the amount of ethylene endgroups in the excited staggered state, decreases the bandwidth.

From their DFT calculations Guterding et al. then further estimated the change in the Hubbard model parameters t , t' and U , which we discussed earlier. We see that changing from eclipsed to staggered configuration for κ -Cl and κ -Br, increases both the frustration t'/t and the relative strength of the Hubbard repulsion U/t . They conclude from this that κ -Br can be tuned into a Mott insulator by getting ethylene endgroups from the eclipsed ground state into the staggered excited state. This then increases U/t and as κ -Br is already close to the Mott metal insulator transition this then may bring the compound over the phase transition line into the insulating state. Hartman et al.[8] showed experimentally that this is possible for a partially deuterated κ -Br sample. (Partially-) Deuterated κ -Br is closer to the Mott metal insulator transition as shown by Sasaki et al. [18].

2.6 Phase diagram

At ambient pressure κ -Cl is an insulator while κ -Br is a metal both, as shown in fig. 2.6. Both are separated by the Mott metal insulator transition. We now want to discuss the different phases close to the metal insulator transition.

In the upper left of fig. 2.6 in (a) we see the phase diagram drawn by Hartman et al. [8]. They show that by changing pressure, they can move κ -Cl from the insulating state to the metal state. Moving from the insulating to the metallic state can also be achieved by changing the halogen in the anion from Chlorine to Bromine, which is therefore called "chemical pressure". They further show that by substituting the hydrogen atoms with deuterium atoms, they can move κ -Br closer to the metal insulator transition. Deuterating the samples then acts as a negative "chemical pressure". They claim that by ordering and disordering the ethylene endgroups in the organic molecule ET they can also create "negative pressure". This will be discussed in detail in subsection 2.6.1. On the upper right of fig. 2.6 in (b) we see a pressure-temperature-resistance diagram from Kagawa et al. [19]. They labeled each region observed in the diagram accordingly. Noticeable is a double step feature in the resistance of the pressure sweeps (blue lines) which is also visible in the temperature sweeps (red lines). This double step feature occurs at the transition from metal to insulator. An explanation may be found in the lower right of fig. 2.6. There anomalies in the sound velocity are shown which Fournier et al. [21] attribute to anomalies in the compressibility of electronic degrees of freedom which then can lead to anomalies in the resistance. Kagawa et al. and Fournier et al. report that these step anomalies end at the critical point at 38.1 K and 232 bar. Above this point the change in

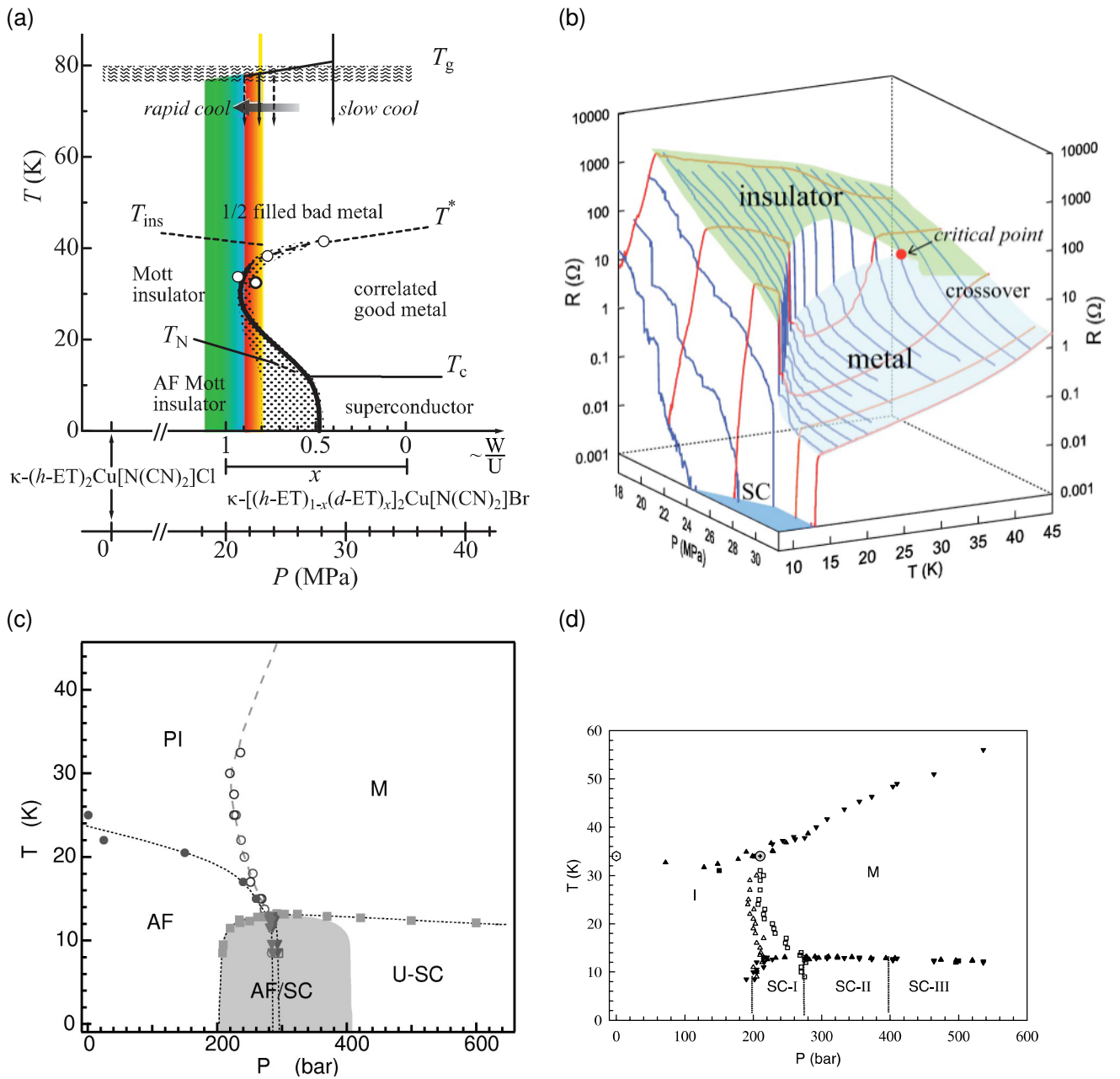


Figure 2.6 Phase diagrams and plots of features in resistance for κ -Cl and κ -Br. All phase diagrams are temperature over pressure **Upper left, (a)**: From [8], showing to which pressure the changes in chemical composition of the κ -Cl - κ -Br system, can be related. Also includes the effect of cooling rate which they investigated. **Upper right, (b)**: Resistance behaviour of κ -Cl over pressure and temperature from [19]. **Lower Left, (c)**: Phase diagram temperature over pressure of κ -Cl from [20], naming the different phases. **Lower right, (d)**: Anomalies in the sound velocity, from [21]. They attribute these changes in sound velocity to changes in the electron compressibility.

resistance is no more step like. It may be that the findings of Kagawa et al. and Fournier et al. are based on different effects, but that would rise the question how one can occur without the other. Fournier et al. report that they found three different phases of superconductivity, where they say that the anomalies between 12 and 30 K are an extension of the superconducting phase boundary of SC-I. They report that their measurement is not sensitive enough to detect the antiferromagnetic (AF) phase boundary shown in the lower left of fig. 2.6. Lefebvre et al. report an antiferromagnet (AF) and paramagnetic insulating (PI) region on the lower pressure side of the metal insulator transition line marked by the open circles. On the other side is the metallic (M) region above a region of either unconventional superconductivity (U-SC) or an antiferromagnetism superconductivity coexistence region (AF/SC). In the AF/SC region the superconductivity is suppressed with decreasing pressure, which gives a region of in-homogeneous phase coexistence. This region is made from the SC-I and SC-II phases Fournier et al. [21] report.

2.6.1 Similarity between pressure and disorder for moving in the phase diagram

We have seen that we can move in the phase diagram by either applying pressure or by chemical substitution. Hartman et al. [22] claim that they have found another method to move in the phase diagram. Their approach is that by ordering or disordering the ethylene endgroups they change state state of their sample as if they applied or reduced pressure. To show this they took a sample that consisted of 80 % fully deuterade ET molecules and 20 % fully hydrogenated ET molecules. This sample they heated with a voltage pulse that heats the sample above the glass transition range. This voltage pulse then is turned off to allow the sample to quickly cool down and freeze in the disorder at the final temperature of the heat pulse. The resulting disorder is the disorder of the ethylene endgroups that did not relaxed during the fast cooling. By gradually relaxing the sample for 2 min at 70 K, which is below but close to the glass transition they created a series of temperature sweeps for different ammounts of disorder, shown on the left in fig 2.7. They estimate that the amount of the ethylene endgroups in the eclipsed ground state is 94 % after the heat pulse compared to 98 % for the slowly cooled state.

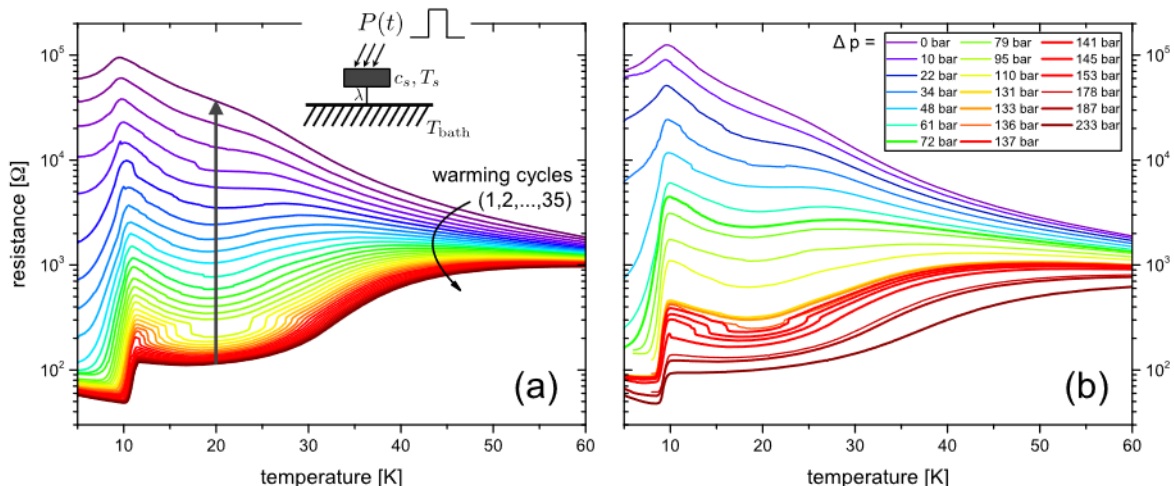


Figure 2.7 From [22]. **Left, (a):** The resistance measurements over temperature for for different amounts of disorder. The heat pulsed state of the sample has crossed into the insulating region of the phase diagram. **Right, (b):** Resistance measurements for different pressures with the sample prepared by the same heat pulse as the initial highest disordered state in (a). The other resistance curves were then prepared by increasing the pressure. This then brought the sample back into the metallic region of the phase diagram

From the measurements shown in fig. 2.7 they mapped then pressure to disorder, estimating to get a "negative" pressure amounting to 200 bar. Negative here means that disordering the system moves the sample in the phase diagram to lower pressure states. This is, as they state, remarkable as this pressure effect is achieved by a change in occupation probability of the eclipsed ground state from 98 % to 94 %.

We will try in this master-thesis, to use this effect to move fully hydrogenated κ -Br samples closer to the metal insulator boundary.

3 Theory

3.1 Matthiesen's Rule and Drude Sommerfeld model

For analysing the resistance and the change of resistance by the thermal treatment, we want to investigate the different contributions to resistance separately. Gross and Marx show in their book on solid state physics [23, p. 410] that indeed this is possibly by the so called Mathiessen rule. For the details we follow [23, p. 410].

The different types of scattering have each their density n_S and their scattering cross section S . The mean free path is as in optics then $1/l = n_S S$. In the case that different independent scattering processes are present, each with their own density $N_{S,i}$ and cross section S_i , then the inverse free path length is

$$l^{-1} = \sum_i n_{S,i} S_i \quad (3.1)$$

The inverse free path length is proportional to the resistance R , by the Drude Sommerfeld model [23, p. 296]

$$R = \frac{m v_F}{n e^2 l}, \quad (3.2)$$

where m is the electron mass, v_F the Fermi velocity, n the electron density and e the electron charge.

Combining this we get

$$R = \sum_i R_i. \quad (3.3)$$

Using this theory from Gross and Marx we can find the resistance contribution from the disordering of the ethylene end-groups.

The density of defects from the ethylene end-groups is $(1 - \rho_E(T, t) / \rho_{EEG})$ as in the perfectly ordered crystal all end-groups would be in the ground state, where $\rho_E(T, t)$ is the time dependent density of the ethylene endgroups in the eclipsed state and ρ_{EEG} is the density of the ethylene endgroups. We can see from fig. 2.2 that 90 % of the ethylene end-groups are in the ground state at the glass transition for κ -Br. Guterding et al. [14] report that 20 % of the ethylene end groups at room temperature are in the excited state for κ -Cl. Therefore the end-groups in the excited state are in the minority and can be seen as defects.

Therefore the fraction of the end-groups that is not in the eclipsed ground state are the defects, with the density of ethylene end-groups ρ_E and the thermal history dependent $\rho_E(T, t)$ number of ethylene end-groups in the eclipsed state.

Using equation 2.3 we can write the time dependent resistance when quickly changing from T_0 to T_1

$$R(t, T) = c \cdot \left(1 - \left(\rho_E^\infty(T_1) - [\rho_E^\infty(T_1) - \rho_E^\infty(T_0)] \cdot e^{-\frac{t}{\tau_{eff}}} \right) / \rho_E \right) + \sum_i R_i(T) \quad (3.4)$$

with c a constant accounting for the scattering cross section. The sum over the $R_i(T)$ is over all the other scattering contributions except the ethylene end-groups. This now allows to fit τ_{eff} from the time dependent resistance.

3.2 Mott insulator

We now want to briefly introduce the Mott insulator following F. Gebhards book [24]. We start with the gap criterion for an insulator, 1.1.3 in Gebhards book. He states two fundamental requirements for electron transport in Fermi systems derived from a Kubo formula for the current-current correlation function. The correlation function probes the (collective) propagation of an electron-hole excitation of the system at a fixed electron number. Two fundamental requirements for electron transport in Fermi system can be uncovered by this analysis:

- Quantum-mechanical states for electron-hole excitations must be available at energies infinitesimally above the ground state energy. This is as, the external field provides arbitrary small energy, which could be used to reach a state at an energy above the ground state. A gap would then mean that there is an onset field required for conductivity where the field provides the energy necessary to reach the electron hole excitation.
- The electron-hole excitations must be delocalised charges that can contribute to transport over the entire macroscopical sample size.

If both conditions are fulfilled then the ground state is metallic. Many physical phenomena can be described with the assumption of independent electrons, e.g. the de-Haas-van-Alphen effect and a lot of other experiments at the Fermi surface in metals. However if we want to understand Mott insulators we need electron electron interactions. That we can assume independent electrons comes from two observations:

- In systems with delocalized electrons the Coulomb interaction between the charge carriers is very effectively screened. The screening length lies in the range of the inverse Fermi wave number k_F^{-1} , it is only on the order of Ångströms.
- If a Fermi surface exists, then the scattering rate between electrons near the Fermi surface with energy $E_F + w$, vanishes proportional to w^2 . This is as the Pauli principle strongly reduces the number of scattering channels that are compatible with both, energy and momentum conservation.

The second principle allows for Landau's Fermi liquid theory. If a Fermi surface exists for the interacting Fermi system, as it did for the non interacting Fermi system (Fermi gas), then the excitations near the Fermi surface are long living Fermions, so called Landau quasi-particles. These particles have a one-to-one correspondence to the electron and hole excitations of the Fermi gas. Gebhard then explains in detail how Fermi liquid and Fermi gas can be mapped onto each other. Fermi liquid theory and Fermi gas theory both describe metals. To get to an insulator these concepts have to break down. On the basis of physical grounds we can argue that the Fermi liquid picture provides a self-consistent description of the influence of electron-electron interactions in metals:

- the electrons are highly mobile in the crystal, therefore
- their mutual interaction is well screened, which allows us
- to apply Fermi liquid theory. This then implies
- that the remaining screened electron-electron interactions do not qualitatively change the picture.

This concept of dynamic self-screening of delocalised electrons plays an important role in metals. We can non the less not neglect the electron-electron interactions, as they keep each other at distance, while the electrons kinetic energy spreads them out over the crystal.

To understand this we want to have a look at the model for electrons in narrow bands by Hubbard [25]. His central equation is a tight binding model with fermionic ladder operators, $c_{i,\sigma}^\dagger$ creates an electron at site i with spin σ and the annihilation operator $c_{i,\sigma}$ which destroys an electron at site i with spin σ . If the creation of an electron is not possible as this would violate the Pauli principle or if the annihilation is not

possible if there is no electron to annihilate then the state is destroyed. Due to the narrow band, only two electrons are allowed per site. Hubbards main equation is then

$$H = U \sum_i c_{i,\uparrow}^\dagger c_{i,\uparrow} c_{i,\downarrow}^\dagger c_{i,\downarrow} - t \sum_{\langle i,j \rangle, \sigma} \left(c_{i,\sigma}^\dagger c_{j,\sigma} + c_{j,\sigma}^\dagger c_{i,\sigma} \right) \quad (3.5)$$

where U is the repulsion strength and t the hopping parameter or hopping energy. $c_{i,\sigma}^\dagger c_{i,\sigma}$ is the number operator $n_{i,\sigma}$, that counts the number of electrons at site i with spin σ . $c_{i,\sigma}^\dagger c_{j,\sigma}$ is the hopping operator that transports an electron with spin σ from site j to site i . The sum for the repulsion is only for each site and excludes nearest neighbor repulsion. The sum $\langle i, j \rangle, \sigma$ is then over the (nearest) neighbors and both spins \uparrow, \downarrow . The repulsion term $U \sum_i c_{i,\uparrow}^\dagger c_{i,\uparrow} c_{i,\downarrow}^\dagger c_{i,\downarrow}$ increases the energy of a state for each double occupied atom which is the representation of the Coulomb repulsion, which tries to separate the electrons. The transport term $t \sum_{\langle i,j \rangle, \sigma} \left(c_{i,\sigma}^\dagger c_{j,\sigma} + c_{j,\sigma}^\dagger c_{i,\sigma} \right)$ decreases the energy of a state by delocalizing the electrons. This is the kinetic energy that tries to spread the electrons over the sample.

If we now have half filling of the band which we have in our κ -Br and κ -Cl then for infinite repulsion strength we have each electron confined to one atom in the ground state. For $U = 0$ eV we get a completely delocalised electron gas. This this, by continuity implies that for some ratio of U/t there has to be a transition from the state with each electron confined to an atom, to a state with delocalised electrons. This then is a metall-insulator transition, which is according to Gebhard [24] the Mott metal insulator transition. For fillings away from half filling, this argumentation would not hold anymore as even for very large U we have at least one electron or one hole, therefore the ground state has to have an electron or hole that can hop around without a constant contribution from the repulsion term. In a real crystal we can change U/t by hydro-static pressure, chemical substitution, by changing the bandwidth and by disordering the ethylene endgroups.

3.3 Glass model

We want to give a brief introduction into the theory of the glass transition following Scherer [26].

At first we want to introduce the so called fictive temperature T_f . In glass or anything that undergoes a glass like-transition, we have the degrees of freedom that freeze out due to the glass transition, which we for short call glass degrees of freedom. In a material that has this transition, we then can define two temperatures. The thermodynamic temperature T that can be measured via a thermometer and the temperature to which the order and disorder in the glass degrees of freedom correspond to. The latter temperature is called the fictive temperature T_f . The fictive temperature identifies, the temperature from which one must quench a state to get a particular value of a property p . If we are far above the glass transition, where the relaxation is fast, we have quasi immediate relaxation of the glass degrees of freedom and therefore $T = T_f$. When reaching the transition range T_f begins to decrease slower than the change in temperature. For a higher cooling rate the departure from equilibrium is at a higher cooling rate and therefor the property is frozen in corresponding to a higher value, which results in a higher T_f as depicted schematically in fig. 3.1.

We have two definitions for T_g :

- The temperature where the relaxation time is around 100 s according to Hartman et al. [8] and Scherer [26].
- The temperature to which the fictive temperature freezes in, on cooling, according to Scherer [26].

These definitions might seem very different at the first glance but, when the cooling rate of a sample is on the order of 1 K/min to 2 K/m then the sample stays needs 30 s to 60 s for each Kelvin. This means that the relaxation rate is comparable to the cooling time. As Scherer shows, the relaxation rate grows exponentially with decreasing temperature around the glass transition, therefore below the temperature T_g according to the first definition, there will not be much relaxation happening at these cooling speeds

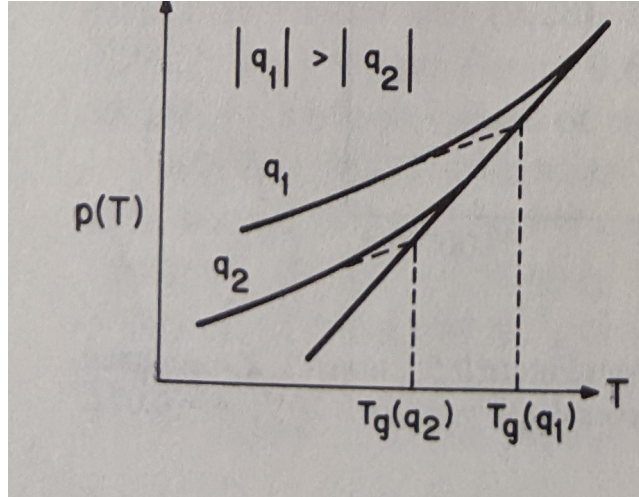


Figure 3.1 From Scherer [26]

and the glass degrees of freedom will in about correspond to the temperature where the relaxation rate is 100s. With a lower or higher cooling rate this temperature can be lowered or raised. This then allows to fine tune the glass transition.

3.4 Shubnikov de Haas oscillations

3.4.1 Electrodynamics in a magnetic field

For an introduction to Shubnikov-de-Haas oscillations we will follow Kartsovnik [27]. For further and in-dept theory there is Abrikosov [28] and Shoenberg [29].

We consider the electrons in the vicinity of the Fermi level E_F , which are responsible for the conductive properties. We further make the simplification that the scattering processes can be approximated by introducing a constant relaxation time τ . We assume it to be independent of the electron's momentum and magnetic field. This τ -approximation is not always justified, as we will see later, when we discuss the scattering probability of the charged carriers depending on the states an electron can be scattered into. We will show during this subsection that the number of states depends on the magnetic field. In a magnetic field B the conducting electrons in a metal feel the Lorentz force

$$F_L = \frac{dp}{dt} = ev \times B, \quad (3.6)$$

where p is the electron momentum, v the velocity and e the charge of the electron. From equation 3.6 we see that the magnetic field only affects the momentum perpendicular to the field, while the component parallel to the field is constant. For low fields, the change in the momentum during the scattering time is minimal, as the curvature of its trajectory is rather small. The radius of the curvature is the Lamour radius

$$r_L = \frac{p_F}{eB} \quad (3.7)$$

where p_F is the Fermi momentum. It is much larger than the mean free path l . Using this, it can be shown that, for a current perpendicular to the field, the change in resistivity $\Delta\rho(B)$ relative to the zero field resistivity $\rho(0)$ is

$$\frac{\Delta\rho(B)}{\rho(0)} \propto \left(\frac{l}{r_L}\right)^2 \propto B^2 \quad (3.8)$$

We want now to investigate the case for higher fields where $r_L \leq l$ holds. From equation 3.6, we see that the Lorentz force affects the momentum perpendicular to the field significantly and changes it within time

τ . This results in a varying electron velocity $v(p) = \delta\epsilon(p)/\delta p$. The velocity depends on the momentum and is always perpendicular to the Fermi surface. To calculate the conductivity, it is necessary to solve the Boltzmann kinetic equation for the case with both electric and magnetic fields. For the semi-classical τ -approximation the solution yields the conductivity tensor $\sigma_{\alpha\beta}$ in the form

$$\sigma_{\alpha\beta} = -\frac{2e^2\tau}{(2\pi\hbar)^3} \int \frac{df_0}{d\epsilon} v_\alpha(p) \overline{v_\beta(p)} dp \quad (3.9)$$

where α and β stand for the directions x,y and z, $df_0/d\epsilon$ is the energy derivative of the equilibrium Fermi distribution function and $\overline{v_\beta(p)}$ the velocity averaged over the scattering time τ :

$$\overline{v_\beta(p)} = \frac{1}{\tau} \int_{-\infty}^0 v_\beta(p, t) e^{t/\tau} dt. \quad (3.10)$$

One can now see that the conductivity depends on the the velocity and average velocity, which depend on the magnetic field.

Lifshitz and co-workers have shown that the asymptotic behavior of the conductivity in high magnetic fields is qualitatively determined by the the topology of the orbits of the electrons on the Fermi surface. This then allows us to gather important information about the Fermi surface geometry from the conductivity. The electron motion along a closed orbit in momentum space can be characterized by the cyclotron frequency

$$w_c = \frac{2\pi eB}{(dS/d\epsilon)_{p_B}} = \frac{eB}{m_c} \quad (3.11)$$

where S is the area of the orbit orthogonal to the magnetic field B and the cyclotron mass

$$m_c = \frac{(dS/d\epsilon)_{p_B}}{2\pi}. \quad (3.12)$$

For electrons on closed orbits in a strong magnetic field we get new states with quantized energy, which then form subbands. Landau found that the energy of the states can be derived from a free electron gas in a magnetic field by

$$\epsilon(n, p_B) = \left(n + \frac{1}{2}\right) \hbar w_c + \frac{p_B^2}{2m_e}, \quad (3.13)$$

where m_e is the mass of the free electron, n the integer number for level n and p_B the momentum parallel to the field B. The electron orbits then follow the intersection of the Fermi surface orthogonal to the field and the Landau subbands.

3.4.2 Shubnikov-de-Haas oscillations

The theory of the effect is rather complicated, as it requires the detailed problem of electron scattering in a magnetic field. However the effect can be qualitatively understood using a simple idea from Pippard. He showed that the probability of scattering is proportional to the number of states into which the electrons can be scattered. This probability then determines the electronic relaxation time τ and the resistivity will oscillate in sympathy with the density of states $D(\xi)$ around the Fermi level. This can be shown to be proportional to the field (B) derivative of magnetization M :

$$D(\xi) \propto \left(\frac{m_c B}{S_{extr}}\right)^2 \frac{\delta M}{\delta B} \quad (3.14)$$

where S_{extr} is the extremal Fermi surface, e.g. the surface with the biggest or smallest area perpendicular to the field. The oscillatory part of the conductivity σ can then be expressed in the form

$$\frac{\sigma}{\sigma_0} \propto \sum_{r=1}^{\infty} \frac{1}{r^{1/2}} a_r \cos \left[2\pi \left(\frac{F}{B} - \frac{1}{2} \right) \pm \frac{\pi}{4} \right] \quad (3.15)$$

where σ_0 is the background conductivity,

$$a_r \propto \frac{m_c B^{1/2}}{S_{extr}^{1/2}} R_T(r) R_D(r) R_S(r) \quad (3.16)$$

holds, m_c is the effective carrier cyclotron mass and $R_T(r)$, $R_D(r)$ and $R_S(r)$ are damping factors. We will introduce them in the following.

The damping factor R_T originates from the smearing of the Landau bands due to the Fermi distribution, which leads to bands with higher energy being partially occupied by electrons from lower lying bands. This however reduces the change in the electron density of states at the Fermi level when increasing or decreasing the magnetic field. The exact expression for R_T is

$$R_T(r) = \frac{2\pi^2 r k_b T / (\hbar \omega_c)}{\sinh[2\pi^2 r k_b T / (\hbar \omega_c)]} = \frac{K r \mu T / B}{\sinh[K r \mu T / B]} \quad (3.17)$$

with

$$\mu = \frac{m_c}{m_e} \quad (3.18)$$

the cyclotron mass normalized to the electron mass m_e and all constants from the first formulation gathered together into

$$K = \frac{2\pi^2 k_B m_e}{\hbar e}. \quad (3.19)$$

This temperature dependence of the amplitude allows us to get the cyclotron mass m_c by measuring the oscillations at different temperatures and then fitting the amplitudes.

Second we want to have a look at the damping due to impurities in the crystal. These impurities also wash out the Landau sub-bands, as a finite lifetime leads to an uncertainty in the energy of the electrons, due to Heisenberg's uncertainty relation for time and energy.

Usually one takes a Lorenz or a Gaussian distribution to describe the scattering. The factor in the amplitude of the oscillations that describes this is the so-called Dingle damping factor

$$R_D(r) = \exp\left(-\frac{\pi r}{\omega_c \tau}\right) = \exp\left(-\frac{K r \mu T_D}{B}\right) \quad (3.20)$$

with the Dingle temperature

$$T_D = \frac{\hbar}{2\pi k_B \tau} \quad (3.21)$$

which is due to its dependence on the life time, a measure for the disorder.

The third factor is due to the effect of Zeeman splitting and has if no magnetic impurities are present the form

$$R_S(r) = \cos\left(\frac{\pi}{2} r g \mu\right) \quad (3.22)$$

with g the Landé factor. In case of magnetic impurities a beating, e.g. a periodic change in the amplitude is visible. However, for the present work, this was not observed in the Shubnikov-de-Haas oscillations measured and we would only get a change in the amplitude. Therefore this is not discussed in further detail here and we leave the details to Kartsovnik [27].

3.5 Theory for U/t change from effective mass

A change of U/t predicted from Guterding et al. [14] upon getting ethylene endgroups from the eclipsed ground state into the staggered excited state. Oberbauer et al. [5] showed that in κ -Cl and κ -(BEDT-TTF)₂Cu[NCS]₂, the effective cyclotron mass changes with pressure p in the following

$$m_c \propto \frac{1}{p - p_0} \quad (3.23)$$

with $p_0 = -410 \pm \text{MPa}$. Both the Brinkman-Rice theory [30] and the (single-site) dynamical mean-field theory (DMFT) by Georges et al. [31] calculated a change of the effective mass, which follows the formula:

$$\frac{m_{c,band}}{m_C} = C_Z \left[1 - \frac{U/t}{(U/t)_0} \right] \quad (3.24)$$

with the prefactor $C_Z = 2$ from the Brinkman-Rice theory and $C_Z \approx 0.9$ from the DMFT calculations by Georges et al. Oberbauer et al. [5] give $(U/t)_0 = 12$.

4 Experimental methods

In this chapter the measurement methods are presented. These methods were used to measure the temperature-, time- and magnetic-field-dependent resistance of the samples.

A LabView measurement program, written by Sebastian Jacob [32] and Michael Kunz [33] during their master-thesis, was used to gather the measurement data from the measurement devices and to store the data for further analysis. This program was used for all experiments done in Garching. For the experiments done at the HMFL in Dresden the local setup was used. In Garching the effects of annealing and quenching at ambient pressure and under pressures up to 450 kbar, the T_c dependence on the ordering and disordering were investigated and the heat pulse setup and procedure were developed. At the HMFL in Dresden the Shubnikov de Haas oscillations were measured.

4.1 Measuring resistance of the samples

To measure the resistance the samples were contacted in a four contact probe setup using graphite paste as conductive adhesive and annealed 20 μm Platin wires. The contact resistance was typically on the order of 40 Ω to 110 Ω for κ -Br and 30 Ω to 50 Ω for κ -Cl. The platinum wires were soldered onto a platform to connect them to twisted pairs of 100 μm thick copper wires. These copper wires were then connected to the measurement devices. The four contact probe was used to measure the sample resistance without the resistances of the contacts and wires. This is done by gluing two pairs of wires to the sample on the opposite sides of the crystal planes, such that by sending a current through one pair, a current flows through the crystal in the desired direction in which to measure the resistance. By measuring the voltage drop over the sample in the desired direction with the other pair, the sample resistance can be calculated. For all measurements in this thesis, the resistance measured was orthogonal to the conductive planes of the sample. The contact resistance of the samples was typically from 50 Ω to 110 Ω .

For low resistances up to 50 k Ω either Stanford Research Systems SR830, Princeton Applied Research 5210 or Zurich Instruments MFLI lock-in amplifiers were used to measure the resistances. All lock-in amplifiers used have only a constant voltage amplitude. To keep the measurement current constant a load resistance as described in fig. 4.1 was used. The measurement current with the used load resistances and the set output voltages were 1 mA to 10 mA. The sample resistances ranged up to 3 k Ω over all temperatures for κ -Br. For κ -Cl the highest resistance found was 70 M Ω which was measured at the lowest temperature in the isolating state. For the lock-in frequency, values 97 Hz, 143 Hz, 162.55 Hz, 227 Hz, 231 Hz, 253 Hz, 277 Hz, 333 Hz, 408 Hz, 524 Hz, 647 Hz, 736 Hz, 1 kHz. For measuring in magnetic field also a frequency of 13 Hz and 17 Hz. For measuring For high resistances above 50 k Ω , Keithley 2400 Sourcemeters were used as current source with measurement currents of 10 nA to 100 nA and Keithley 2000 Multimeters to measure the voltage drop in the four point measurement in DC resistance measurement. For measuring with the Keithleys the in- and outputs were directly connected to the sample without the load resistance. As any temperature gradient causes a thermo-electric voltage, the voltage was measured with one polarity and then with the opposite polarity and averaged over both values, switching the polarity via software.

4.1.1 Naming samples

To simply identifying samples, each sample was given a name. This allowed to track and talk about different samples over the different measurements. If one only gives each sample a number in each measurement

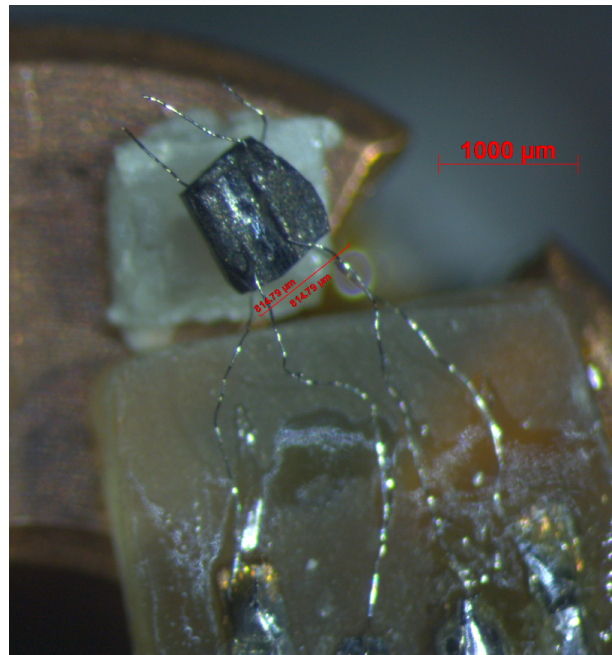
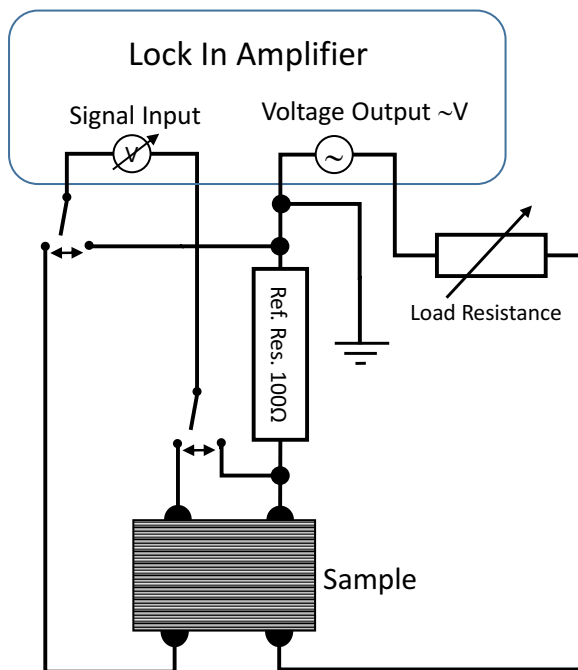


Figure 4.1 Left: Sketch of the measuring circuit of the lock-in amplifier and the wiring of the measurement setup in four point probe configuration. An ac voltage output is connected to the sample via a tunable resistor. The resistor can have values $100\ \Omega$, $1000\ \Omega$, $10\ \text{k}\Omega$, $100\ \text{k}\Omega$ or $1\ \text{M}\Omega$, which allows to choose a value that keeps the current amplitude through the sample approximately constant. Further, this allows to set the current according to the sample resistance. The two switches in the sketch are mechanically connected and switched as one, forming a mechanical switch. The switch allows to measure the reference resistor to calibrate the system and to set the voltage output such that a defined measurement current flows. In all cases except the heat pulses described later the output was set slightly above 1 V such that a simple multiplication factor can be used to convert from measured voltage drop to the resistance. Once the voltage output is set the switch is set to measure the sample. **Right:** sample Hepheistos contacted in a four-wire probe setup. Visible on the bottom of the picture is the platform that is used to change from platinum to copper wires. A thin piece of plastic was glued under the sample to prevent the sample from making a conductive contact with the copper block that serves as sample holder.

in can become difficult to remember which sample had which number were. The names given to each sample as well as an explanation of the name is given in appendix A.1.

4.1.2 Integrating new lock-in amplifier

Two new Zürich Instruments MFLI lock-in amplifiers (short MFLI lock-ins) were bought for which a new subprogram for the measurement program was necessary. The MFLI lock-in amplifier communicates via LAN and needs a constant connection to be upheld. This is in contrast to the devices used previously, that communicate via GPIB. These devices do not need a permanent connection. This means that instead of sending queries to the devices when the next measurement value is to be read, it is necessary that a subprogramm is running in a separate thread for each MFLI lock-in. This subprogram upholds the connection, reads data from the MFLI lock-ins, and closes the connection once the program stops. Not closing the connection as well as opening too many connections in parallel can lead to the device becoming irresponsive to new connection attempts, once the maximum number of connections is reached. To solve this a reboot of the device is required.

4.1.3 Problems with auto range on Keithley 2000 multimeters in case of huge changes of resistance with time and temperature and certain resistances

Using auto range has the advantage that neither the input is too high for the set range and potentially damages the measurement device, nor the input is much lower than the range which leads to avoidable noise on the measured input. However it was found that under some conditions the Keithley 2000 multimeters have difficulties with autorange, as shown in the following graph. The sample measured was a fully hydrogenated κ -Cl sample, named Little Big sample. The measurement was done at a pressure of 180 bar where the sample is in the Mott insulating state. It shows a strong increase of resistance from 10 k Ω at 30 K to 31 M Ω at 13 K. Below 16 K, while measuring in autorange, the resistance starts to jump.

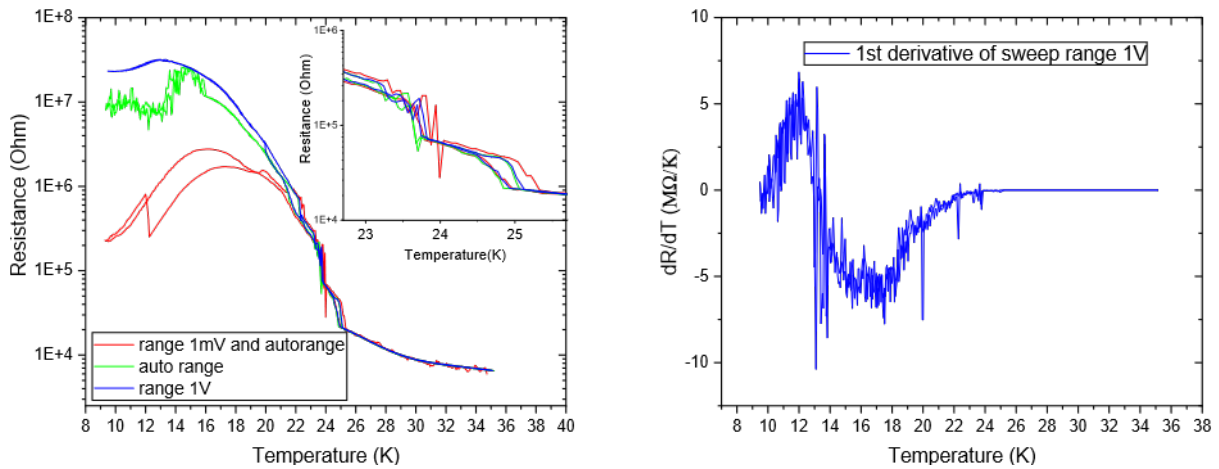


Figure 4.2 Left: All three measurements were done by cooling from 35 K to 9 K and then warming again to 35 K. First measurement was with a measurement range of 1 mV, a measurement current of 10 nA, a sweep speed of 2 K/min and a switch to auto range on warming at 20 K. The resistance is much lower than on the other measurements as likely the multimeter was in over range. On warming at about 23.5 K, a jumping behaviour can be seen on the first measurement which does not occur on the other two measurements. The difference between the first and the second measurement is that the second measurement was done with a temperature sweep rate of 1 K/min. This implies that not only $\frac{dR}{dT}$ needs to be considered but also the temperature rate. The second sweep was done with auto range on and the third with 1V range, both with a sweep rate of 1 K/min. **Right:** numerical derivative of the sample resistance with respect to the temperature of third sweep.

At first a loose contact was suspected to be the source of the jumps seen in the measurement. The samples were mounted in a pressure cell, which is explained later in section 4.8. Warming up, opening and closing the pressure cell as well as checking all wires takes a considerable amount of time, therefore the measurements were continued. Only at the end of the measurements the first measurement in fig. 4.2 was done by accidentally not switching to auto range. It was only after the second measurement, which then used auto range, that it was understood, that what was assumed to be the effect of bad wiring, was in fact the effect of using auto range. To verify this the third measurement was performed. This measurement does not show any of the problematic jumping behaviour.

The jumps are visible where the derivative $\frac{dR(T)}{dT} \cdot \frac{dT}{dt}$ is high, as visible at the phase transition at 23.5 K. On the other hand the derivative $\frac{dR(T)}{dT} \cdot \frac{dT}{dt}$ is also big below 18 K as seen in the right picture of 4.2, but the jumps only occur below 16 K. This implies that the resistance also plays a role.

The exact cause of the jumps and when they occur, is not fully understood from this measurement, but if the jumping behaviour is visible then the solution is to set the range to an adequate constant value.

4.2 Sample preparation

Pictures of the samples, including dimensions and basic physical properties including from which batch they are, can be found in the appendix in the tables A.1 till A.5. The samples used in this thesis were provided external and their crystal grower can be read from the batch. It is

- NKG – Dr. Natalia Kushch from the Institute of Problems of Chemical Physics (Chernogolovka, R.F.) during her visits at the WMI
- EK – Dr. Harald Müller, European Synchrotron Radiation Facility
- AFCI – Dr. H. Schubert (group of Prof. M. Lang), Goethe Uni. Frankfurt
- PC – Peter Christ, WMI – he was a PhD student of W. Biberacher and was most likely assisted in the crystal growth by W. Biberacher and by Dr. A. Lerf both WMI

The single crystals of κ -Br and κ -Cl were prepared electrochemically, from a solution of the organic molecule BEDT-TTF and the respective anion, with alternating current, using platinum electrodes.

4.3 Thermometry and stabilising temperature

4.3.1 Thermometry

The temperature of the samples was measured with Cernox thermometers. For the experiments in Garching a LakeShore model CX-1030-SD serial number X75113 cernox thermometer (short X75113) was used. In Dresden a LakeShore model CX-1030-SD-HT serial number X94057 cernox thermometer (short X94057) was used. Read-out of the thermometers was done with LakeShore 340 and LakeShore 350 temperature controllers. The thermometers used on the variable pressure set up described in section 4.8, are described in the PhD thesis of Dieter Andres [34]. The thermometers other than the sample space thermometer were only monitored as the delicate freezing procedure of Helium described in [34] was not used, as all experiments were done in liquid Helium at temperature and pressure above the freezing point.

4.3.2 Comparing thermometers and measuring T_c of Niob

The T_c of the κ -Br samples found in our measurements were higher than found in the literature. To verify this the two LakeShore thermometers, X75113 and X94057, were mounted onto the copper block sample holder. They were fixed with Apiezon N to have a good thermal coupling of copper block and thermometers.

First the two thermometers were cooled. This was done as the X94057 thermometer had been calibrated before with a thermometer with known good calibration and it was then to be used to check the calibration of the X75113 thermometer. A new calibration was created for low temperatures for the X75113 thermometer from comparing to the X94057 thermometer. The samples superconducting transition entrance is at 12.46 K, the midpoint of 50% resistance at 12.32 K and the 5% resistance is at 11.94 K. Comparing it to [10], who reports a maximum T_c of 11.7 K, we see that the sample is much colder than the thermometer. This is somewhat to be expected from the samples, see figure 4.4, being surrounded by Helium gas which can flow through the bottom hole and the side opening of the protective cup. The thermometers are strongly thermally coupled to the copper block which extends above the samples to thermal layers with a higher temperature above the samples. To reduce the temperature mismatch between sample and thermometer a big brass block was added around the protective cup and every opening was covered with either Teflon tape or duck tape as seen on the right of figure 4.4. Then to check thermometry further a Niob wire was cooled to check its T_c and compare it to the literature.

The first cooled Niobium wire showed a T_c of 8.87 K by the 50% resistance rule, with the setup up shown in figure 4.3. This is below the literature value of 9.2 K according to [23]. As the wire is expected

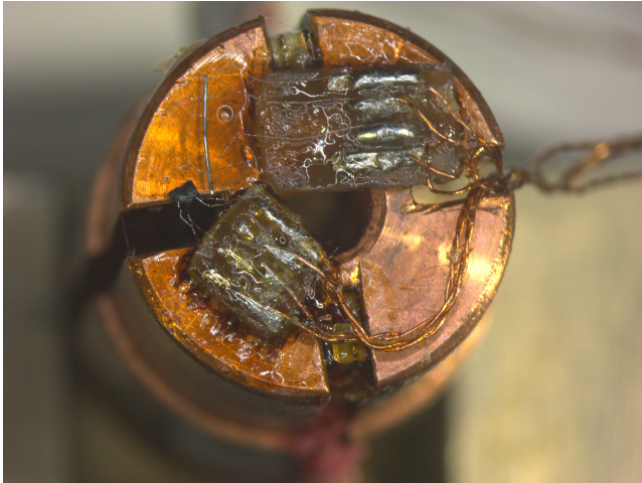


Figure 4.3 Left: The two thermometers on the copper block, visible in the lower and the upper slit, together with a niobium wire and the sample Crumb. The Niobium wire showed a T_c of 8.9K which is lower than the literature value of 9.2K according to [23]. From this it was concluded from that the wire is not made from pure Niobium. **Right:** Niobium foil together with sample Crumb and thermometer X75113. Note that what is seen here from the top view is hanging upside down in the helium cryostat.

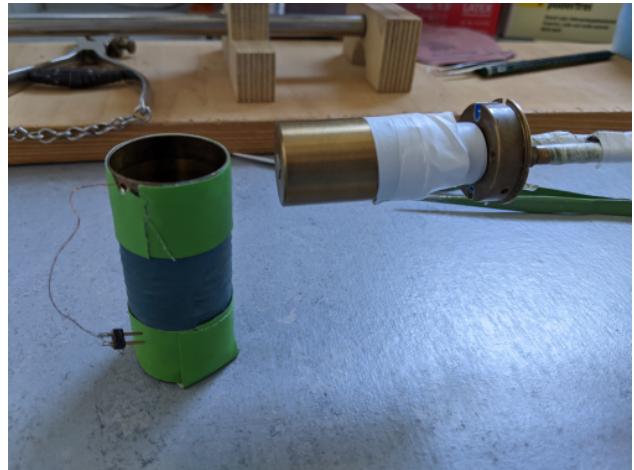


Figure 4.4 Left: The original setup. There is a big opening to the samples in the protective copper block covering the samples. **Right:** Brass block covering the setup and all holes sealed with Teflon tape

to be colder than the thermometer, it should show the superconducting transition at a higher thermometer temperature reading than 9.2K. It was suspected that the wire was not pure Niobium. For the second attempt the configuration was changed to the right of figure 4.3 with a piece cut from a Niobium foil. The foil showed a superconducting transition at 9.3K and the $K-Br$ sample a T_c of 12.27K both by the 50% resistance rule. From this we can conclude that the T_c needs to be lowered by at least 0.1 K.

4.3.3 Stabilizing temperature

For measuring the temperature Lakeshore 340 and 350 temperature controllers were used. Both can stabilize and control the temperature via their heater output, however the heater output on our Lakeshore 340 was broken. Therefore two methods of stabilization were used. One using the Lakeshore 350 and one written by Kunz [33] using a Keithley 2400 source meter. The program by Kunz did stabilize the temperature okay and had an acceptable convergence speed, but it was written for stabilizing temperature in a dilution refrigerator. This was noticeable as it was sometimes slower to stabilize and the stabilization oscillated with an amplitude of about 0.1 K. In contrast the amplitude of the PID (proportional, integral,

differential) stabilization of the Lakeshore 350 produced temperature oscillations with an amplitude of less than 0.01 K.

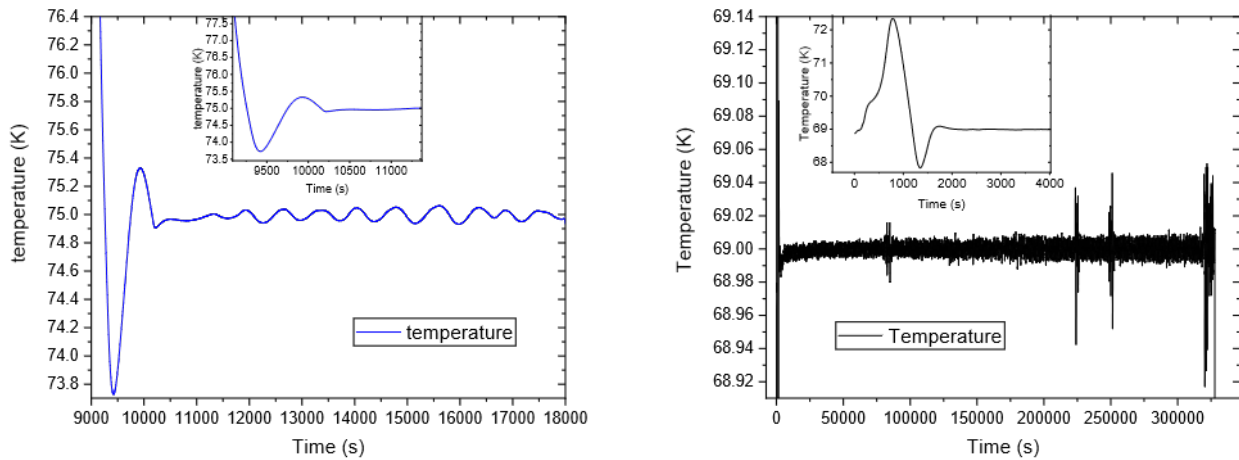


Figure 4.5 Stabilization around 70K to measure annealing of the endgroups of the samples. **Left:** Stabilization using the program of Kunz [33]. Noticeable are the significant temperature oscillations **Right:** Stabilizing the temperature with the PID stabilization of the Lakeshore 350. This was done over the weekend. Noticeable are the oscillations at some times and especially at 320000 s, which was at about 8 in the morning on Monday. This events mark a change in the pressure of the recovery line which leads to a small change of the temperature in the cryostat. It is interesting that it is possible to detect that other people at the institute work at what times with the temperature stabilization.

The lower amplitude of the temperature oscillations of the Lakeshore temperature controller meant it was used for stabilizing temperature whenever it was available. This is as when measuring the annealing rates of the glass transition, the approximately exponential dependence of the rate on the temperature means that strong oscillations will have a strong influence on the speed of the annealing and will change the measurement results.

4.4 Quenching methods

Three quenching methods were studied in this thesis.

4.4.1 Cooling the sample by turning off the heater

The most simple technique is by heating up the samples to a temperature above the glass transition by the heater installed in the sample chamber. This heater is mounted already to control temperature in sample space. This method can only cool down the samples maximally with the power the heater can maximally supply, as the highest reachable temperature difference to the cooling walls of the VTI is determined by the heater power. As the heater is only surrounding the samples in a distance it heats also the sample holder and its surroundings. When the heater is turned off not only the samples are cooled by the colder walls of the VTI but also the sample holder and the thermometer. This absorbs a lot of the cooling power and limits the maximal achieved cooling speeds in our case to around 10 K/min.

4.4.2 Cooling by moving the sample holder

To achieve higher cooling rates than with turning off the heater, a method similar to a black smith hardening iron by shock cooling it, was tested. This was done by reducing the pressure in the sample space and getting some liquid helium through the capillary of the VTI into the sample space. The sample holder was raised to an upper position till it had the desired temperature. A heater, which is turned off just before moving the sample holder, can be used to achieve a higher sample temperature than by simply lifting the

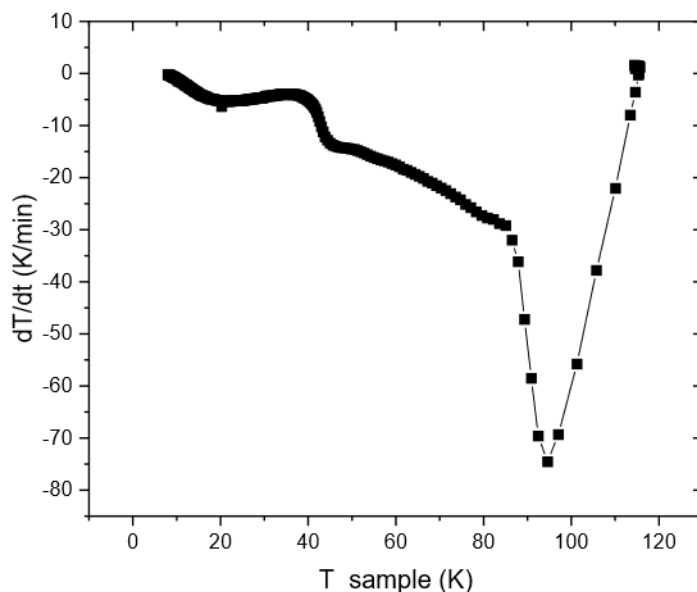


Figure 4.6 Cooling rate by moving the sample holder. The rate was calculated via software by calculating the numerical derivative of the thermometer. The process of calculating the derivative involves some averaging and as the thermometer is coupled to the copper block, the cooling rate of the samples are bigger but should be lower than the rates achieved by heat pulsing. This can be inferred as when disordered via heat pulses the sample shows a hysteresis above T_c and a stronger increased resistance. None the less the resistance at 14K changed from $3\ \Omega$ to $6\ \Omega$ implying some disorder relative to a cooling with $2\ \text{K/min}$

insert. The sample holder is then moved rapidly down into the liquid helium to quickly cool the samples. The achieved cooling rates are shown in picture 4.6. However quenching by moving the sample holder is not possible in system using Helium 3, due to leak concerns.

4.4.3 Using the sample as a resistive heater to heat itself

This method was used mostly in this thesis and is explained in the following section in detail.

4.5 Heat pulsing

To disorder the ethylene endgroups it was proposed by Hartman and Mueller [8], to heat the sample by a strong current or voltage pulse above the glass transition and then by switching off the voltage or current, to cool the sample rapidly due to the much colder environment. This very fast cooling through the glass transition then freezes the disorder of the endgroups at the end temperature of the pulse. This way a strong disorder of the endgroups was achieved. Hartman and Mueller used a partially deuterated κ -Br sample that was close to the MIT. This allowed them to tune their sample across the MIT by disordering the ethylene endgroups. We therefore wanted to use this technique on fully hydrogenated κ -Br to see how close we can get to the MIT.

We were able to partially reproduce their method, also using a Keithley 2400 source meter to apply the pulse, but instead of a SR830 lock-in we used a Par 5210 lock-in. We successfully disordered the ethylene end group, and archived a reversible increase in resistance, which we took as evidence that we added disorder to the sample but did not introduce micro cracks or any other permanent defects. However we did the pulsing in a semi manual way, which meant that the duration of the pulse, was done by switching on

and off the source meter by hand. During testing and implementing the heat pulsing method, by a operator accident, the sample Vesuv was burned. It was therefore decided that a fully automatic heat pulse control needed to be programmed, that checks if all heat pulse parameters are within the safety limits and allows for a defined pulse duration. During the design of this program it was noticed, that the Zürich Instruments MFLI lock-in amplifiers are able to apply a dc bias voltage up to 10 V together with the ac output of the lock-in. This then, together with the ability to measure and transfer up to 1674 measurement points per second, was used to create a measurement setup that allows for monitoring the heat pulse during the heating and cooling phase. This made it is possible to measure voltage and current during warming and cooling phases of the heat pulse directly.

This has the advantage that the time dependent resistance can be calculated directly from current and voltage drop over the sample. The resistance $R(\text{time})$, together with $R(T)$ curves of the sample before and after the pulse can be used to calculate $T(t)$ and $\dot{T}(t)$. This idea to use the sample as a thermometer was also used in [8]. There however they needed to fit the cooling rate and final temperature of the heat pulse from a heat bath model:

$$P(t) = C \cdot \dot{T}(t) + \lambda[T(t) - T_{bath}], \quad (4.1)$$

. Here C is the sample's specific heat, λ is the parameter for the coupling to the cooling bath $P(t)$ the heating power and T_{bath} the temperature of the surrounding of the sample.

4.5.1 Description of the heat pulse setup

The programs for controlling the heat pulse and reading the data was created in LabView. The general idea is to have three threads running in parallel. A thread for each ZI MFLI to read the data from the devices and a thread to precisely control the pulse. This was realised in two programs. The measurement program that reads the data and the heat pulse program that controls the heat pulse. This allows independent use of the heat pulse program from the MFLI lock-ins, by also implements heat pulsing with a Keithley 2400.

As the first heat pulse trials were done with the Keithley 2400 alone, the separation into two programs had historically grown, but the separation was preserved as it allows for higher flexibility in using the programs. Further seperating into two programmms has the advantage that it makes sure that heat pulse and measurement program run and work independently. This is import, as it make sure that the the dc bias voltage output of the MFLI lock-ins is turned off in time.

The two programs as the detailed procedure when applying a heat pulse are described in detail in the appendix A.3. A brief summery is given here. The measurement program reads the data from the MFLI lock-ins and handles the measurement of the pulse. When the measurement is started and running without problems it requests a heat pulse from the heat pulse program. The heat pulse program checks if all conditions for the heat pulse are met and applies the heat pulse if everything is alright. For the MFLI lock-ins this means it applies a dc bias to the signal output. As starting temperature 35 K was chosen as it does not put too much thermal stress on the sample, but was enough to achieve high enough cooling rates. Also when applying the voltage pulse the heating power applied to the sample is V^2/R . Looking at $R(T)$ as for example in fig. 5.1 in section 5.1, the resistance falls almost exponentially with decreasing temperature. To avoid this super strong heating power the pulse is not done from 6 K as does Hartman et al. [8] but from a higher temperature. For the first attempts 35 K was tried and then used for the other pulses for comparability. Decreasing the bath temperature to 5 K would increase cooling rate by approximately 30 % when going to 130 K as can be estimated from a simple heat bath model in equation 4.1. As will be later shown in subsection 5.3.3, 120 to 130 K is the temperature where the relaxation rates of the ethylene endgroups is so fast that heating above this temperature does not in crease the disorder. This is as with the achieved cooling rates the disorder already relaxes during cooling. Increasing the cooling rate would increase this temperature but as shown later in subsection 5.2.2 the relaxation rate increases by a factor of 10 about every 5.5 K. Therefore by increasing the cooling rate by 30 % would only increase this maximal temperature by a few Kelvin and looking at fig. 2.2, the increase of the occupation of the excited state would be small.

Heat pulse schematics

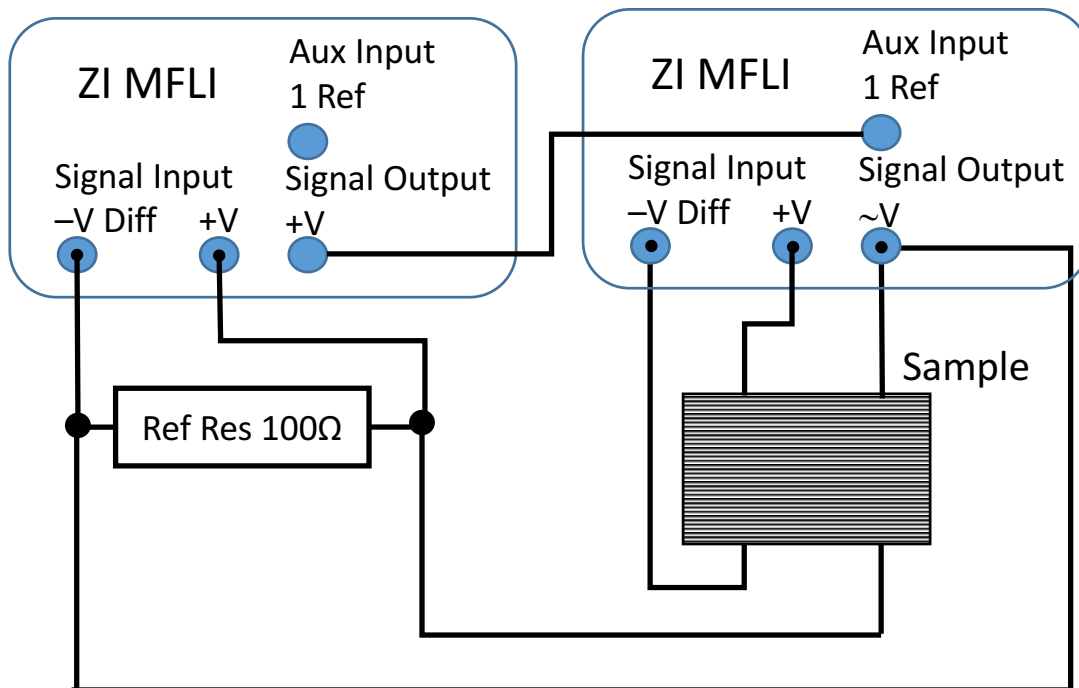


Figure 4.7 Wiring plan of the heat pulse setup. The MFLI lock-in on the left is responsible for measuring the current through the sample by measuring the voltage drop over a $100\ \Omega$ reference resistance, which is in series with the sample. This MFLI lock-in is therefore called current MFLI. The ZI MFLI on the right is responsible for applying the voltage, both ac and dc, over the sample and reference resistance, as well as measuring the voltage drop over the sample. This MFLI lock-in is therefore called voltage MFLI. Both MFLI lock-ins are synchronized by using the current MFLI as external reference for the voltage MFLI

This approach in general is part of the strategy to heat the sample only as much as necessary to archive good disordering but also to keep the thermal stress low. It was therefore also avoided to keep the sample at a temperature far above the surroundings longer than necessary. Therefore a step up where the temperature is increased in steps as does Hartman et al.[8] was not used. This method has the advantage that it works with lower thermal stress on the sample, which is important especially for samples and compounds with lower mechanical stability than κ -Br and κ -Cl.

It was shown by [8] that a partially deuterated κ -Br sample can survive being heated to 307K with the surrounding bath at 6K and then rapidly cooled by turning of the heating voltage through the sample. This should also hold for the fully hydrogenated κ -Br. However, as it is very difficult and time consuming to change a sample in a Helium 3 cooling setup and good samples are best treated with care. Therefore in our case less stressful parameters were chosen. Further keeping a sample at a higher than surrounding temperature warms the surroundings of the sample effectively reducing the achieved cooling rates, especially in the important temperature range several dozen Kelvin above the glass transition. This thermal region is important as we later show in the experimental results region, as it is the one where the annealing rates are on the order of milliseconds and seconds. This means there the ordering rate is not much faster than the cooling rate.

The current and voltages measured are processed after the pulse by the measurement program to calculate the sample resistance $R(t)$. This is can be combined with $R(T)$ before and after the pulse to get $T(t)$, $\dot{T}(t)$ and $\ddot{T}(T)$. The results of one example heat pulse are discussed in section 5.3.

We want to compare here the approach via heat pulsing with a Keithley 2400 and a SR DSP 830 lock-in amplifier as [8] do, to the approach in this thesis. The approach here has the following advantages and disadvantages: Advantages

- The resistance during and after the pulse can be precisely monitored with a high number of measurement points, with our settings with 209 measurement points per second.
- This allows for a fast approach to the final temperature and to measure the final temperature of the samples precisely. Quickly approaching the final temperature heats the environment of the samples the least and therefore allows for a higher cooling rate.
- The drop of resistance after the pulse can be precisely monitored although not the very first part due to the switching of the dc bias. This allows to calculate the gradient of temperature over time directly and not via the fitting approach of [8].

Disadvantages

- The final temperature can only be estimated before the pulse in the current version of the program as it only sets the voltage once. This however can be changed such that resistance is permanently calculated and the program increases the voltage until the desired sample resistance and therefore the desired sample temperature is reached. This would be done via a first trigger that finds that the peak of the sample resistance is already crossed and a second one looking for the desired resistance.
- A SR DSP 830 lock-in amplifier and a Keithley 2400 are quite standard measurement devices that are likely already available in each lab. The newer MFLI lock-in amplifier used here, as of today cost in about 5000€ each and are likely not available in every lab.

4.6 He 3 gas system

To get to the low temperatures necessary for measuring Shubnikov de Haas oscillations in our samples, a ^3He gas system was used. The systems used in this thesis operated by first cooling the environment of the sample space as low as possible by pumping and evaporating ^4He . Then ^3He gas was inserted into the sample space and condensed. After condensing as much ^3He as possible, the sample space was pumped, which, by evaporation cooling of ^3He then cooled the samples. This was the same for the experiments performed in Garching and in Dresden. The lowest temperatures achieved were 380 mK in Garching and 630 mK in Dresden.

4.6.1 ^3He System in Garching

The ^3He system in Garching works by having 1.4 K stage around the sample space. This 1.4 K space is connected via a capillary to the main volume and allows for liquid ^4He to flow into the space. The capillary has a inner diameter of $50\ \mu\text{m}$ at room temperature and is wound to achieve a higher impedance by taking a longer capillary. Via pumping the 1.4 K space the temperature is lowered to 1.4 K by evaporation cooling. Via a good thermal connection the samples space is then too cooled to this temperature. By inserting ^3He gas into the sample space the samples come in thermal contact to the 1.4 K stage and parts of the ^3He gas condense. To get the lowest temperature in the 1.4 K space, a heater is installed in the 1.4 K space. The liquid ^4He in the 1.4 K space becomes super fluid inside the space and builds up and moves up the walls of the 1.4 K pot. This increases the evaporation area and increases cooling power. However due to a fixed throughput of the vacuum pump this also increases the pressure and therefore the temperature. To lower the evaporation surface and therefore to reduce the pressure, a heater is used to heat up the liquid inside the 1.4 K space. This then leads to complete evaporation of the liquid inside. After the evaporated liquid is pumped off the pressure in the sample space is reduced compared to the situation before turning on the

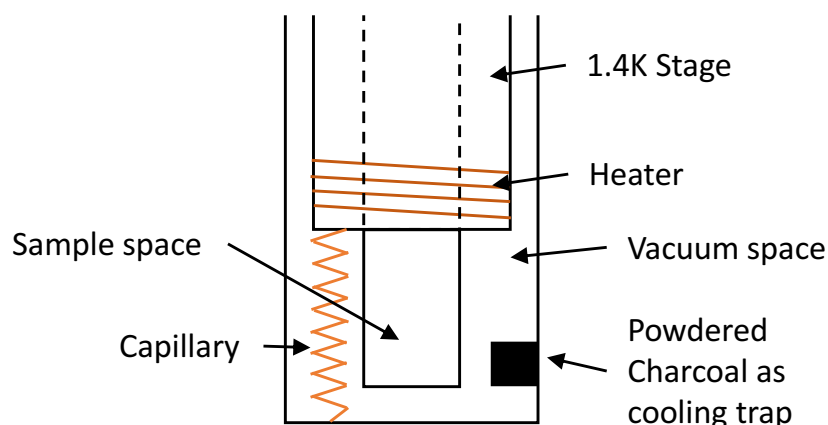


Figure 4.8 functional sketch of the ^3He variable temperature insert used for cooling to 380 mK in Garching, sample holder and samples omitted for simplicity

heater. Once the heater is turned off the liquid flowing through the capillary into the 1.4 K space evaporates in a lower pressure environment, which leads to a lower vapor pressure equilibrium and therefore to a lower temperature. Once the maximal amount of ^3He is condensed, the sample space is pumped, to lower the temperature in the sample space by evaporation cooling. The lowest achieved temperature was 380 mK. To isolate the sample space and 1.4 K space from the main volume both together are surrounded by the vacuum space. For the initial cool down the vacuum space is filled with a small amount of 0.5 mbar of ^4He . This leads to a thermal coupling of the main volume of the cryostat to the sample space and cools down the capillary. Once the capillary is getting cold it opens up due to the thermal contraction of the metal and a flow of ^4He from the main volume fills the 1.4 K space. Once everything is cold enough the 1.4 K space is pumped to cool the sample space. As the thermal coupling via the vacuum space is not needed anymore the vacuum space is pumped with a rotary pump and a turbo-molecular pump. This is done at a temperature slightly above 20 K, where the powdered charcoal that acts as a cooling trap does not cryopump that strongly. This allows to empty the charcoal which then when cooling down to base temperature cleans out the remaining gases in the vacuum space, improving the decoupling of the sample space from the main volume of the cryostat. As the ^3He setup in Garching was only used to characterise the samples, only the lowest temperature was of interest. To get to temperatures above the base temperature the valve between sample space and the pump was only opened partially. To stabilize temperature the valves were closed further when the temperature was falling and opened further when the temperature increased.

4.6.2 ^3He system in Dresden

The ^3He setup in Dresden works differently from Garching. The insert is much simpler. What the 1.4 K space in Garching does is replaced by pumping the main volume of the cryostat. The lowest temperature achieved by pumping the cryostat in Dresden was 1.4 K. The main volume of the cryostat is coupled with a variable coupling strength to the sample space. The coupling strength can be set by activating a heater (sorb heater) around the powdered charcoal. This powdered charcoal, acts like before, as a cryopump. Cooling down the samples and condensing liquid ^3He works by setting the heater strength to get the desired coupling of the sample space to the main volume. Once enough ^3He is condensed the temperature is lowered again by pumping the ^3He in the sample space. When approaching the desired temperature, the sorb heater is turned off. It was found by operator accident of the autor of this thesis, that lower temperatures can be achieved by keeping the sorb heater on during the cool down to base temperature. An explanation to this is that via the increased coupling of the main volume of the cryostat to the sample space, the heat load from above is cooled away. This is that the cooling power of the cryostat

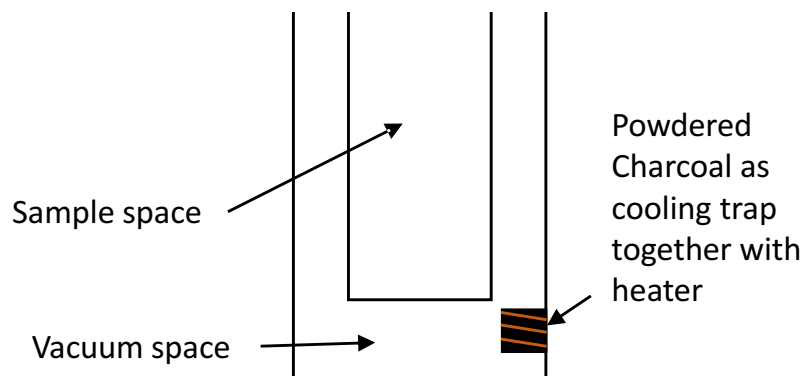


Figure 4.9 functional sketch of the ^3He variable temperature insert used for cooling to 630 mK in Dresden, sample holder and samples omitted for simplicity

main volume acts like a heat shield against the heat flow from the insert holding the samples and the thermal radiation from the top of the insert which is at room temperature. But this coupling has also the adverse effect that the lowest part of the sample space where the samples are located, is also coupled to the main volume of the cryostat. As this main volume is at 1.4 K while the sample space temperature is at 0.63 K the coupling of the sample space to the main volume also heats the samples. This is why just before reaching the lowest temperature the sorb heater is turned off. This allows to achieve a lower temperature in the sample space until the heat from the top of the insert reaches down to the samples.

Setting a temperature above the base temperature needed a different procedure than in Garching. The inner diameter of the ^3He insert was 15 mm. The diameter of the sample holder rod was 10 mm which left a gap of 2.5 mm on each side meaning small area for the gas flow. The system was so inert that opening or closing a valve partially needed on the order of minutes to make effect on the temperature and the change of the temperature in the samples space. Stabilizing to different temperatures then had to be done by opening the valves between sample space and pump gradually and then observe to which value the temperature in the sample space drifted. When the value was too high, one of the valves had to be opened gradually and one observes again to which value the temperature drifted. The time between two openings of the valves was in about 5 to 30 minutes. Operating the valves was further complicated by spontaneous drops of the temperature in the sample space. These drops only occurred once during the cooling procedure and may mark the moment once the level of liquid ^3He drops below the upper end of the sample holder seen in fig. 4.12. The increase in the evaporation surface might then increase the cooling power leading to a lower temperature. Further as the level now is closer to the samples with more space, a better convection coupling to the samples and the thermometer of the evaporation surface should be possible. Further when the level of liquid ^3He was too high above the samples the evaporation and therefore the cooling occurred far away from the samples. This meant that due to the low convection it was difficult to cool the samples, making a good predictable temperature stabilisation difficult.

4.6.3 Proposed improvement to ^3He system in Dresden

This findings lead to a proposed improved version of the insert. A continuous cooling of the part of the sample space above the samples acts as a heat shield against heat from the top of the insert. To archive this a 1.4 K space as in Garching could be added around the sample space. This should also reduce ^4He consumption as a smaller volume of ^4He is pumped and kept at low temperature. Further a refilling becomes much simpler as the main volume of the cryostat is at ambient pressure.

Low temperatures lead to decreased vapor pressures above the liquid and therefore to low densities of gas. Low densities of gas mean a low density of the gas flow when pumping the liquid to achieve low temperatures. A low gas flow implies low cooling power which leads to higher temperatures. To increase

the total flow of Helium 3 for low flow densities the sample space could be widened above the magnet, where the size restrictions due to the magnet bore diameter do not hold anymore. This should lead to a much lower base temperature.

Powdered Charcoal as cooling trap should be kept with a heater as there is already. This would allow to turn on the heater over night and have a small thermal coupling between sample space and main volume of the cryostat. Keeping the samples at low temperature this way should allow for a more Helium efficient cooling than pumping the 1.4 K space. Further this should be efficient enough such that one filling of the cryostat in Dresden is enough for over night.

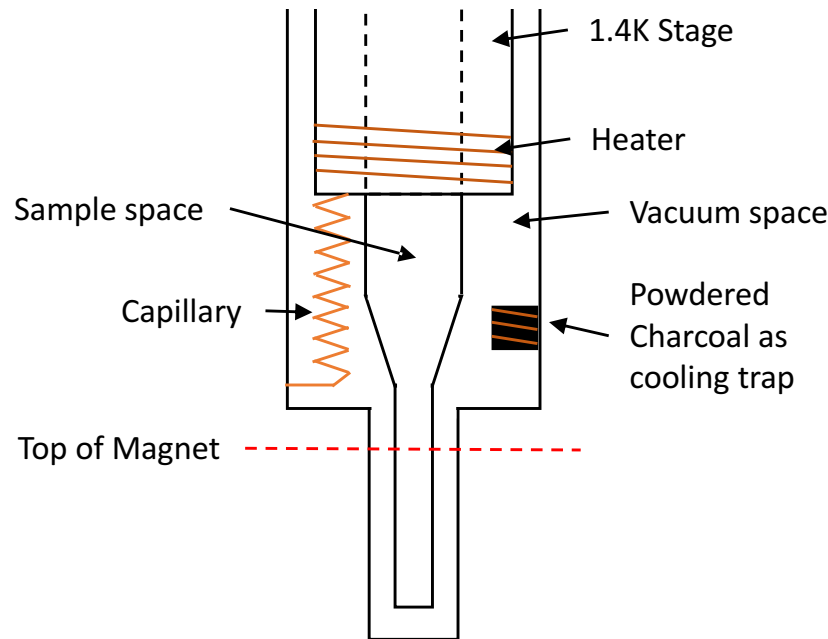


Figure 4.10 functional sketch of a proposed improvement to the ^3He variable temperature insert used for cooling in Dresden

4.7 Measuring SdH

We wanted to measure the effective mass depending on the thermal history of κ -Br. As explained in section 3.4, the amplitude of the oscillations is damped with increasing temperature but increased with increasing magnetic field. The factor determining this damping of the amplitude with temperature is the effective electron mass. The Shubnikov-de Haas oscillations in fields up to 15 Tesla were barely visible at lowest achievable temperatures in Garching. To get higher fields the pulsed magnetic fields at the Dresden High Magnetic Field Laboratory at the Helmholtz-Center Dresden-Rossendorf in Germany (HFLD) were used. To study the samples in different temperature ranges as necessary to determine the effective mass, a He3 system was used. Generally the samples were cooled to temperatures between 0.38K to 1.6K when searching for oscillations.

4.7.1 Characterising samples in Garching

The samples were pre-characterised by the ratio of peak resistance to the resistance just above the onset of superconductivity at 14K. A high ratio should imply that the samples show a good metallic behaviour of a strong decrease of resistance with temperature. This should imply that the number of defects is low as the defects dominate the resistance at low temperatures. The samples that showed promising ratios of $\frac{R(T_{peak})}{R(14K)}$ were then cooled by a He3 system to 380 mK and tested for oscillations using a superconducting

magnet in Garching. For $R(T_{peak})$ and $R(14K)$ values, see the appendix A.1. Good samples showed a ratio of 80 or bigger.

The superconducting magnet used for measuring oscillations is a system from Cryogenics consisting of two coils, with the inner coil made from Nb₃Sn and the outer coil made from NbTi, with the coils in serial. The coil was inside the cryostat and cooled with liquid Helium. The maximal achievable field was 15 Tesla when cooled to 4.2 K. When pumping the liquid He4 to 48 mbar pressure above the liquid, corresponding to 2.1 K, the field could be increased to 17 Tesla. Lowest achieved pressures in the main volume of the cryostat were 13 mbar corresponding to 1.74 K. The magnet was operated with a Oxford Instruments "Mercury iPS 120-10" magnet power supply capable of generating currents up to 120 A. The maximal current used to operate the magnet was 110 A.

The resistance of the samples was measured with Stanford Research DSP SR830 lock in amplifiers, with time constants of 1 s to 3 s and measurement currents of 10 to 40 μ A. Generally the measurements were performed with a time constant of 1 s, a sweep speed of $0.1 \frac{\text{Tesla}}{\text{min}}$ and a measurement current of 10 μ A. If no oscillations were found, improvements in sensitivity were made by increasing the time constant and reducing the sweep speed of the magnet to $0.05 \frac{\text{Tesla}}{\text{min}}$, increasing the measurement current to 40 μ A and/or using transformers. The transformers are applied to the wire pair that measured the voltage drop over the sample. The transformers should then act like a low pass filter that damps the shot noise from the graphite paste contacts on the sample. Four samples were identified that either showed oscillations visible by a Fourier transform or, as was the case for one sample, visible by eye above 16.5 T. These four samples were then taken to Dresden to be measured in high fields. The sample holder had enough measurement lines for three samples and a thermometer, with one sample used as back up sample.

4.7.2 Measuring effective electron masses at the high field laboratory in Dresden.

To measure Shubnikov-de-Haase oscillations a pulsed 70 T magnet at the HFLD was used. Precisely a KS3 Design 70 Tesla magnet with a 24 mm bore diameter. The magnet was cooled in a bucket filled with liquid nitrogen to 77 K. The samples were cooled with a bath cryostat from CryVac with a Helium capacity of 10 l. This meant that the cryostat had to be refilled after each pulse and after every night. To apply the magnet pulse several capacitance banks were charged to 21 kV to an energy content of 6.7 MJ. The entire stored energy was then released into the magnet to create the magnetic field of up to 70 T. This heated the magnet to room temperature and it took 3.5 hours for it to cool down, which is above its design cooling duration of 2.5 hours. The longer cooling time meant that 4 magnet pulses were possible per day.

The magnetic field generated is shown in figure 4.11. The measurement process of the resistance of the samples was done similar to the lock in setup as shown in figure 4.1. The difference is that in the Dresden setup the voltage drop over the reference resistor was measured during the magnet pulse to measure also the current through the sample. This works similar to the heat pulse wiring in figure 4.7. The AC voltage applied to the sample was generated by a "Low distortion Function Generator DS360 — 200 kHz" from Stanford Research. The voltage drops over the samples and reference resistors was measured by a "Yokogawa DL850 scope recorder". Applied frequencies of the voltage applied to the samples were 33333 Hz, 55555 Hz and 56455 Hz. It was found that the best results are obtained with each sample at a different frequency, to avoid cross-talk. The applied magnetic field was measured with a pick-up coil in the magnet. The signal of the pick-up coil was split by a BNC T-piece and was recorded with a second "Yokogawa DL850 scope recorder" and the scope recorder that records the voltage drops over the samples. The maximal measured magnetic field was 68.3 Tesla. The recorded signals were then processed with a digital lock in program provided by the HFLD, which did the lock in procedure of the recorded data, to generate the R(B) curves.

The samples were mounted to a holder made from PEEK. Using a plastic holder has the advantage that there are no induced Eddy currents in the holder from the fast changing magnetic field. The twisted wire pairs were fixed with Apiezon N such that they don't move in the magnetic field and any induced currents cancel each other due to the twisting and no currents are induced due to wire movement.

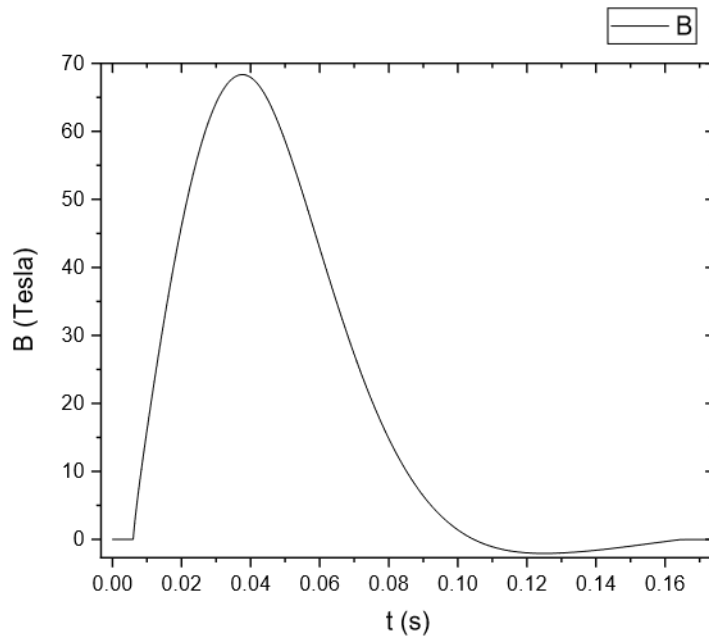


Figure 4.11 Magnetic field over time for the pulsed magnet used in Dresden.

Removing spikes in the measurement data

The Yokogwa scope recorders sometimes had problem with measuring the pick up coil signal and the voltage drops over sample and reference resistances. This can best be understood from the pick up coil signal as it was recorded twice. Sometimes one of the scope recorders did record the signal correctly while the other showed some nonphysical spikes, as happened for example in pulse 47, seen in figure 4.13. Sometimes it was possible to replace the measured pick up coil signal by one without spikes. In the other cases it was necessary to replace the spikes in the pick up coil signal, otherwise it was necessary to remove the spikes. Several improvements were made over the measurements in grounding the scope recorders such that for the late pulses, the signal of the pick up coil was clean. As an example of a late pulse with clean signal pulse 65 is shown.

Unfortunately these spikes did not only occur in the pick up coil, but simultaneously in the measured voltages of sample and reference resistances. It was therefore necessary to remove the spikes via software as removing them by hand would have taken too long. This was done via interpolation in the following steps as seen in figure 4.14. The goal is to replace the spike with data that fits in and does not cause problems when processing and analysing the data. The true data is not reconstructed here, but some replacement that should be close to the true data.

1. Choose the parts of the measured data where a spike is to be removed. Note that via setting the ranges correctly one can strongly influence the interpolation result. This is as the continuity condition of the spline implies that the interpolated data has the same derivative, at the edges of the interpolation as the data just outside the interpolated range. This can be used to get an interpolation with correct amplitude, curvature and derivative.
2. Interpolate the original measured data with a cubic spline except at the parts where a spike is to be replaced. The interpolation is not done on all measurement points but a fraction to reduce noise. Here only every fifth point was used for interpolation. A cubic spline was chosen as
 - It is a standard tool for interpolation when the interpolation points are already given [35, 106ff.].



Figure 4.12 The samples mounted to the sample holder as they were measured in Dresden. The Apiezon N was not applied yet on the photograph. It is noteworthy that two samples Nizza and NKG11 are below the thermometer. The thermal coupling to the thermometer is not very good as there are no materials in between that conduct heat well. Only sample Crumb is at the same height as the thermometer which means if the convection of the liquid Helium 3 is low and isothermal layers are formed in the liquid only the temperature of sample Crumb is known correctly.

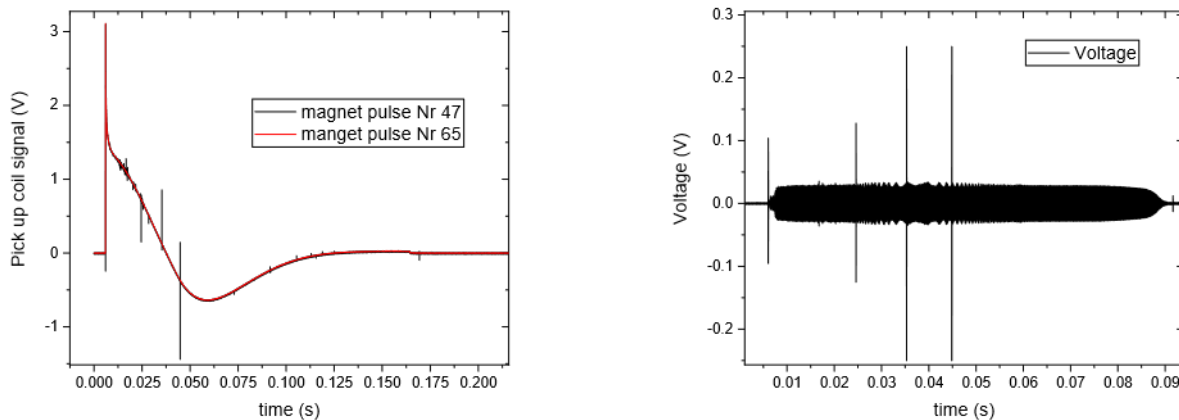


Figure 4.13 Left: Pick up coil signal of pulse number 47, which shows spikes in the signal. For comparison, the pick up coil signal of pulse number 65 with improved grounding, as recorded by the better scope recorder. **Right:** Spikes in the measured sample voltage over time of pulse 47. Note the fine oscillations of the signal generators at several dozen kHz are not resolved.

- Due to its smoothness at the interpolation points it is possible to get continuous first and second derivatives at the interpolation points. This allows to get the correct curvature that fits into the Shubnikov de Haas oscillations of the unchanged data. The Shubnikov de Haas oscillations can be approximated with a cubic polynomial for an interval of the size of the spikes encountered. The spikes encountered covered less than half an oscillation. By choosing the interval of interpolation in the right way the spline should be a curve is similar to what one would expect for the amplitude of the resistance. The error due to the interpolation should be on the same order as the other noise present or lower.

3. Evaluate the spline at the original magnet field values of the measured data where the spikes shall be removed, to get the interpolated resistance.
4. Store the measured data, with the interpolated values replacing the spikes. The data stored is shown as resistance corrected in fig. 4.13

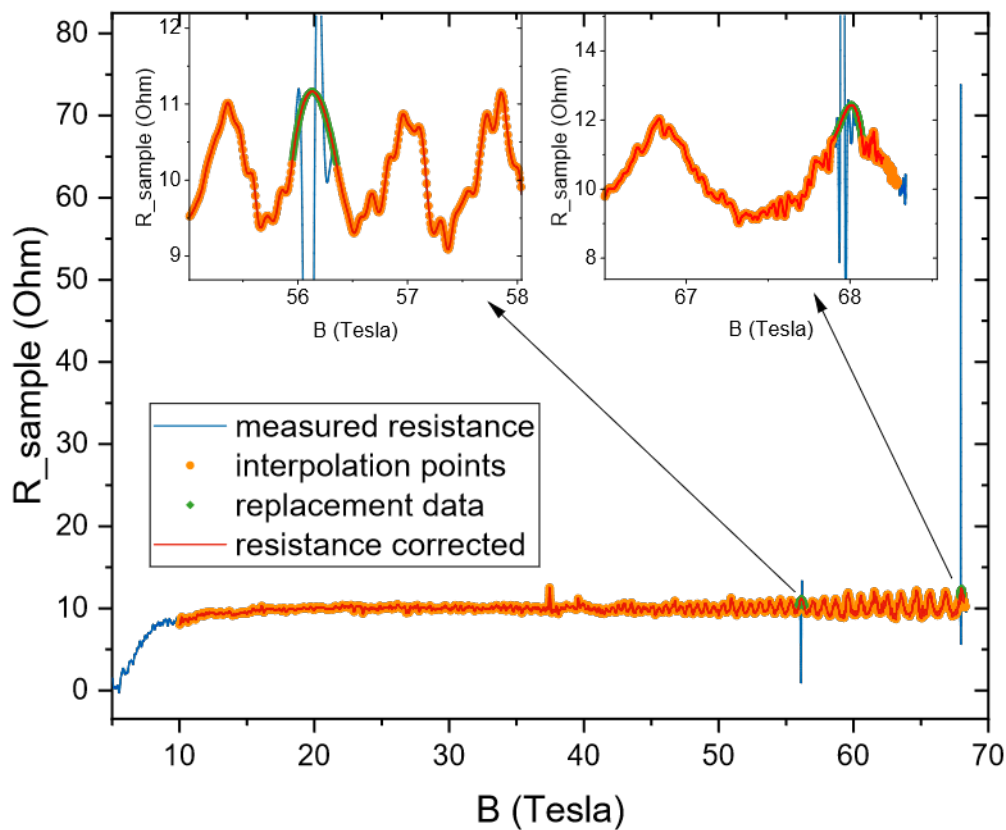


Figure 4.14 The steps of the interpolation process

4.8 Pressure Cell and He Gas Pressure System

In this thesis a He 4 gas pressure setup was used to study κ -Cl under pressure to compare the effect of pressure to the effect of annealing and disordering.

4.8.1 The ^4He gas pressure setup

The setup used, shown in figure 4.15, was bought and assembled, by Dieter Andres [34] during his doctor thesis and is described there in detail. Here shall be given a brief summary. The advantage of using a ^4He pressure system is that the pressure can be tuned while the sample is cold, in contrast to methods like clamp cells. This allows to do measurements at several different pressures cooling only once. As long as the pressure and temperature stay below the solidification lines of the p-T diagram, the pressure in the sample chamber can be precisely measured using the sketched pressure sensors. The lowest temperature was 9 K and the highest pressure was 450 bar at 35 K, which gives 420 bar at 9 K. This should be still be in the liquid range close to the solidification border, according to left side of figure 4.15 .

The setup is sketched in figure 4.15. First everything is pumped to clean out all gases except Helium and the setup is checked for any leaks. This is done as any gases except Helium would freeze out and potentially block or damage the finer parts of the setup. To operate the system and apply pressure, the He 4 gas is released from a storage gas bottle into a nitrogen trap. From the trap the gas is then pumped by a membrane compressor into the 3 kbar stage. The setup also contains a 10 kbar stage that via a cylinder

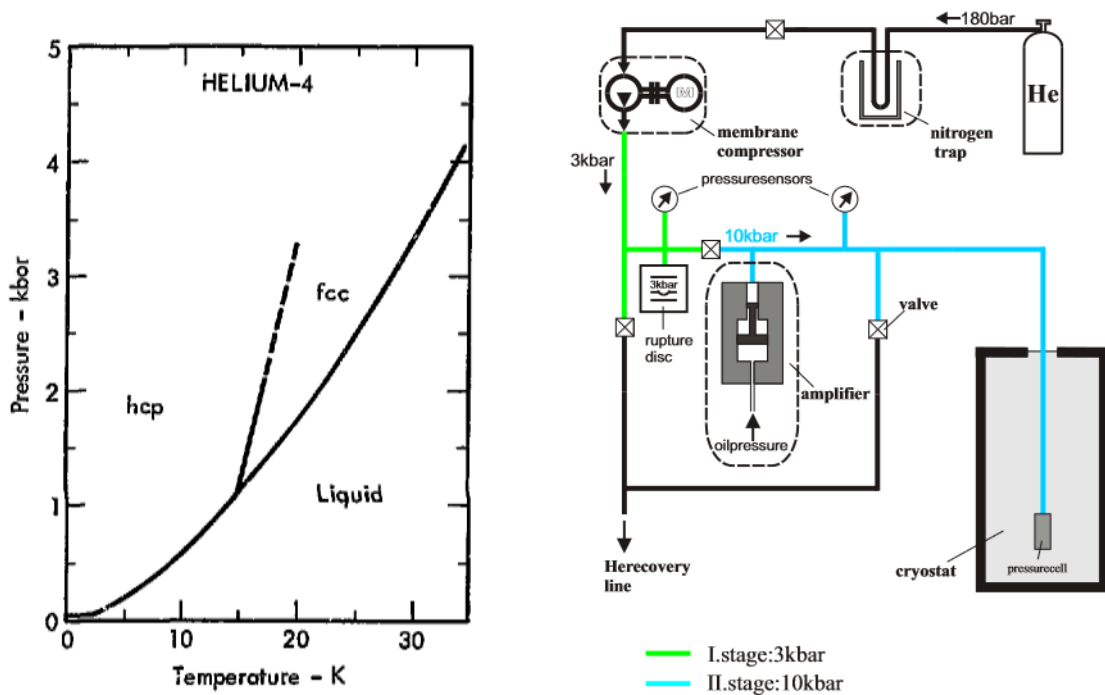


Figure 4.15 Left: Phase diagram of He in the range used in this thesis, from [36]. **Right:** drawing of He gas pressure setup by [34]

operated by oil pressure can achieve pressures up to 10 kbar. Due to a leakage this 10 kbar stage is not used. The output of the compressor is connected via a 4m long capillary made from a Cu-Be alloy to the pressure cell. A regulating valve and 4 one way valves after the compressor are used to set the pressure.

4.8.2 The pressure cell

The compressed ^4He gas is sent via the capillary into the sample chamber. The chamber is sealed with sealing rings made from brass covered in a thin layer of lead, which helps seal due to its softness. The samples are glued as usual to platinum wires on a feedthrough. This feedthrough contains copper wires which are used to measure the resistance in the usual four point probe setup. To seal the copper wires, the feedthrough is filled with "Stycast" epoxy, which embeds the copper wires and withstands the pressures applied.

Although changing the pressure while the samples being cold is a nice feature, this can not be used in a pure ^3He cooling setup, due to possible leaks of ^4He gas. It should however be possible to use this together with a dilution refrigerator, as it already uses a ^3He - ^4He gas mixture.

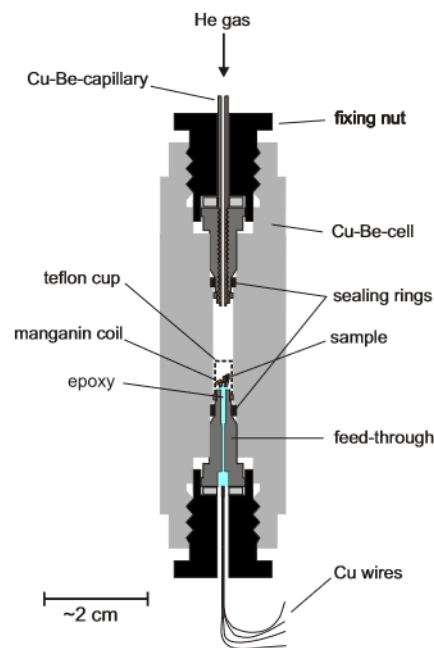


Figure 4.16 drawing of He gas pressure cell by [34]. Note there was no manganin coil mounted for our experiments. This pressure sensor is only necessary when the Helium solidifies. As our experiments were done on the liquid side of the solidification line in the p - T diagram, it was possible to use the pressure sensors included in the setup. The thermometer to measure the sample resistance was mounted on the outside of the cell on the same height as the samples. This was done as mounting the thermometer into the cell necessitates un-soldering all contacts, which would make a re-calibration necessary. Further the space in the sample chamber is very limited which makes it difficult to add the rather large thermometer. For sample and thermometer size comparison see 4.12

5 Experimental Results

5.1 Change in resistance over temperature depending on thermal treatment

At first we want to have a overview look at $R(T)$. Su et al. showed that the resistance below 80 K and the superconducting transition depends on the cooling rate of the sample. We want to study this effect also with respect to the changes in the phase diagram shown by Hartman et al.[8] in subsection 2.6.1. The results of the measurements of $R(T)$ of the samples NKG11, Nizza and Crumb are shown in fig. 5.1

It is to be expected that due to an increase or decrease in disordering, due to annealing or due to heat pulsing, the peaks should change in height. However it is unclear what mechanism changes the peak positions. However Oberbauer [37] investigated a similar effect in κ -Cl over pressure, for which he gives a theory by Dobrosavljevic and Tanaskovic [38]. As in the phase diagram κ -Cl is a compound similar to κ -Br but set at another pressure and Hartman et al. [8] argue that the increase of disorder acts in a way as opposite to increasing hydrostatical pressure, then the theory by Dobrosavljevic and Tanaskovic [38] might be an explanation for what we observe.

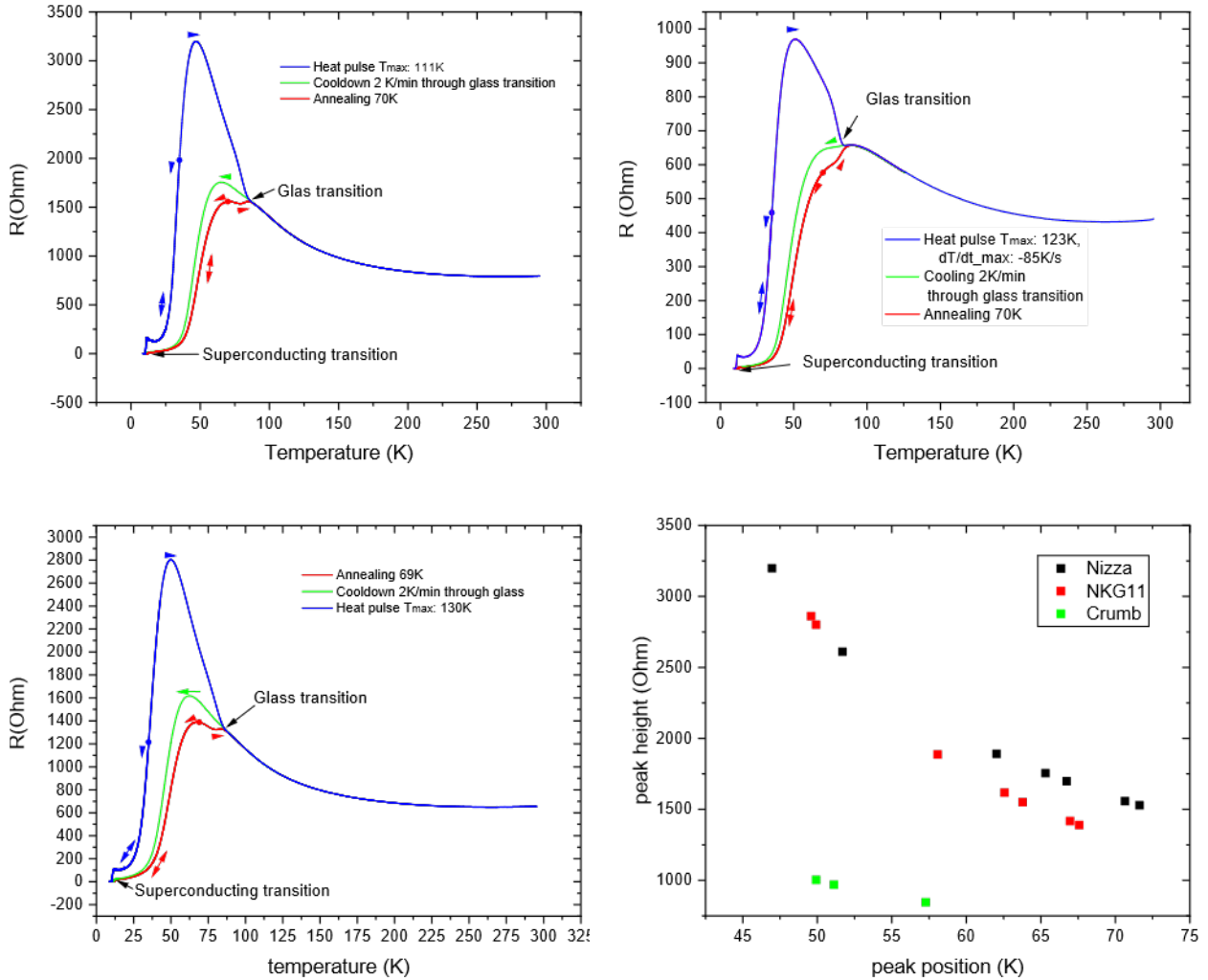


Figure 5.1 $R(T)$ for samples **Upper left:** Nizza, **Upper right:** Crumb, **Lower left** NKG11. The state shown were measured in different ways. The green curve was measured as cooling in from 130 K at a cooling rate of 2K/min. The red curve was an annealing curve were the sample was kept at the temperature of annealing for 12 hours in case of the annealing temperature of 70 K and for 60 hours in case of annealing at 69 K. The filled circle marks the starting temperature of the measurement. The samples where then cooled and the superconducting transition was measured. Afterwards they were heated again till 130 K. The heat pulsed state was measured starting at 35 K after applying at heat pulse as described in the measurement chapter in section 4.5. The sample was cooled to measure the superconducting transition, then warmed again till 130 K. We see that all $R(T)$ curves meet above the glass transition temperature. As we will later show, this change in resistance below the glass transition is perfectly reversible. We further see that the peak in resistance is shifted to lower temperatures and increased in height. We therefore plot the peak resistances over the peak positions for the various states of ordering and disordering prepared for the samples in the **Lower right**.

5.2 Annealing and change in resistance

To better understand the ordering and especially the ordering rates the annealing of the ethylene endgroups of the BEDT-TTF molecules was studied. For this the samples were heated to 100K and then cooled with 1 to $2 \frac{\text{K}}{\text{min}}$ to temperatures in the range of 68 K to 78 K for κ -Br and to 63 K to 70 K for κ -Cl. Then the temperature was stabilized and the change in resistance over time was recorded. Figure 5.2 shows example results of the annealing process.

5.2.1 Fit with one and two exponentials

We see that fitting with an exponential decay with two exponents fits better than fitting with just one exponent for κ -Br, as seen in fig. 5.2. For fitting the ExpDec2 function from Origin was used which is a sum of two exponents with each exponent having its own amplitude pre-factor. This is in agreement with Stalcup et al. [10] who also finds that two exponents explain the resistance over time. For the deuterated κ -Cl a fit with two exponents works better than with one exponent. It is the opposite case for hydrogenated κ -Cl, where a fit with two exponents either collapses to two times the same annealing rate or a second quasi zero amplitude component is the fit result. An explanation for this is that, in reality the resistance decreases with the sum of two exponents but the rates are so similar that it can not be resolved as two exponents.

An explanation for the two different rates can be found in the crystal structure, seen in Fig. 2.1.

We see that the endgroups of the ET molecules have two different surroundings. On one site they are surrounded by the halogen atom and at the other site they are surrounded by the Cu atoms and CN molecules. This modifies the energy barrier and the energy difference between staggered and eclipsed state of the endgroups. We therefore expect two different ordering rates.

5.2.2 Annealing rates

The relaxation times are shown in Fig. 5.3.

We see the quasi exponential dependence of the relaxation time on temperature, which is predicted by Hartman et al. [8]. They define the glass transition temperature T_g as the temperature when the time scales of relaxation are 100 s. In our case this is 80 K for κ -Br and 75 K for κ -Cl.

When heat pulsing the maximal achievable disorder is determined by highest temperature where the cooling rate is roughly the relaxation time. The highest achieved cooling rates were about 400 to 500 $\frac{\text{K}}{\text{min}}$. This means the sample is at that temperature at a window of 1 K for 2 ms. Therefore the relaxation rate should also be in about 2 ms. For a small temperature range we can approximate the formula 2.2 by a simpler exponential law, as we can see in fig. 5.3. Fitting by an exponential law base 10 the relaxation rate $r(T)$,

$$r(T) = 10^{a*T+b}, \quad (5.1)$$

we get for a $-0.174 \pm 0.019 \frac{1}{\text{K}}$ and for b 16.1 ± 1.38 from the rates t1 and a $-0.2094 \pm 0.016 \frac{1}{\text{K}}$ and for b 19.1 ± 1.14 from the rates t2 for κ -Br. This means that the relaxation rate decreases by one order of magnitude roughly every 5.5 K. From fitting t1 of κ -Br this gives an estimated temperature of 108 K and from t2 this gives 104 K.

For fully hydrogenated κ -Cl we get for a $-0.225 \pm 0.014 \frac{1}{\text{K}}$ and for b 18.6 ± 0.96 from the rate t1. This means the relaxation rate decreases by one order of magnitude roughly every 4.4 K and we get an estimated maximal temperature for the heat pulse of 95 K.

From fitting fully deuterated κ -Cl we get for a $-0.226 \pm 0.023 \frac{1}{\text{K}}$ and for b 18.7 ± 1.53 from the rates t1 and a $-0.233 \pm 0.029 \frac{1}{\text{K}}$ and for b 19.7 ± 1.93 from the rates t2. The relaxation rate changes by order of magnitude roughly every 4.3 K and we get an estimated temperature of 95 K from t1 and from t2 roughly 96 K.

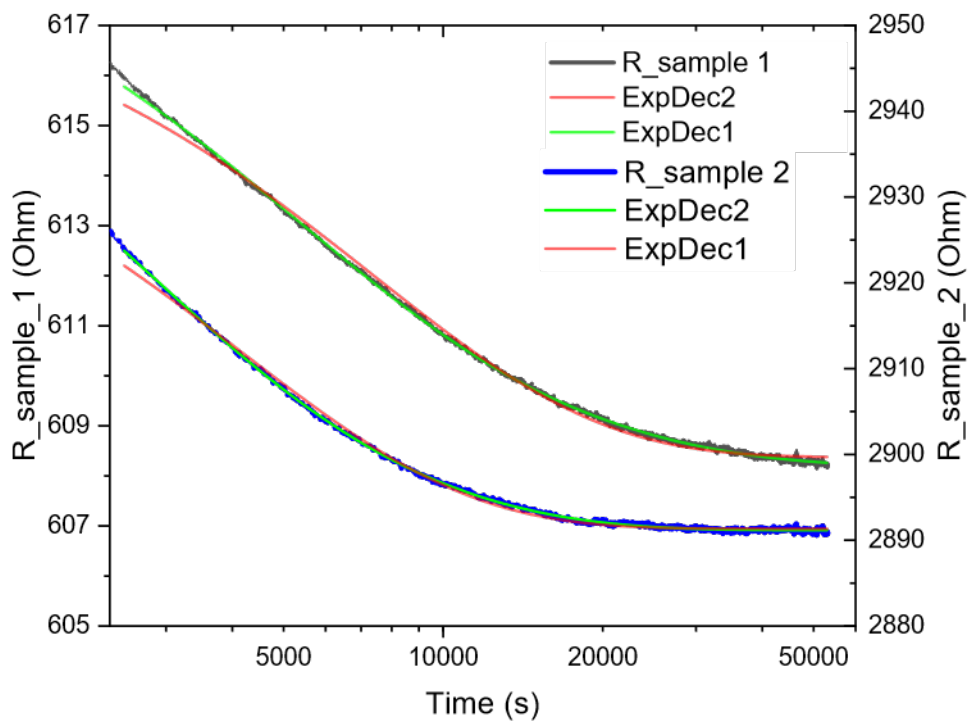
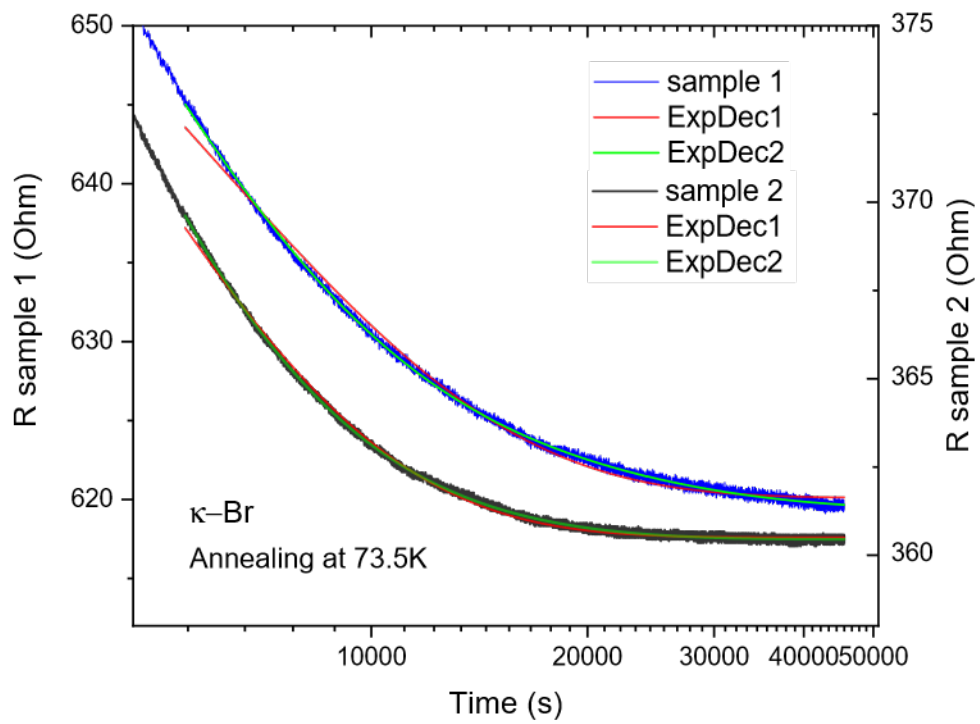


Figure 5.2 Upper resistance over time for κ -Br, Lower resistance over time hydrogenated and fully deuterated κ -Cl. Sample 1 is fully deuterated while sample 2 is fully hydrogenated

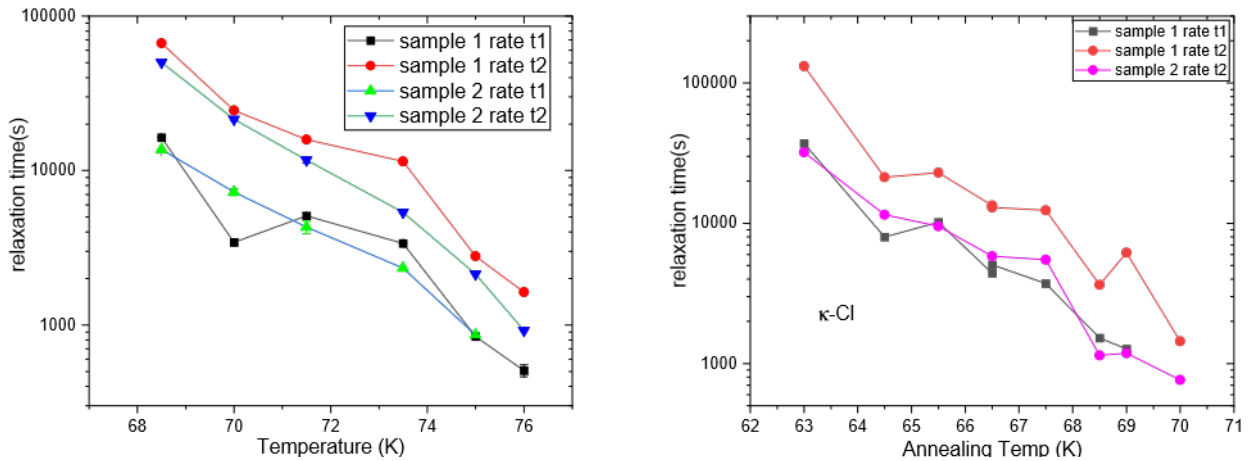


Figure 5.3 Upper Left relaxation times for κ -Br measured for samples Hepheistos (sample 1) and sample Crumb (sample 2) **Upper Right** relaxation times for fully hydrogenated and fully deuterated κ -Cl. Secret hero (sample 1) is fully deuterated while Superhero (sample 2) is fully hydrogenated

However the exact theory in Hartman et al. [8] for τ_{eff} is a sum of two exponents which means that the relaxation rate goes slower to 0 than from this estimate, therefore reaching higher temperatures by the heat pulse still might give a higher disorder.

5.2.3 Annealing under pressure

The annealing was measured in a pressure cell for the κ -Cl which means a worse thermalisation between samples and thermometer. This is the reason why there is a bigger variance in the relaxation time measurement results compared to κ -Br. Due to this all measurements of annealing of κ -Br were done without the pressure cell. For comparison also the general study of annealing of κ -Cl was done at ambient pressure. However, measuring in the pressure cell allowed to measure also annealing under pressure to check if the relaxation times are significantly different. To check this the annealing was measured at 66.5 K at ambient pressure and at 375 bar. It was found that the relaxation times do not significantly differ.

5.2.4 Change of amplitude during annealing

Last in this section we want to talk about the change in resistance during annealing. As a quasi instant temperature stabilization is not possible, the change in resistance during annealing depends on the time needed to stabilize. During this time already the endgroups are annealed. Therefore the true change in resistance from annealing any disordering is unknown but knowing the relaxation rates most of the annealing prior to happens during going through the higher temperatures, which is similar for most stabilization temperatures. Only for the highest temperatures the stabilization happens where the relaxation times are short. This means that the amplitude of the change of resistance during annealing is decreased for these temperatures, as a significant part of the annealing has already happened before stabilization.

The change in resistance relative to the annealed resistance is shown in Fig.5.4

Comparing κ -Cl and κ -Br, we see that the effect of annealing on resistance is stronger in κ -Br. Further we see a exponential dependence of the amplitude with temperature for κ -Br.

Looking at the formula for the time dependent resistance 3.4, we see that the amplitude of the time dependent part is a constant, times the difference in occupation of the ground state of the ethylene end groups $\rho_E^\infty(T_1) - \rho_E^\infty(T_0)$, with T_0 the temperature corresponding to the occupation of the ground state at annealing begin. As the relaxation time increases exponentially with decreasing temperature, there should be not much more annealing happening when stabilizing for annealing for lower than for higher

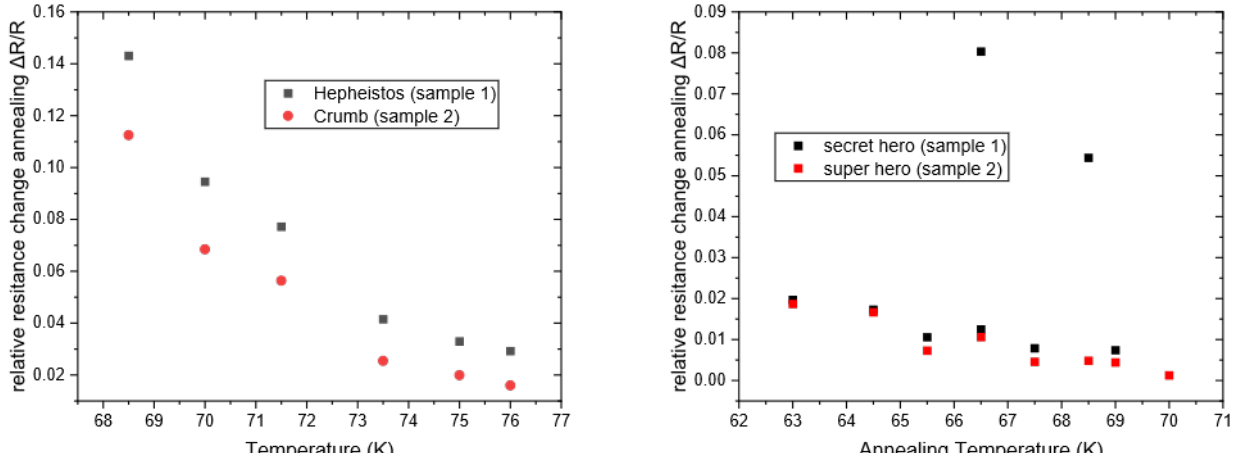


Figure 5.4 Left relative change in resistance for κ -Br measured for samples Hepheistos (sample 1) and sample Crumb (sample 2) **Right** relative change in resistance for fully hydrogenated and fully deuterated κ -Cl. Secret hero (sample 1) is fully deuterated while Superhero (sample 2) is fully hydrogenated. Noteworthy is that the high values at 66.5 K and 68.5 K are from annealing quenched states that were prepared via heat pulse.

temperatures, even the stabilization takes longer due to having to sweep to a lower temperature. We get using equation 2.1

$$\rho_E^\infty(T_1) - \rho_E^\infty(T_0) = \frac{1}{1 + e^{-\frac{2\Delta E}{k_B T_1}}} - \frac{1}{1 + e^{-\frac{2\Delta E}{k_B T_0}}} = \frac{e^{-\frac{2\Delta E}{k_B T_0}} - e^{-\frac{2\Delta E}{k_B T_1}}}{\left(1 + e^{-\frac{2\Delta E}{k_B T_1}}\right) \left(1 + e^{-\frac{2\Delta E}{k_B T_0}}\right)} \quad (5.2)$$

Setting $T_1 = T_0 + \Delta T$, we can rewrite $e^{-\frac{2\Delta E}{k_B T_1}}$ to get

$$e^{-\frac{2\Delta E}{k_B T_1}} = e^{-\frac{2\Delta E}{k_B T_0} \left(1 - \frac{\Delta T}{T_0}\right)} \quad (5.3)$$

using $\frac{1}{1+x} \approx 1 - x$ for small x . This is the case here as ΔT is much smaller than the starting temperature of the stabilization T_0 . Combining this with the equation above we get

$$\rho_E^\infty(T_1) - \rho_E^\infty(T_0) \approx \frac{e^{-\frac{2\Delta E}{k_B T_0}} \left(e^{-\frac{2\Delta E}{k_B T_0} \left(1 - \frac{\Delta T}{T_0}\right)} - 1 \right)}{\left(1 + e^{-\frac{2\Delta E}{k_B T_1}}\right) \left(1 + e^{-\frac{2\Delta E}{k_B T_0}}\right)}. \quad (5.4)$$

$\rho_E^\infty(T_1) - \rho_E^\infty(T_0)$ does not change a lot as seen in fig. 2.2, therefore we can assume the denominator to be constant. This simplifies for fitting to

$$\rho_E^\infty(T_1) - \rho_E^\infty(T_0) \approx a * e^{-\frac{2\Delta E}{k_B T_0} \frac{\Delta T}{T_0}} - c. \quad (5.5)$$

For the κ -Br samples we get $a=0.00701 \pm 0.00535$, $\Delta E/ = 70.7 \pm 16.4$ meV and $c=0.00834 \pm 0.01342$ for sample Hepheistos and for sample Crumb we get $a=0.00439 \pm 0.0041$, $\Delta E/ = 77.0 \pm 20.5$ meV and $c=0.00206 \pm 0.01182$, assuming a starting temperature T_0 of 80 K. This is in agreement with Hartman et al.[8] who give a ΔE of 90.5 ± 4.3 meV while Guterding et al.[14] find 110 meV for ΔE by DFT. Hartman et al.[8] found their value for ΔE of 90.5 ± 4.3 meV from synchrotron x-ray diffraction done by Wolter et al. [13]. Synchrotron x-ray diffraction is better suited for finding ΔE which results in a lower error bar. We can see that our result for ΔE is within error bars.

The dependence of the amplitude of annealing of κ -Cl on temperature is almost linear, which might be due to the much more difficult stabilization of temperature when using the pressure cell. This then leads

to a larger variation of the measured amplitudes of annealing and this variation may therefore cover an exponential dependence. Therefore also for these relative changes in resistance are fitted with equation 5.5.

For the κ -Cl samples we get $a=0.0025\pm 0.0083$, $\Delta E/ = 43\pm 54$ meV and $c=-0.0001\pm 0.01595$ for sample secret hero and $a=0.00511\pm 0.01304$, $\Delta E/ = 34.1\pm 38.3$ meV and $c=-0.00849\pm 0.01965$ for sample Hephheistos, assuming a starting temperature of 75 K. The huge error bars are due to the difficulties in stabilizing and the huge variance in relative resistance change observed. Guterding et al.[14] find 72 meV for ΔE by DFT, which is not to far away.

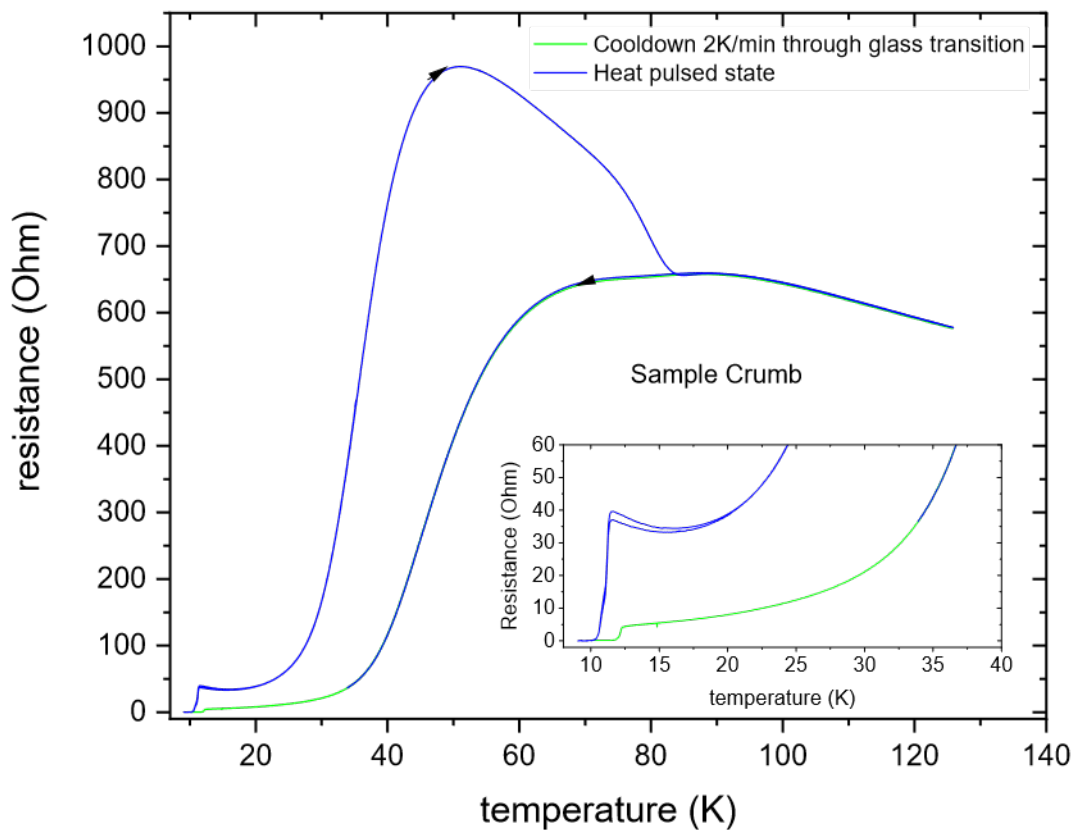


Figure 5.5 $R(T)$ after heat pulse in blue and $R(T)$ before heat pulse in green. $R(T)$ after the pulse is done by first cooling from 35 K after the pulse down through T_c , then go to 100 K and then cool down again. The two curves need to be taken with the same cooling rate otherwise the different annealing processes will lead to different resistances.

5.3 Heat pulses

We now want to look at the heat pulse and its effects. It was already briefly discussed in section 4.5. A figure of a heat pulse and its details are explained there. Further heat pulses are seen in figure 5.8.

5.3.1 Reversibility of the heat pulse

To make sure the samples do not sustain any damage like micro-cracks and change their resistance due to the damage, the effect of the heat pulse is reversed by heating the sample to 100 K and then cooling it again. The resistance curve is then compared to a resistance curve taken before the heat pulse which was cooled with the same cooling speed. This can be seen in fig. 5.5. The two curves lie perfectly on each other when comparing to the part of cooling after the heat pulse from 100 K down. Therefore the original state of the sample can be restored.

5.3.2 Rates of cooling and heating during and after the heat pulse

To give an idea of the cooling and heating rates involved, in the following the results from processing the heat pulse of sample NKG11 are discussed. The heat pulse had duration of 2 s and a pulse voltage of 7.50 V. A picture of $R(T)$ for NKG11 can be seen in fig. A.1. Qualitatively it looks similar to the curve of sample Nizza seen in fig. 5.7 on the lower right. We see that the temperature rises quickly in the beginning

of the pulse were the resistance is low and the temperature difference to the cooling bath is low as seen in fig. 5.6 on the upper left. The heating rate then gradually decreases and comes to a halt at around 1.5 s as seen from the middle of fig. 5.6. Therefore the sample is almost in a thermal steady state at the end of the pulse at 130 K. It is noteworthy the difference in the maximum temperature found during the pulse and after the pulse as seen on the top row of fig. 5.6. This difference is from the time during the switching off of the dc bias voltage, which due to the high cooling rates already allows for a significant cooling of the samples. We can extrapolate the cooling rate from the lower right of fig. 5.6 and get around 420 K/s at 130 K. This means the blind time during switching off the dc bias is around 50 ms and the maximal achieved cooling rate is 420 K/s. It may be that the cooling rate is even higher than extrapolated as the cooling bath is cooler just after switching off the pulse. Calculating the $T(t)$ during cooling is made difficult above the glass transition as in the cooling phase of the heat pulse the disorder is frozen in while during measuring $R(T)$ after the pulse when going above the glass transition the disorder is relaxed leading to a different $R(T)$ than with constant disorder.

5.3.3 Achievable disorder depending on the maximal temperature of the heat pulse

We want to know the maximal temperature heating up to which increases the achieved disorder by heat pulsing. In subsection 5.2.1 we already gave a lower estimate for the maximal temperature of the heat pulse up to which a heat pulse should increase the disorder. In fig 5.7 we see the achieved disorder as the ratios between resistance at 35 K, the starting temperature of the heat pulse, which is measured in every heat pulse and the resistance at 35 K from cooling with 2 K/min. 1 to 2 K/min is the cooling rate which we define as normally cooled. Further the figure shows the ratios of the residual resistance, which is the resistance at 0 K when only the defect scattering remains. The extrapolation to 0 K was done by fitting the resistance over temperature at 13 to 20 K with the formula

$$R(T) = a \cdot e^{T/b} + c \quad (5.6)$$

with fitting parameters a , b and c and then evaluating the fit at 0 K. We find that the maximal achievable ratio at 35 K is around 15 for samples Crumb and Nizza and 8 for sample NKG 11. The maximal residual resistance ratio is around 35 for samples NKG 11 and Nizza and 21 for sample Crumb. It is for further studies to decide which part of this is to be attributed to the change in the phase diagram towards the metal insulator transition and which part to the increase of defect scattering.

We find that the ratio does not increase when going beyond a maximal heat pulse temperature of 120 to 130 K. As the number of data points is somewhat limited and the heat pulses were done in different environments we can conclude that the upper limit for the temperature is 120 to 130 K. The lowest temperature for which we found a change in resistance was approximately 82 K, where the ratio was close to a few percent above 1. This means that the temperature range for the maximal temperature for heat pulses is 80 K to 120 till 130 K. Going above this temperature does not increase disorder, however it increases the thermal stress on the sample. Actually as seen in fig. 5.8 going to a higher temperature decreases disorder. The heat pulses were done in a row with increasing pulse voltage, where the achieved maximal temperatures are noted for each pulse. We see that the final resistance during applying the pulse voltage decreases with increasing voltage which means an increase in temperature. The temperature can be read from the resistance over temperature graph for the sample shown in the lower right (d) in fig. 5.7. This can be verified by the fact that the starting resistance seen on the left of fig. 5.8 is the final resistance of the previous pulse on the right. The final resistance after cooling increases, when increasing the voltage from 6 V to 6.4 V, but decreases when going from 6.4 V to 7 V. This is as the relaxation rate at temperatures above 120 K to 130 K are much faster than the cooling rate and the occupation probability of ground state of the ethylene endgroups relaxes almost immediately to exactly the steady state occupation. Therefore the disorder at temperatures above 130 K is relaxed during cooling. However the surroundings of the sample are heated more when going to temperatures above 120 to 130 K and therefore the cooling bath is hotter leading to a lower cooling rate below 120 to 130 K.

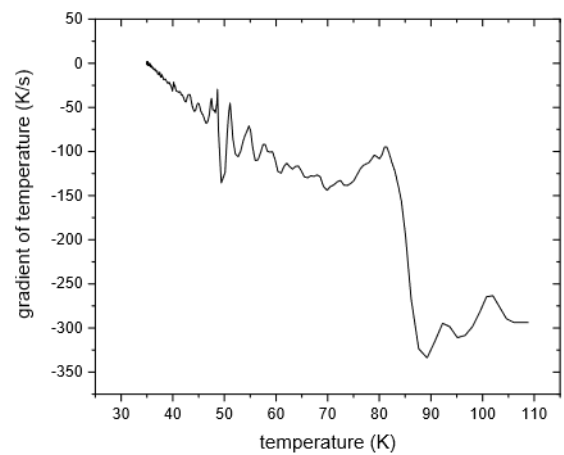
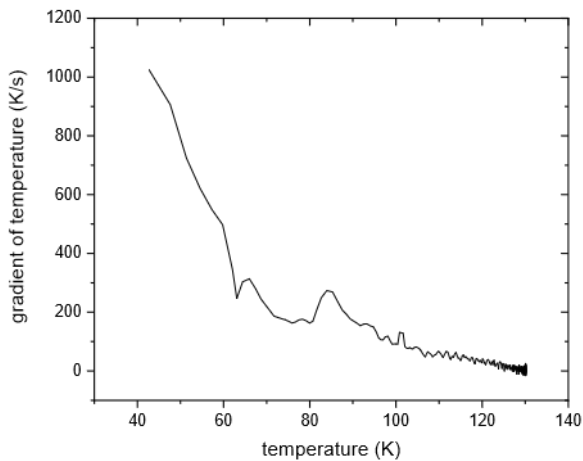
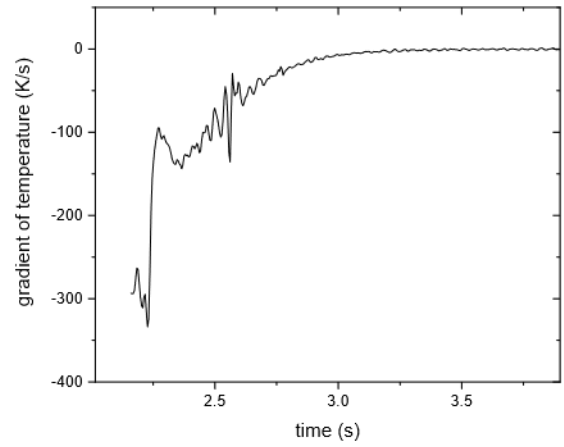
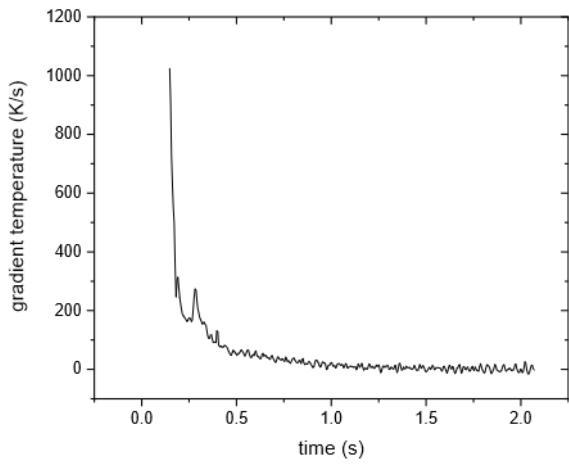
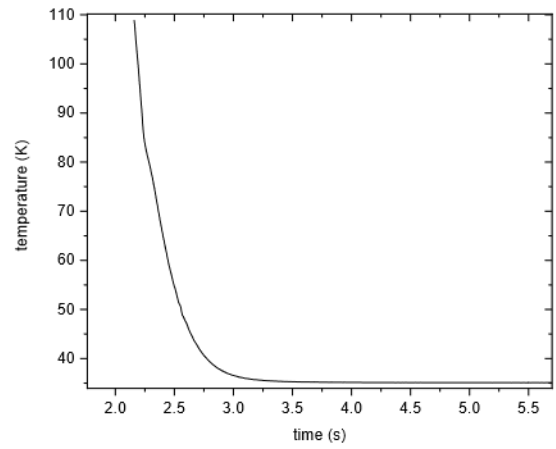
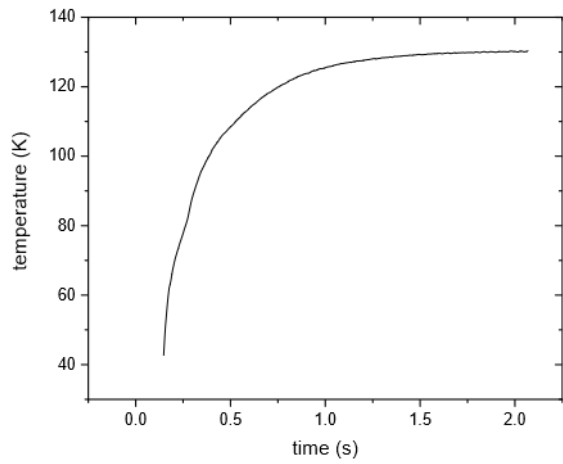


Figure 5.6 The left column is during the pulse and the right column is after the pulse **Upper row:** temperature over time during and after the pulse. Especially during the pulse the first few measurement points are somewhat incorrect. **Middle row:** Gradient of temperature over time. The first points especially during pulse have a large error bar and should serve more as estimate. **Lower row:** Gradient of temperature over temperature

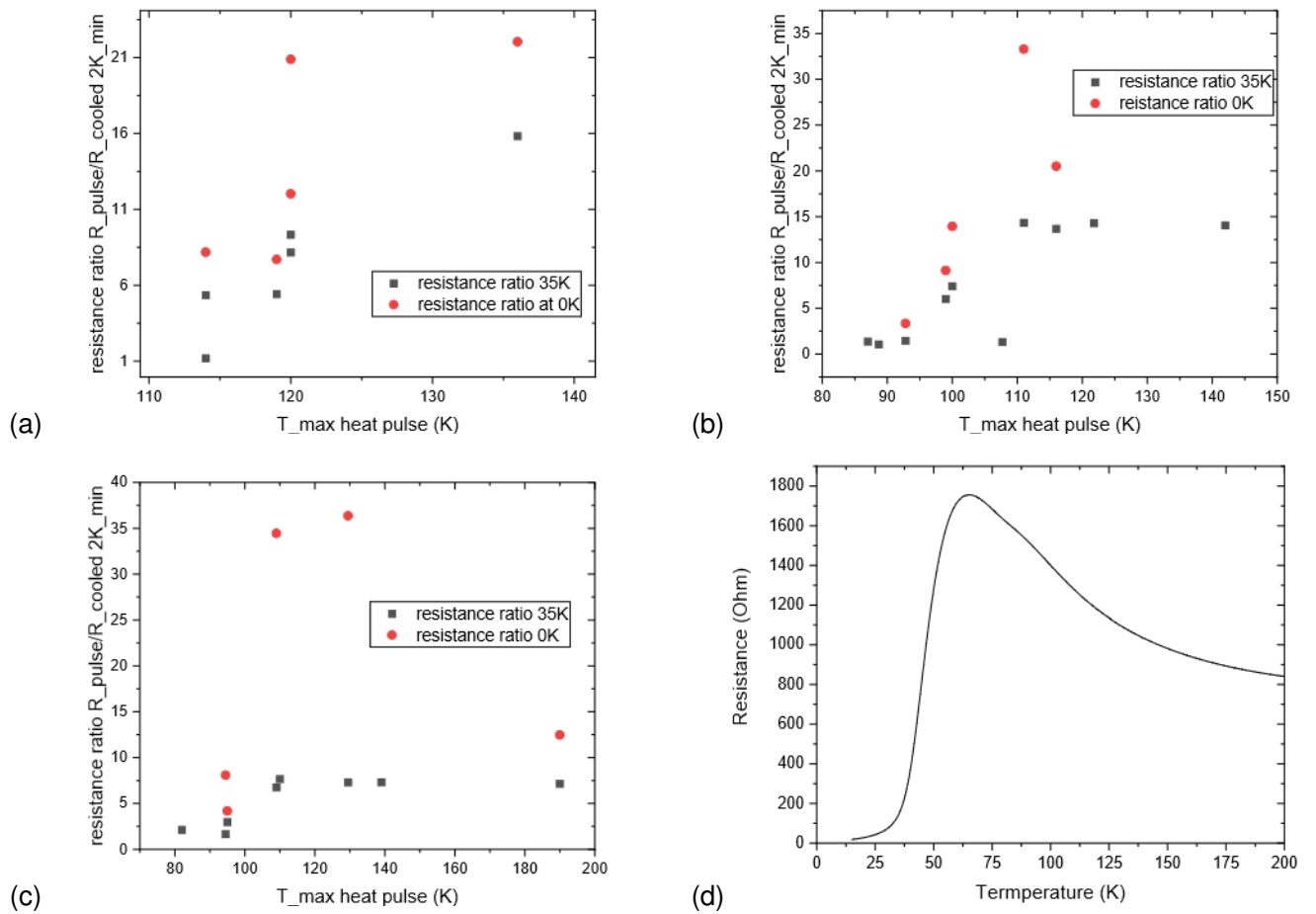


Figure 5.7 Resistance ratios of the samples relative to the state cooled with a cooling rate of 2 K/min through the glass transition range. Given are the resistance ratios at 35 K the starting temperature of the heat pulse and for the resistances extrapolated to 0 K. The heat pulses in Garching were done in a atmosphere of 100 mbar Helium, while the heat pulses in Dresden were done in 45 to 50 mbar ^3He **Upper Left (a)** resistance ratio for sample Crumb. Not shown is a point at 85 K where the resistance ratio is 1.036 at 35 K **Upper right (b)** resistance ratio for sample Nizza **Lower left (c)** resistance ratio for sample NKG11 **Lower right (d)** resistance over temperature for sample Nizza with a cooling rate of 2 K/min per minute through the glass transition.

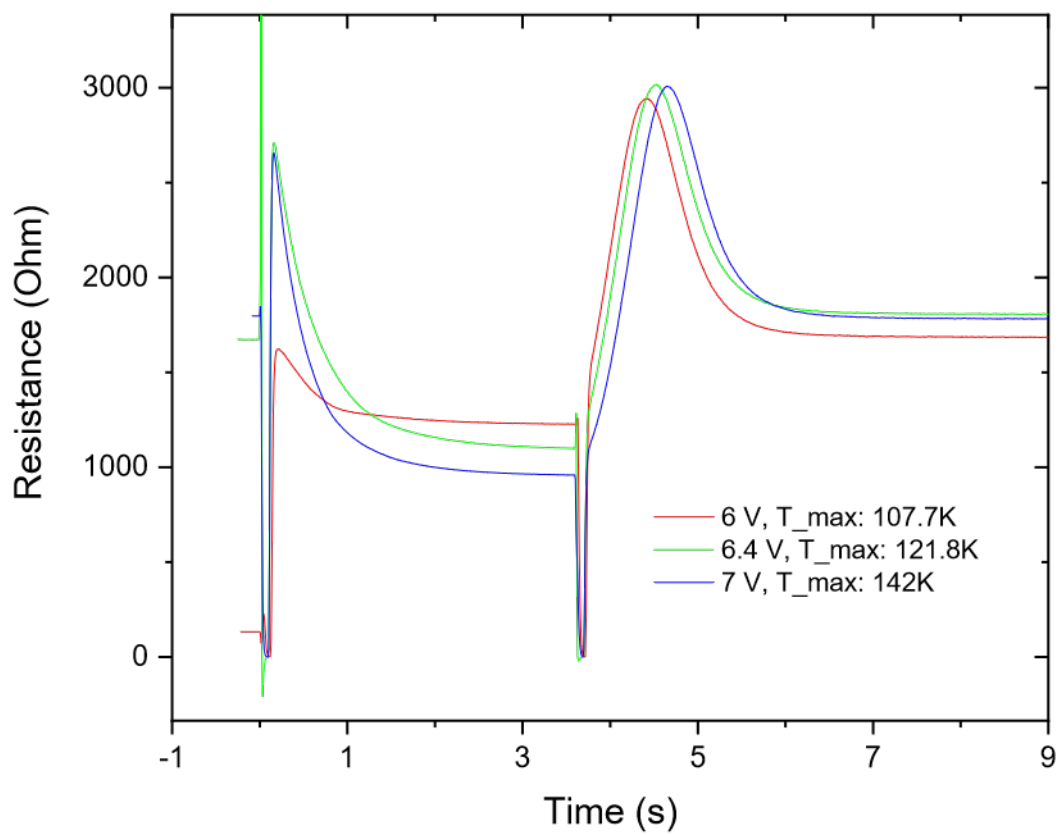


Figure 5.8 Heat pulses of the sample Nizza, with a starting temperature of 35 K and 100 mbar Helium in the sample space.

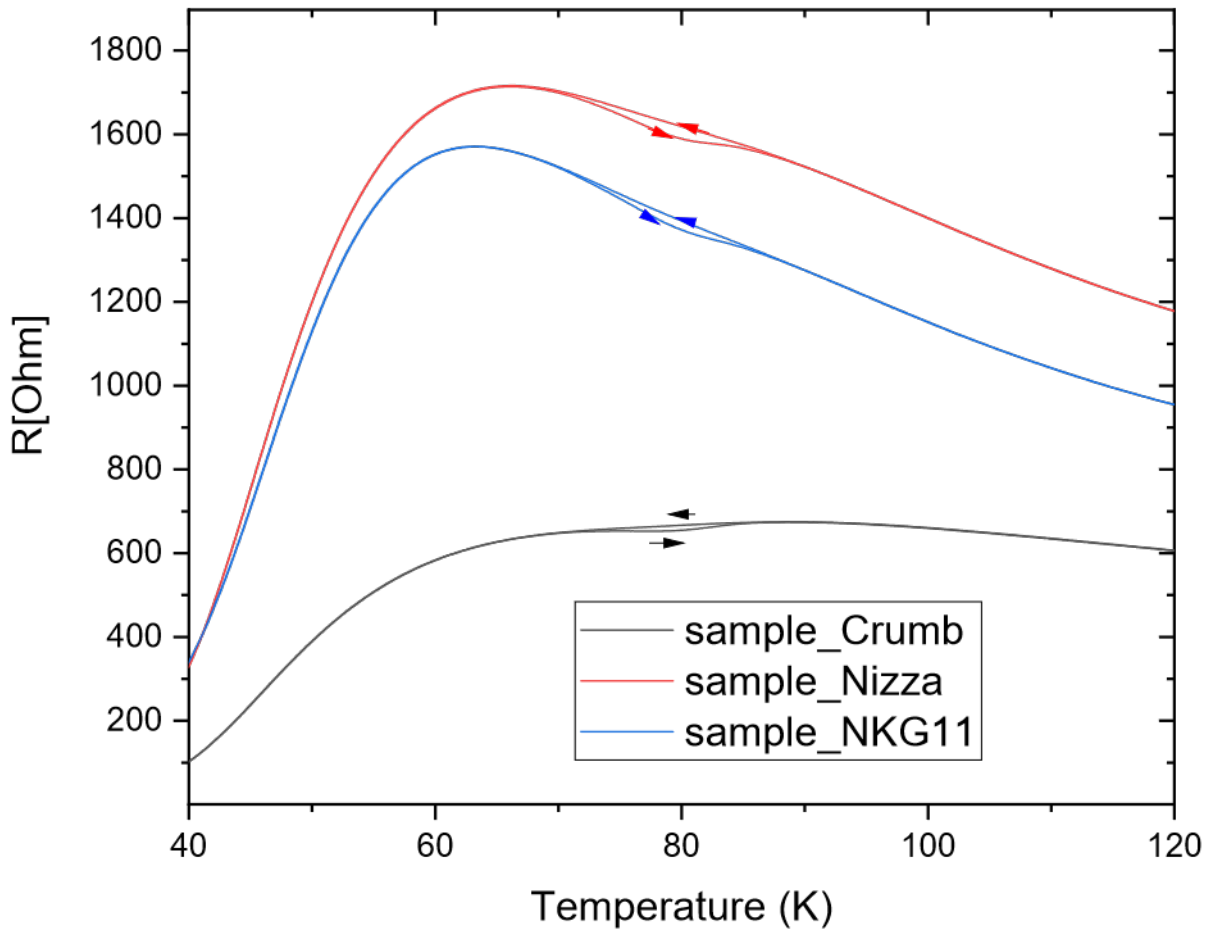


Figure 5.9 Cooling and warming curves of samples Crumb, NKG 11 and Nizza with speed of 1 K/min. The arrows indicate the direction of the change of temperature.

5.4 Hysteresis in the resistance in the glass transition range

5.4.1 Hysteresis in κ -Br

Upon warming the sample Crumb shows a "hump" compared to the cooling curve at around 80K as seen in Fig. 5.9. This "hump" was already reported by Hartman et al.[8] for partially deuterated κ -Br. When comparing cooling and warming curves of the samples with the same speed of cooling and warming and no other thermal treatment done, one can see that in fact there is a hysteresis. This hysteresis is visible even when no "hump" shows up as for samples Nizza and NKG11.

To analyse this, the warming curve is subtracted from the cooling curve. A linear polynomial is fitted to areas away from the hysteresis to remove the sweep induced hysteresis. As the effect should be more or less proportional to sample resistance, the difference is normalized to the cooling curve resistance. The cooling curve does not show the hump therefore it is better suited for normalization. Doing this we get a peak at around 80 K as seen in Fig.5.10, with every sample having about the same peak height.

The difference in peak temperature is seen in Fig. 5.10. It may be explained by the fact that the glass transition temperature depends on the cooling rate as shown in Scherer's book "Relaxation in glass and composites" [26, chapter9]. Formula 9.35 from this book for the difference between glass transition temperatures is

$$T_g(q_2) = T_g(q_1) - \frac{1}{A} \ln \left| \frac{q_1}{q_2} \right| \quad (5.7)$$

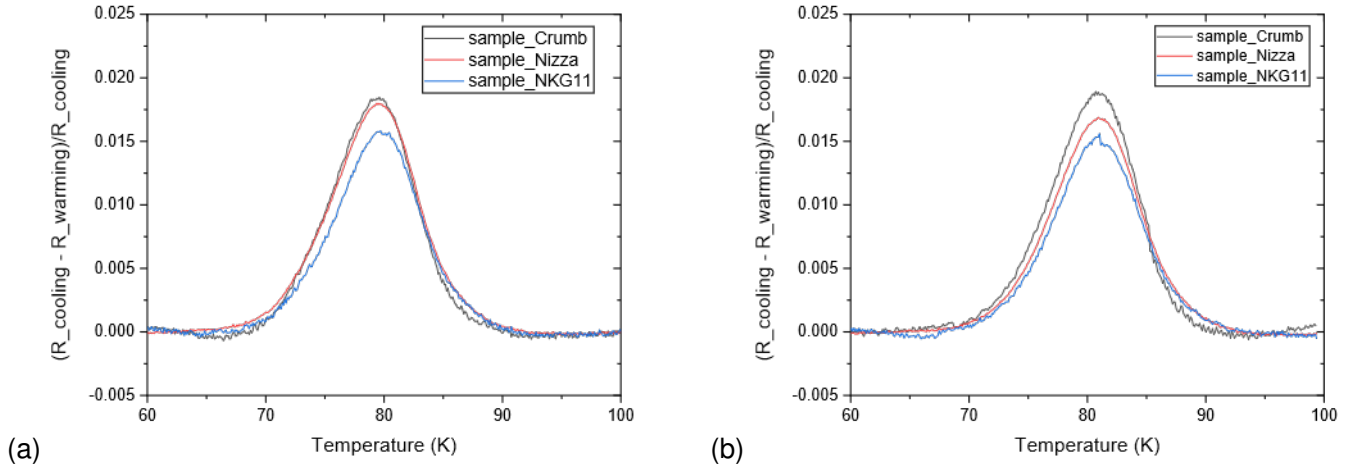


Figure 5.10 Normalized hysteresis. **Left (a)** A sweep speed of 1 K/min. We get peak temperature height pairs, 79.34 ± 0.013 K with height 1.826 ± 0.0043 % for sample Crumb, 79.507 ± 0.007 K with height 1.79 ± 0.002 % for sample Nizza and 79.71 ± 0.011 K with height 1.567 ± 0.003 % for sample NKG11. **Right (b)** Sweep speed 2 K/min. We get peak temperature height pairs 80.80 ± 0.012 K with height 1.865 ± 0.0040 % for sample Crumb, 80.89 ± 0.0011 K with height 1.666 ± 0.003 % for sample Nizza and 80.92 ± 0.012 K with height 1.50 ± 0.003 % for sample NKG11

with q_i the cooling rates, $T_g(q_i)$ the cooling rate dependent glass transition temperatures and A a material specific constant. The constant A is from the relaxation time where formula 9.26 in [26, chapter9] is

$$r(T) = r_0 e^{-AT}, \quad (5.8)$$

were we kept our name for the relaxation rate from the equation 5.1. This formula we have already seen is applicable in the vicinity of T_g , as also Scherer states. This now can be used to calculate A from comparing coefficients getting $A = \ln(10)a$. We get $A = 0.401 \pm 0.044 \frac{1}{K}$ from t_1 and $A = 0.482 \pm 0.037 \frac{1}{K}$ from t_2 . This then evaluates for

$$T_g(q_2) - T_g(q_1) = -\frac{1}{A} \ln \left| \frac{q_1}{q_2} \right| \quad (5.9)$$

to the absolute values of the difference to 1.72 ± 0.19 K from t_1 and 1.43 ± 0.11 K from t_2 . Here the error propagation with the formula

$$u(T_g(q_2) - T_g(q_1)) = \left(\frac{u(A)}{A^2} \right) \quad (5.10)$$

from [39, page 12] was used with $u(A)$ the uncertainty of A and assuming the cooling rates to be exact as they should be already in a steady state with little uncertainty. If the cooling rates have a significant uncertainty, then the uncertainty given here is just a lower bound for the uncertainty of the difference of the glass transition temperatures. Comparing to the peak differences of 1.46 ± 0.018 K for sample Crumb, 1.38 ± 0.013 K for sample Nizza and 1.21 ± 0.018 K for sample NKG11, this is somewhat different for the result from t_1 but partially in good agreement with the result from t_2 . One has to take into account that the situation in [26, chapter9] is for a single exponent with one relaxation rate, therefore our situation should be somewhat different. But due to the two exponents being close, the result should be not too far off from the situation with one exponent. The difference of the height of the peaks may be either a sweep hysteresis due to sample and thermometer temperature mismatch, which the linear polynomial failed to remove or be due to the change in glass transition temperature.

It has been reported by Kund et al. [40] and Müller et al. [15] that the thermal expansion coefficient becomes discontinuous at around 80 K. Kund et al. find that the transition marked by the discontinuity of the thermal expansion coefficient is a second order transition. Kund et al. further report a hysteresis in the resistance however their hysteresis looks different to the hysteresis we found. Tanatar et al. [41] report the warming part of the hysteresis for fully hydrogenated κ -Br and Hartman et al. [8] report the warming part of the hysteresis for their partially deuterated sample κ -Br sample.

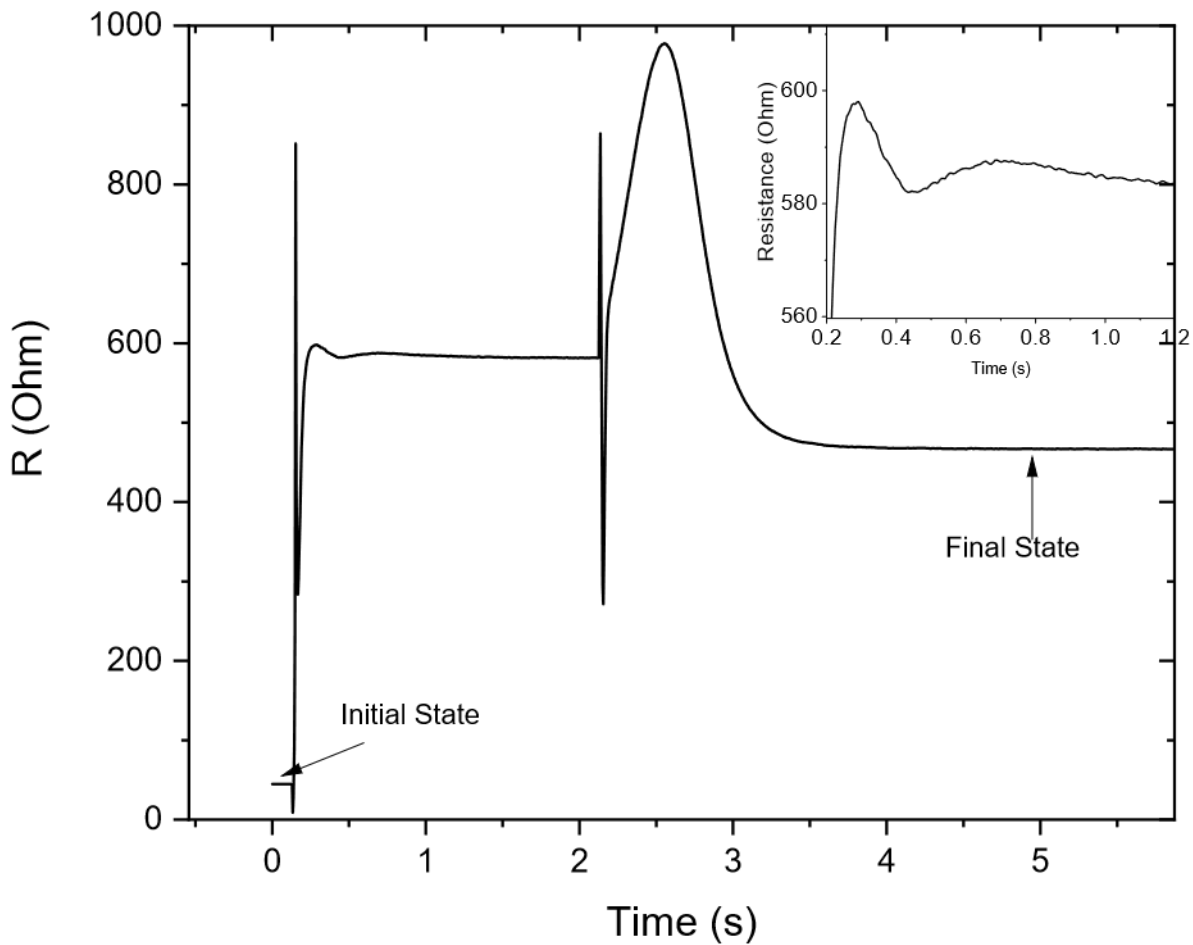


Figure 5.11 Heat pulse of sample Crumb, starting at 35 K, with a starting resistance of 44.7 Ohm and a final resistance after the pulse of 466.7 Ohm, both at 35 K. The pulse duration was 2 s with a voltage of 6 V. The insert shows the first part of the pulse where the warming part of the hysteresis is visible.

Hysteresis visible in heat pulse

The advantage of the heat pulse technique used in this thesis is that it can measure the resistance during the warming phase with high resolution. On sample "Crumb" the hysteresis is easily visible on a heat pulse as seen in fig. 5.11, as the warming part of the hysteresis leads to first a positive, then a negative, then a positive and then a negative $\frac{dR}{dT}$, as can be seen in fig. 5.9. It is not easy to detect the warming part of the hysteresis without these two zero transitions of $\frac{dR}{dT}$, as there is only a change in the amplitude of $\frac{dR}{dT}$ to be seen. This is the case for samples Nizza and NKG11, as visible in fig. 5.9. This change in the amplitude of $\frac{dR}{dT}$ then translates to a change of $\frac{dR}{dt}$ in the pulse, which might be confused with a feature in $\frac{dT}{dt}$ that leads to a feature in $\frac{dR}{dT} \frac{dT}{dt}$.

At the glass transition, the sample can have a warming rate of several hundred $\frac{K}{s}$, which changes the glass transition temperature by formula 5.7. Looking at the warming rates in fig. 5.6, we estimate a warming rate at the glass transition of several hundred K/s. Assuming a warming rate of $300 \frac{K}{s}$ we get an increase of the glass transition temperature to about 90 K. At this temperature the relaxation times should be at the order of seconds. Therefore the relaxation rates at the feature at 0.5 s in fig. 5.11, should still be on the order of seconds or more and due to which no significant amount of annealing or un-annealing happens during the feature. This then means that the hysteresis may not be due to ordering or disordering processes.

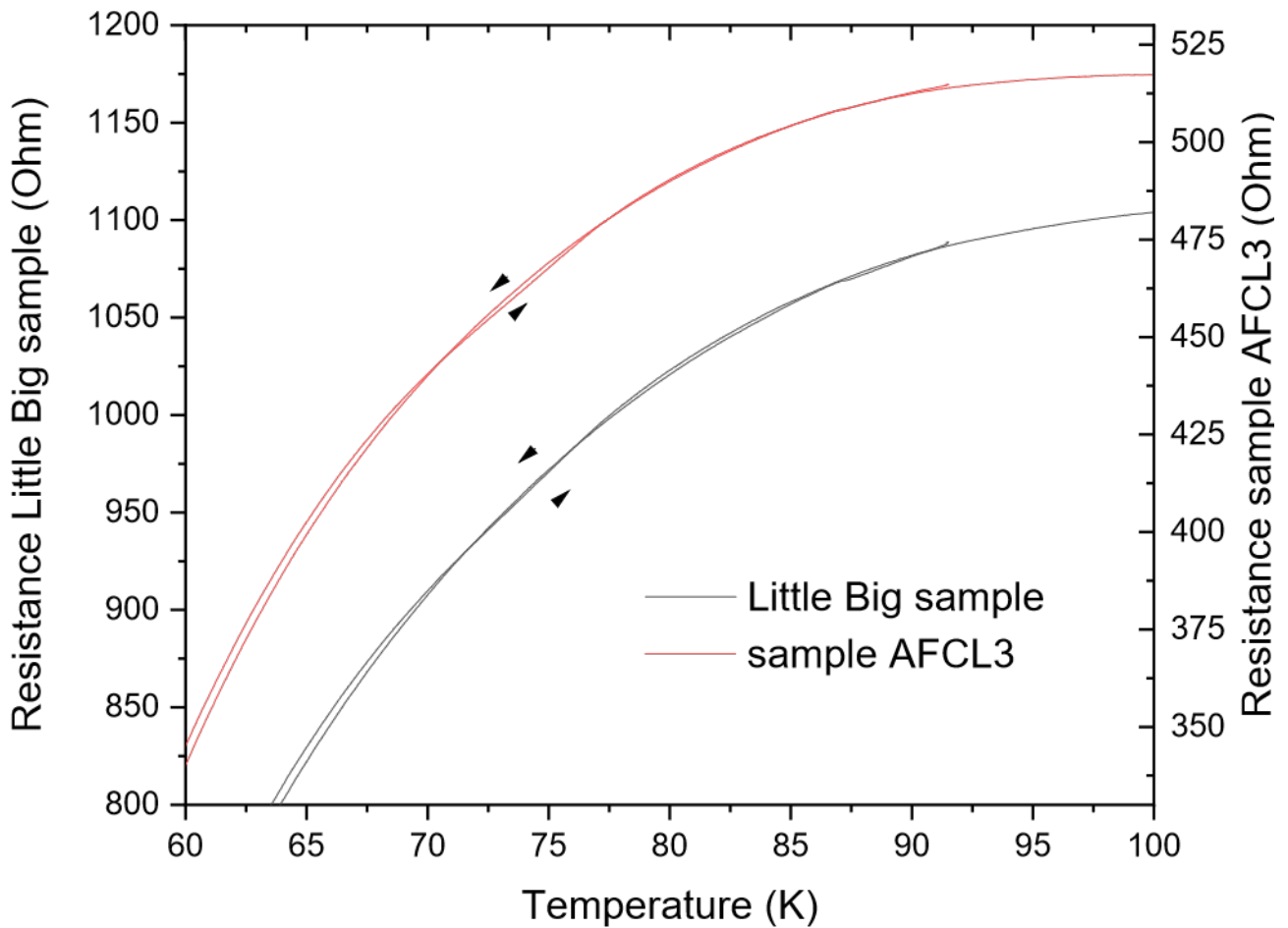


Figure 5.12 Cooling and warming curves of Little Big sample and sample AFCL3 with speed of 1 K/min. The arrows indicate the direction of the change of temperature.

5.4.2 Hysteresis in κ -Cl

Due to the similar nature of κ -Cl and κ -Br one would guess that there should also be a hysteresis visible at the glass transition. Also Müller et al. [15] report a hysteresis in the thermal expansion coefficient at the glass transition temperature. At 350 bar a hysteresis in the resistance at the glass transition is observed, shown in Fig. 5.12. After the same analysis as for κ -Br we get a peak at around 75 K as seen in Fig. 5.10. The height of the peak is only about 0.7 % for κ -Cl, much lower than the 1.7 % for κ -Br.

To check if the peak position difference can be explained by the change in glass transition temperature we do the analysis as for κ -Br. We get $A = 0.518 \pm 0.032 \frac{1}{K}$ and calculate $T_g(q_2) - T_g(q_1)$ getting $1,338 \pm 0.083$ K. Comparing to the result from the distance between peaks from fig. 5.13 we get 0.82 ± 0.017 K and 0.78 ± 0.016 K which is somewhat off. It may however be that removing the hysteresis from the temperature mismatch between samples and thermometer introduced a shift on the peaks. Scherer in his book [26, chapter 9] says that in some cases it was found to be necessary to do a more complex model for the glass transition which he gives there. This may be the case here. Otherwise it is possible that the effects seen here are simply not completely explainable by the change in glass transition temperature. The peak heights also change. This may be either an artefact from temperature sweep hysteresis removal or it may be due to the change in glass transition temperature, where the effect behind this hysteresis depends on the (glass transition) temperature.

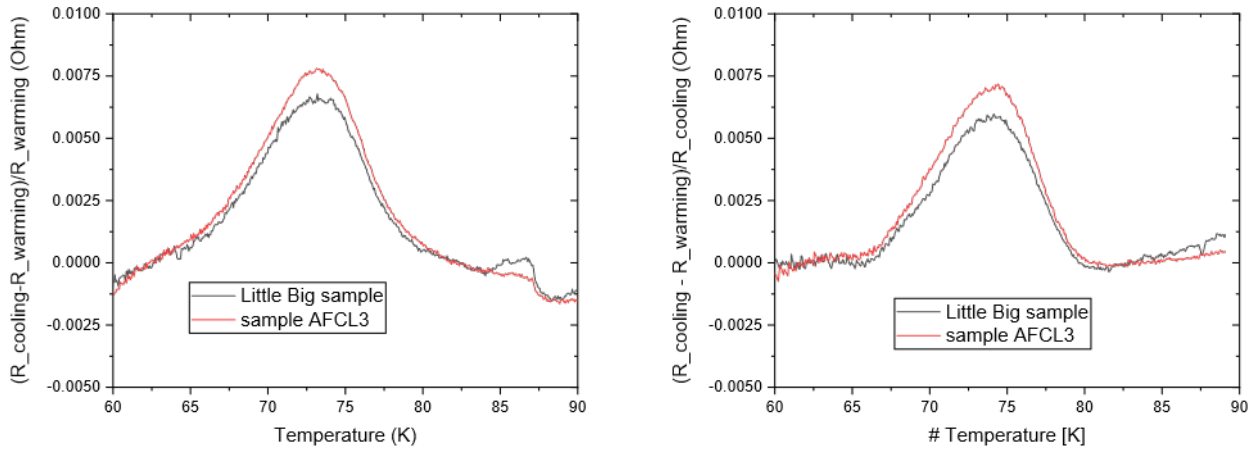


Figure 5.13 Normalized hysteresis. **Left** 1 K/min cooling rate. We get peak temperature height pairs at 73.09 ± 0.010 K with heights of $0.77 \pm 0.015\%$ for sample AFCL3 and 73.01 ± 0.012 K with height of $0.66 \pm 0.017\%$ for Little Big sample **Right** 2 K/min cooling rate. We get peak temperature height pairs at 73.91 ± 0.014 K with height $0.70 \pm 0.020\%$ for sample AFCL3 and 73.79 ± 0.011 K with height $0.58 \pm 0.015\%$ for Little Big sample. Here the peak heights and positions were obtained by fitting with a parabola.

5.4.3 Change of the hysteresis in κ -Cl under pressure

Upon a second cooling of the samples, the thermometer was remounted to the cell at a slightly different position. This change in position reduced the temperature sweep induced hysteresis due to a mismatch of thermometer and sample temperature drastically, allowing for much better investigation of the hysteresis. A hysteresis was found also for the ambient pressure state of κ -Cl which was not visible in the first cooling. The normalized hystereses are shown in fig. 5.14

We see that the center of the peak moves to a higher temperature with increasing pressure as does the lower pressure end of the hysteresis. However the higher pressure end of the hysteresis stays at the same temperature independent of pressure. This in effect decreases the width of the hysteresis. We can extract the peak heights and positions by fitting with a parabola. The results are shown in fig. 5.15

The peak position moves to a higher temperature however there is no clear dependence that would allow a fit. A parabola or $(1 + x^2)^{(1/2)}$ both might describe the dependence. For the amplitudes a fit with the function

$$A \left(1 - \frac{p^2}{p_c^2}\right) \quad (5.11)$$

works well as shown in the right side of fig. 5.15. We get $0.00603 \pm 1.35667E-4$ for A and 1364.56 ± 26.64 bar for p_c , for sample AFCL3 and $0.00603 \pm 1.35667E-4$ for A and 1324.84 ± 58.45 bar for sample Little Big sample.

5.4.4 Conclusions on the hysteresis in the glass transition range

A hysteresis at the glass transition is visible on both κ -Br and κ -Cl in the metallic state. We find that the relative amplitudes of the peak of the hysteresis for κ -Br is 2.5 times the value of κ -Cl, comparing average peak heights at ambient pressures each. We found that the change in amplitudes during annealing as seen in fig 5.4 change by 6 times as much in κ -Br as κ -Cl. We expected that the amplitudes of the peaks in κ -Cl to be smaller than in κ -Br from annealing but the peak heights are bigger than expected from annealing. We found from heat pulsing that the hysteresis may not be an effect of annealing or disordering, as the warming rate was too high for that. It is recommended to repeat the analysis of the hysteresis over pressure for κ -Br to see if it vanishes similarly to κ -Cl. Looking at the phase diagram in the upper right of fig. 2.6, which puts κ -Br at around 350 bar comparing to κ -Cl, we would expect the hysteresis to vanish 350 bar

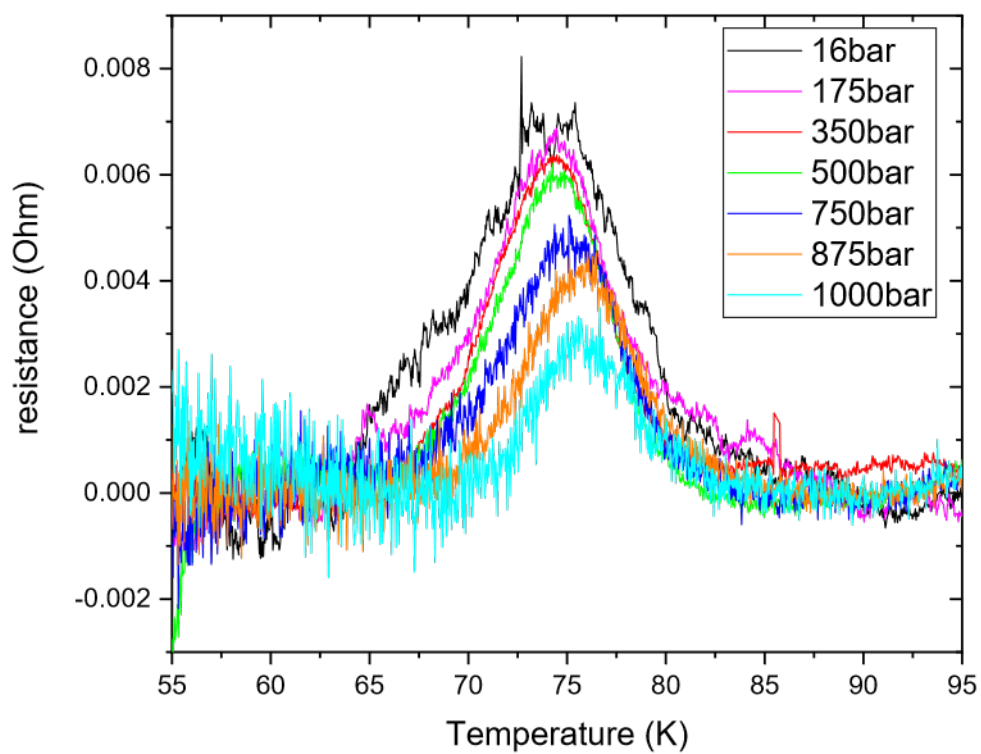
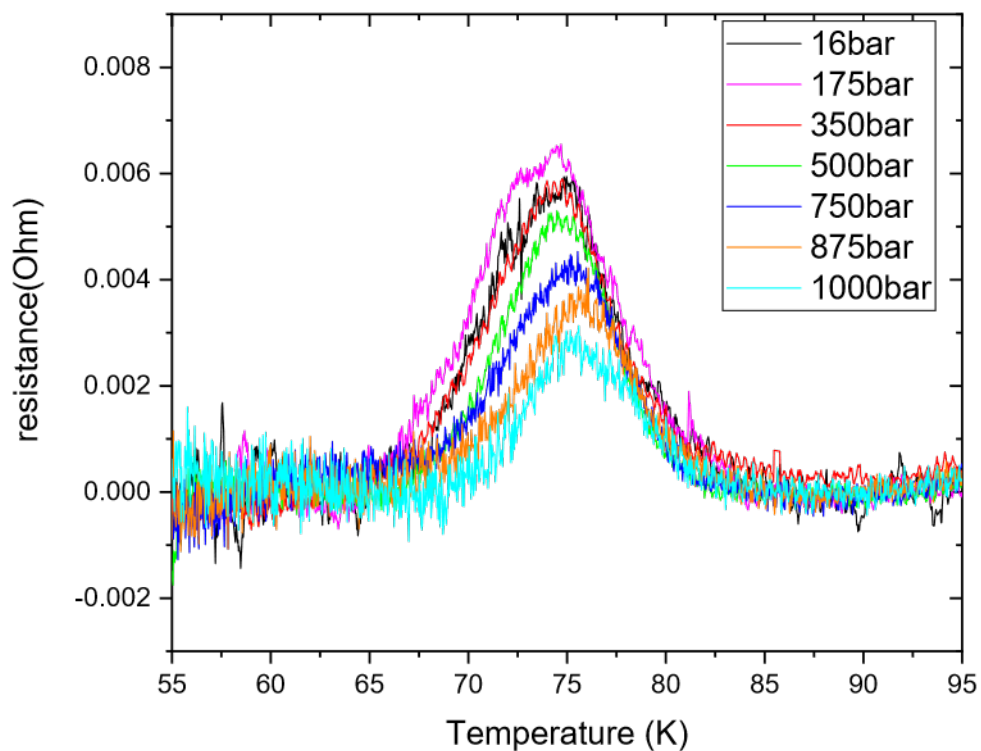


Figure 5.14 Normalized hysteresis. **Left:** For sample AFCL3. **Right:** For Little Big sample. We see a shift to higher temperatures and a decrease of the amplitude of the hysteresis with increasing pressure.

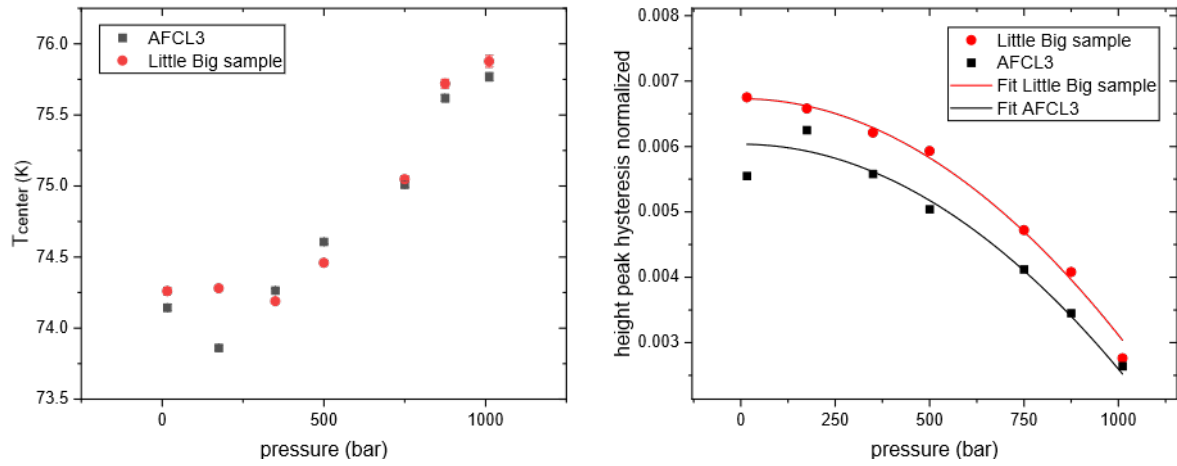


Figure 5.15 Left: Peak middle over pressure. **Right:** Normalized height of the hysteresis over pressure.

below the pressure where the hysteresis in κ -Cl vanishes. The nature and cause of the hysteresis is unknown to the author of this master-thesis.

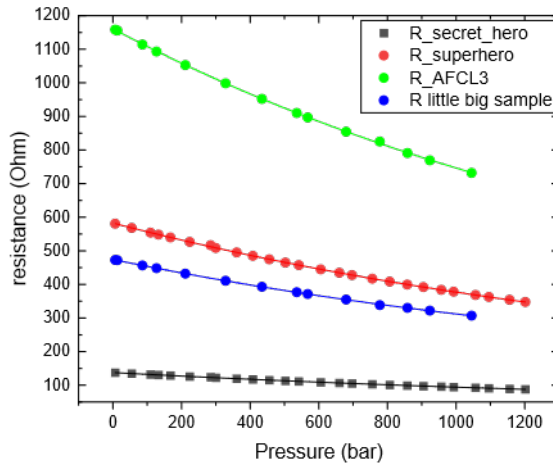


Figure 5.16 Resistance over pressure at room temperature. The samples shown are secret hero which is fully deuterated and super hero, little big sample and AFCL3. The lines between the points are fits with the fit function 'ExpDec1' from Origin.

5.5 κ -Cl under pressure

We want to investigate the effects of disorder of the ethylene endgroups in κ -Cl. Hartman et al. [8] claim that by disordering the ethylene endgroups in a partially deuterated κ -Br sample they can achieve a shift of the sample in the phase diagram that needs a pressure of 200 bar to compensate.

5.5.1 Resistance over pressure at room temperature

At first the pressure dependent resistance is checked at room temperature check the system shown in fig. 5.16. We fit the data with the fit function 'ExpDec1' from Origin

$$R(p) = a * \exp(p/t_1) + c \quad (5.12)$$

We get for t_1 , 2021 ± 71 1/bar for sample secret hero, 1814 ± 58 1/bar for sample super hero, 1784 ± 91 1/bar for sample AFCL3 and 1800 ± 90 1/bar for little big sample. The fully deuterated sample secret hero shows a slightly different rate t_1 than the other samples which show the same rate within error bars. The cooling with sample secret hero and super hero was a test cooling to set up the system. In the following, only samples Little Big sample and AFCL3 are discussed.

5.5.2 Resistance over pressure near the superconducting transition

We want to find the difference between the quenched state and the annealed state in terms of behaviour under pressure with respect to resistance. The samples were cooled in the pressure cell and temperature sweeps were performed at different pressures as seen in fig. 5.17 and fig. 5.19. On Little Big sample the problems with measuring resistance described in subsection 4.1.3 are visible for higher resistances in fig. 5.17. Comparing quenched to annealed state, we see on both samples a shift of the step features in the resistance, where the step features are indicated by arrows. This means that the step in resistance at the transition from insulator to metal moved. To easier identify the steps in the resistance, the curves in fig. 5.17 and fig. 5.19 are shown in 2D plots in fig. 5.18 and fig. 5.20. We see hysteresises in the resistance above the superconducting transition or above 10 K where superconductivity is already suppressed. These hysteresises are in the region of inhomogeneous phase coexistence reported by Lefebvre et al. [20], where the region is shown as shaded area in the lower left of fig. 2.6. These hysteresises too move to higher pressures with increasing disorder.

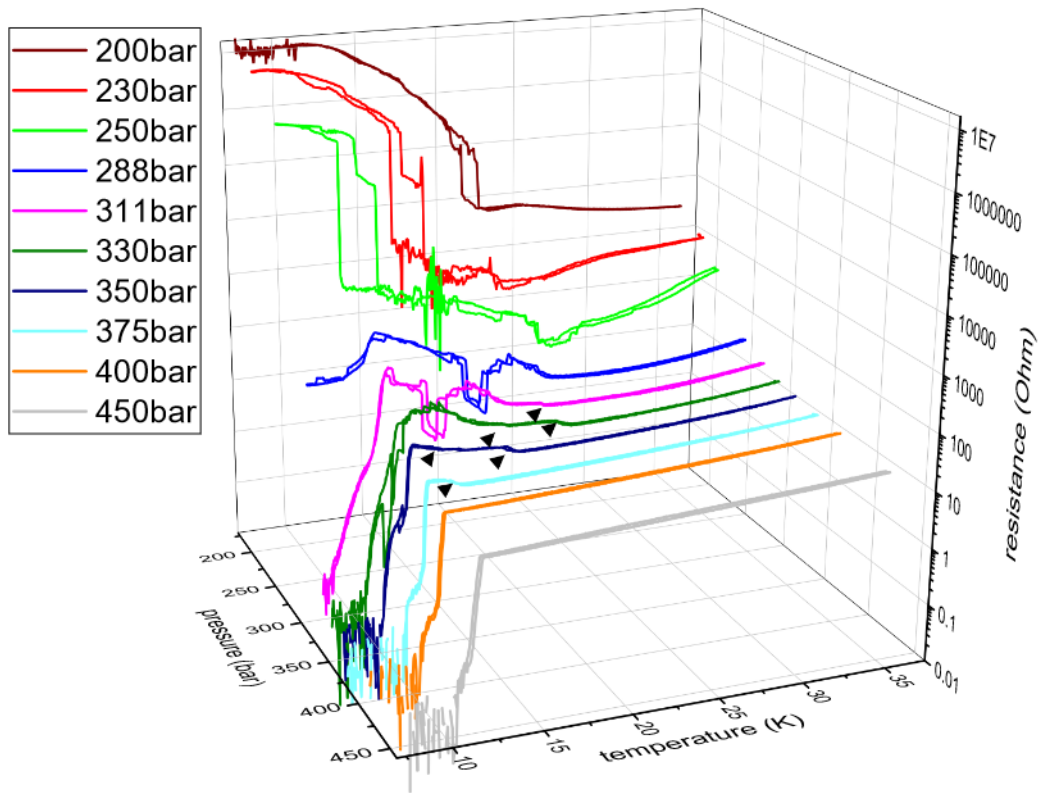
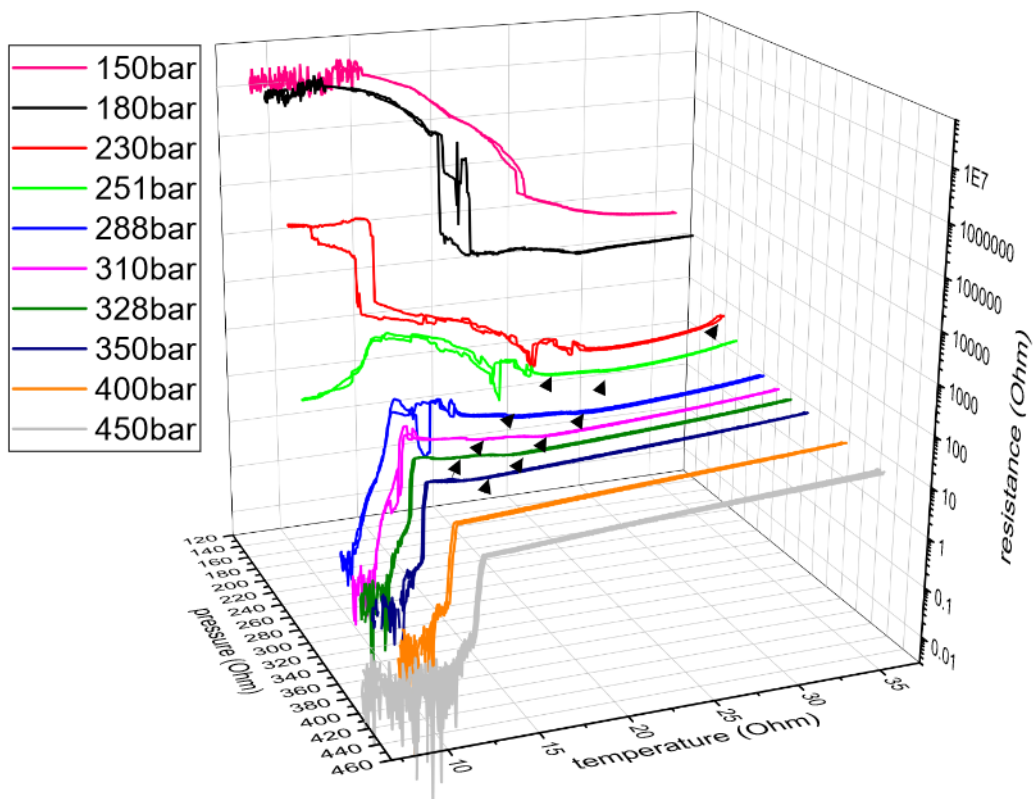


Figure 5.17 Resistance over pressure and temperature for Little big sample. The pressures in the legend are the pressures at 35 K. **Top:** annealed at 63 K for 50 h. **Bottom:** quenched. The arrows in both case indicate steps in the resistance.

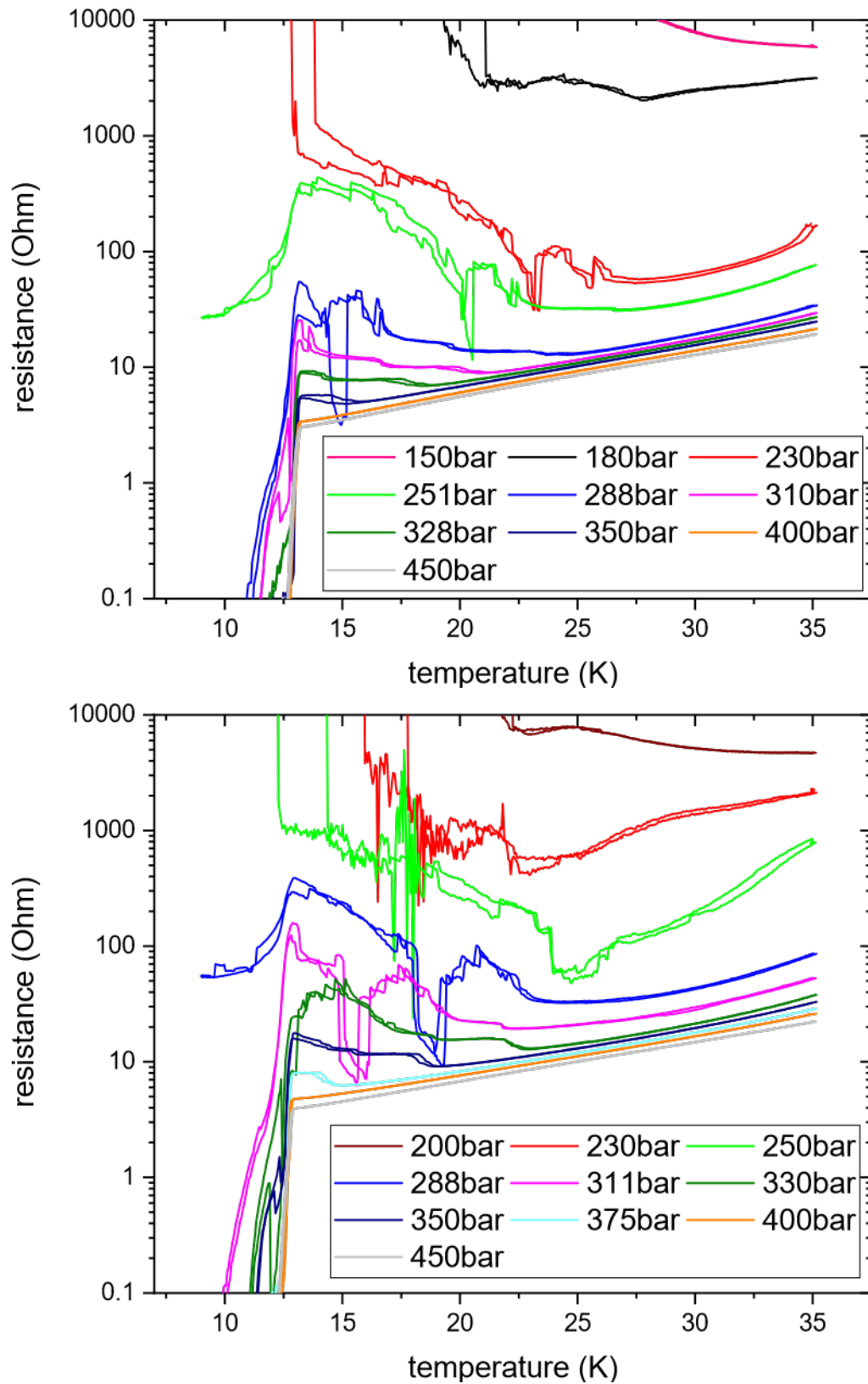


Figure 5.18 Resistance over temperature for Little big sample. The pressures in the legend are the pressures at 35 K. **Upper:** annealed at 63 K **Lower:** the quenched state. Colouring for each pressure is the same as in fig. 5.17.

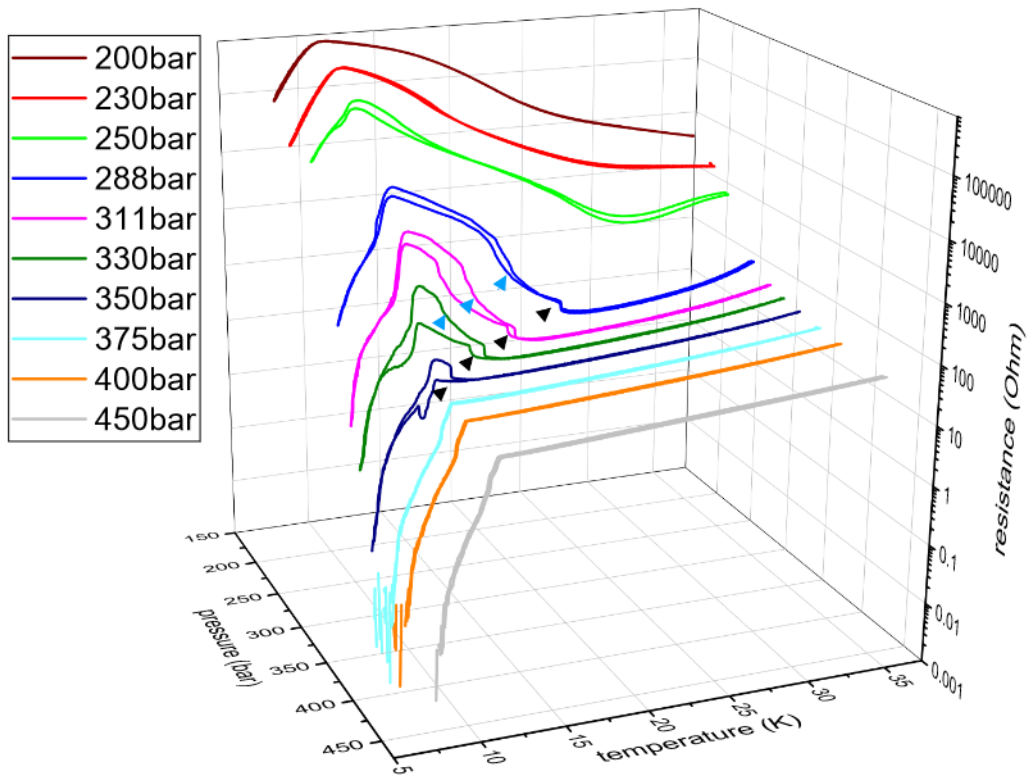
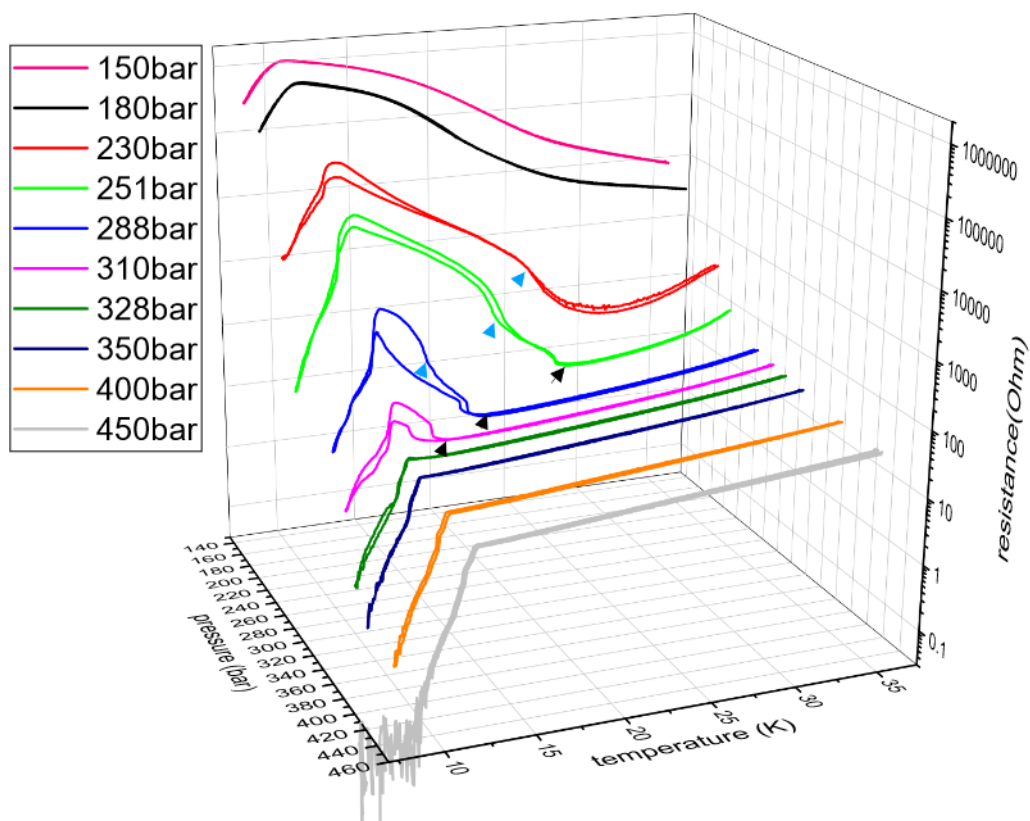


Figure 5.19 Resistance over pressure and temperature for sample AFCL3. The pressures in the legend are the pressures at 35 K. **Top:** annealed at 63 K for 50 h. **Bottom:** quenched. The arrows in both case indicate steps in the resistance.

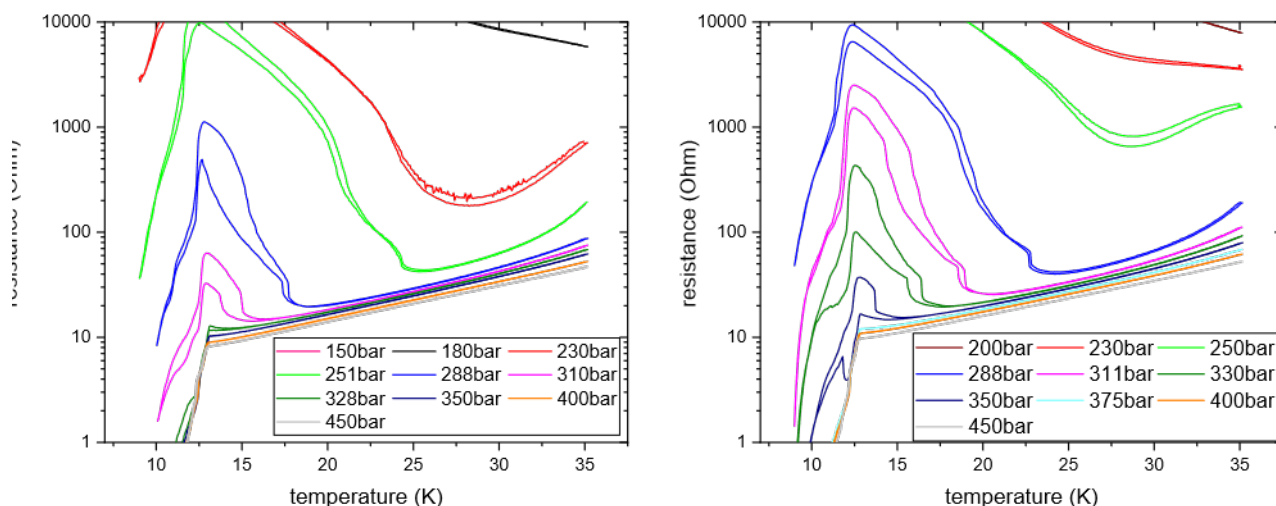


Figure 5.20 Resistance over temperature for sample AFCL3. The pressures in the legend are the pressures at 35 K. **Left:** annealed at 63 K **Right:** the quenched state. Colouring for each pressure is the same as in fig. 5.19.

We also have data on the pressure sweeps for the state where the sample was annealed at 64.5 K for 24 hours. This data is presented in the same way as in figures 5.17, 5.18, 5.19 and 5.20 in the appendix in section A.4. We see in fig. A.6 indicated by blue arrows what might be steps in the resistance. This then would imply that the lower pressure step feature of the two step features in resistance, we expect from the upper right of fig. 2.6 is just very small and broad. We see what might be this second step feature also for the pressures 230 bar, 251 bar and 288 bar for the state annealed at 63 K. Differences for both annealed states can be seen in the position of the step features and positions of the begin of the hysteresises. However these changes are rather small. We only see one step feature in resistance in sample AFCL3 clearly while we see two step features in resistance for Little Big sample. This might be from AFCL3 also showing a superconducting transition at ambient pressure which does not occur for other samples. Showing superconductivity is an indication of incomplete transition to a Mott insulator, which can be due to defects that act as dopants increasing or decreasing band filling, moving away from half filling. A filling away from half filling means that always two sites in the Hubbard model are unoccupied or completely occupied, leading to a remainder of hole- or electron conductivity. These defects then might also collapse or broaden out the lower pressure step feature in the resistance.

These features give three ways to try to find the shift in pressure due to disorder. Our primary target was to observe the shift in the hysteresises, but as we found the step features we can also evaluate these. However looking at the upper right of the phase diagram fig. 2.6 our temperature sweeps will be for some pressures almost tangential to the step feature observed there. Also looking at the lower right of the phase diagram in fig. 2.6, the step features are expected to lie along the direction of the temperature sweeps for some of the pressures as we can not compensate for pressure changes due to cooling and heating. To really analyse the step features one needs as pressure sweeps as shown in blue in the upper right of the phase diagram fig. 2.6. However pressure sweeps are not possible with our setup.

5.5.3 Shift in the step in resistance

We can read the step features from fig. 5.18, 5.20, A.7 and A.5. The results are shown in fig. 5.21

We see that except for the upper feature for the state annealed at 64.5 K for Little Big sample, lower and upper step feature coincide for the two annealed states. We see that the quenched state is shifted by around 20 to 30 bar to higher pressure for both samples. Further we see that the step features occur at a 30 to 40 bar higher pressure for Little Big sample compared to AFCL3. This coincides with AFCL3 showing an incomplete superconducting transition even at ambient pressure, where the superconducting transition is already completely suppressed in little big sample. Comparing the two step features found by

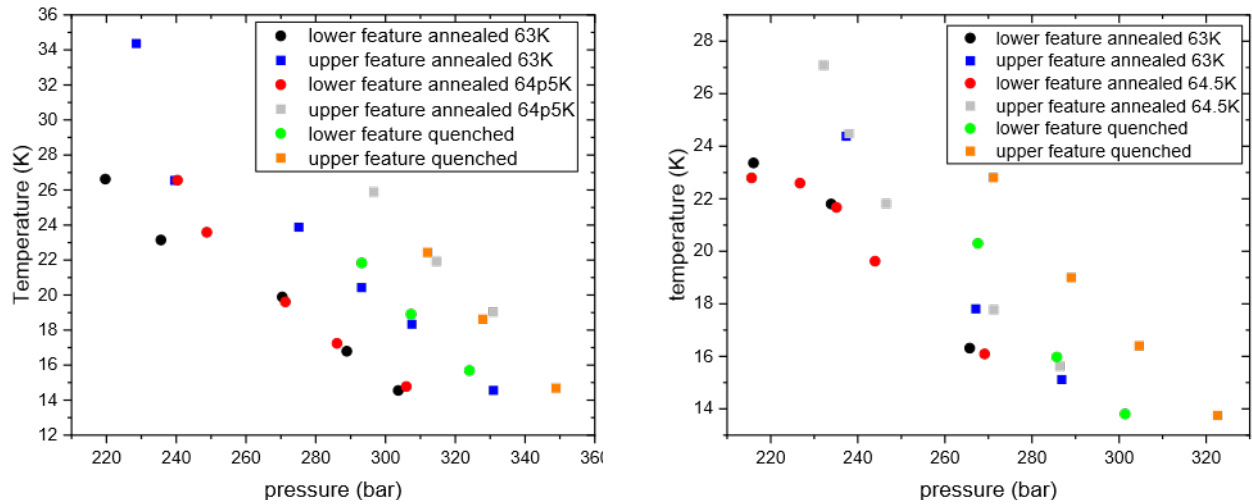


Figure 5.21 Position of step feature in resistance shown as temperature over pressure. Annealed and quenched state as described above. The lower step feature is marked with circles while the upper step features is marked in squares. **Left:** For Little Big sample. **Right:** For AFCL3.

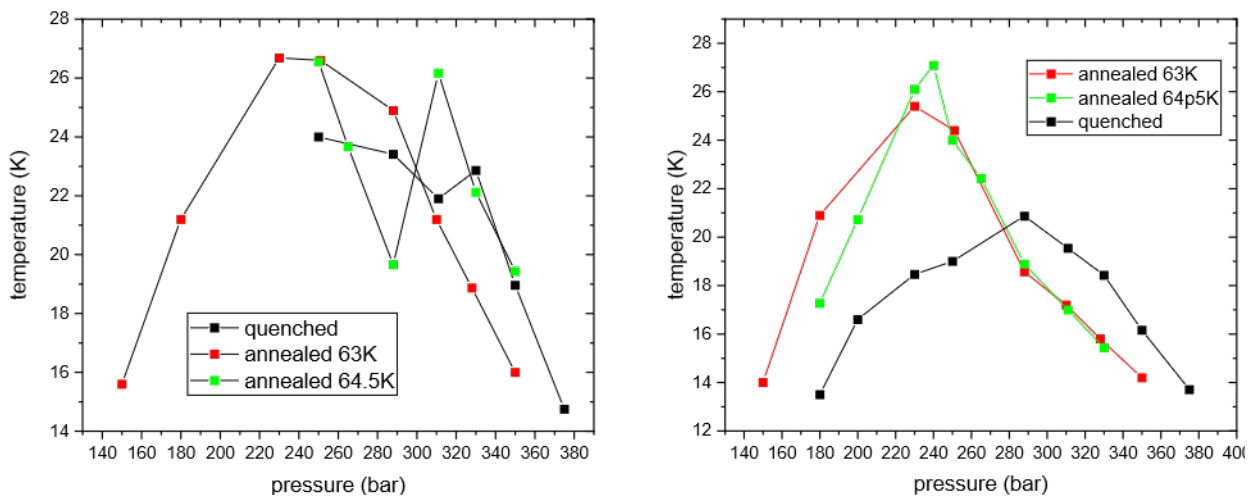


Figure 5.22 Position of the begin of the hysteresis in the resistance as temperature over pressure. Annealed and quenched state as described above. **Left:** For Little Big sample. **Right:** For AFCL3.

Fournier et al. [21] shown in fig. 2.6, where the two features extend from the boundaries of SC-I at 200 bar and 275 bar, our features are only separated by 30 bar. Further we see the step features to start at 14 K at pressures above 300 bar for Little Big sample and above 270 bar. Looking at the upper right of fig. 2.6 which is from Kagawa et al.[19] and figure 2(c) in their publication the double step feature starts at 280 bar at 14 K, which is similar to our step features. Further their double step features are also very close together as in our case. It maybe that the features found by Fournier et al. [21] are different features to the features found in resistance or that the distance in pressure between both features is strongly sample dependent.

5.5.4 Shift in the hysteresis above superconducting transition upon disordering

We now want to investigate the change of the beginning of the hysteresis depending on ordering and disordering of the ethylene endgroups, shown in fig. 5.22.

As with the upper step feature in resistance, the begin of the hysteresis in the resistance for Little big sample coincides for the state annealed at 64.5 K and the quenched state. For sample AFCL3 the begin of the hysteresis coincide for the annealed states. For Little Big sample it was no possible to determine the

For Little Big sample

state	A	$s_{slope}[1/\text{bar}]$	$p_{shift}[\text{bar}]$	c
annealed 63 K	-1.321 ± 0.071	0.0193 ± 0.0022	213.62 ± 4.22	0.458 ± 0.062
annealed 64.5 K	-1.584 ± 0.411	0.0163 ± 0.0036	202.67 ± 16.86	0.74 ± 0.39
quenched	-1.227 ± 0.054	0.0208 ± 0.0018	259.74 ± 2.87	0.41 ± 0.046

For AFCL3

state	A	$s_{slope}[1/\text{bar}]$	$p_{shift}[\text{bar}]$	c
annealed 63 K	-1.211 ± 0.061	0.0193 ± 0.0024	223.01 ± 3.90	0.110 ± 0.050
annealed 64.5 K	-1.159 ± 0.086	0.0213 ± 0.0026	224.33 ± 4.34	0.104 ± 0.076
quenched	-1.131 ± 0.054	0.0213 ± 0.0020	260.36 ± 3.13	0.117 ± 0.046

Table 5.1 Coefficients from the fits of the logarithm of the resistance over pressure with the formula from equation 5.13

sample	63 K and quenched	64.5 K and quenched	63 K and 64.5 K
Little Big sample	46.12 ± 5.10	57.07 ± 17.10	10.95 ± 17.38
AFCL3	37.35 ± 5.00	36.03 ± 5.35	1.32 ± 5.83

Table 5.2 Differences of the midpoints of the transition calculated from table 5.1

beginning of the hysteresis for the state annealed at 64.5 K and the quenched state for pressures below 250 bar due to the measurement problems described in subsection 4.1.3. We see a shift of the hysteresis by about 20 to 30 bar comparing the state annealed at 63 K and the quenched state.

5.5.5 Shift in the transition between metal and insulator close to the critical point upon disordering

The temperature of 35 K was used for evaluating the shift in the transition as there the double step is already mostly collapsed to a single step. This simplifies evaluation. Further it is the highest temperature up to which we did the temperature sweeps at different pressures. According to Kagawa et al. [19] the closer one gets to the the critical point at 38.1 K and 232 bar, the lower in the resistance change is at the step feature. To get a well identifiable step the highest measured temperature, 35 K, was chosen for the evaluation.

The curves for the two annealed states coincide for both samples. The logarithm of the resistances shown in fig.5.23, looks similar to a $\tanh()$ function close to the transition. We can use this to define the middle of the transition, by the pressure were the \tanh function has its zero transition. For this we fitting the logarithm of the resistance with

$$A * \tanh(s_{slope} * (p - p_{shift})) + c. \quad (5.13)$$

A is to account for the height of the step, s_{slope} for the broadness of the transition, p_{shift} is the pressure at which the $\tanh()$ function has its zero transition and c is to account for the normalization. We get the following results for the fit shown in table 5.1

The error bar for Little Big sample for the state annealed at 64.5K are relative large as a point at a lower pressure would be necessary to better determine when the transition starts. Taking the differences of the middles of the transition we get the differences shown in table 5.2.

We see that the difference is about 40 bar, where it is a big smaller for sample AFCL3 than for Little Big sample. The 40 bar difference is higher than from the estimates by the two step features and the hysteresises. However this way of estimating the shift in pressure due to disordering should be more

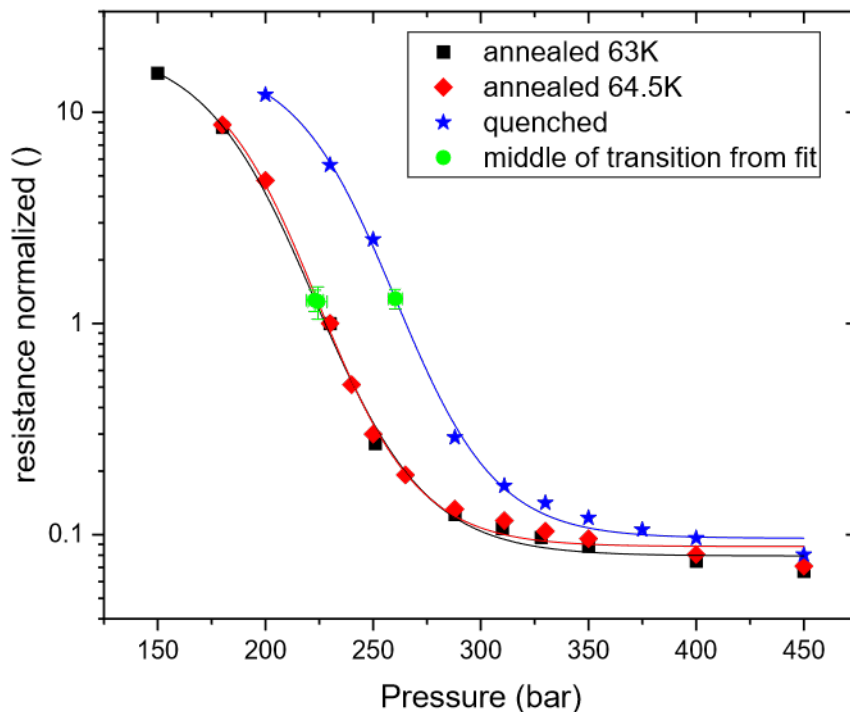
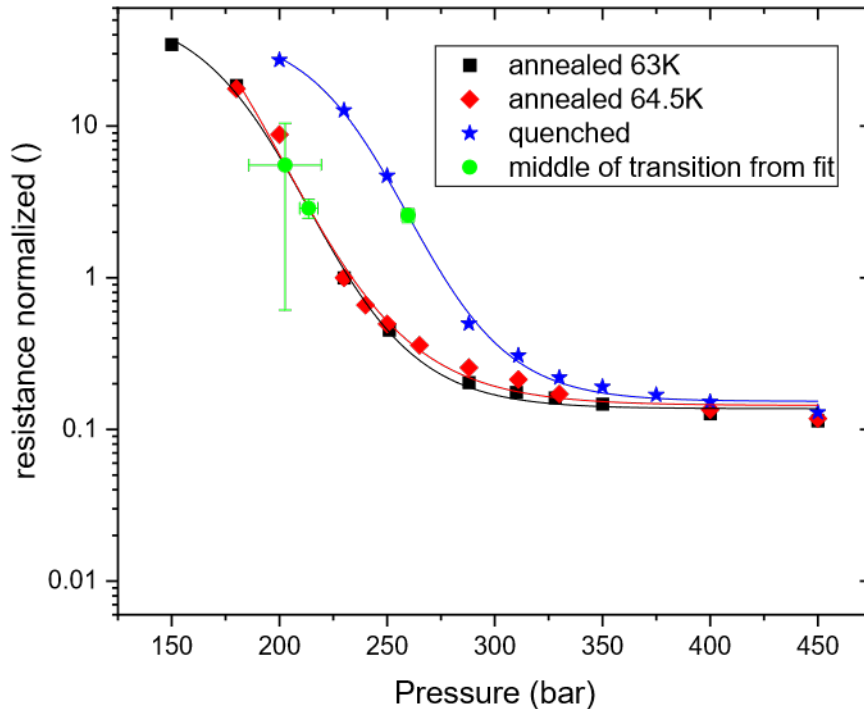


Figure 5.23 Normalized resistance at 35 K over pressure. For the annealed state the resistance was normalized to the value at 200 bar. For the quenched state the factor for normalization was chosen such that the value at 450 bar is very close to the values of the annealed states. The green circles including error Annealed and quenched state as described above. **Top:** For Little Big sample. **Bottom:** For AFCL3.

accurate than the other two, as it is done from points that are easier to read of than the begin of the step features or the hysteresises.

5.6 Hysteresis in the resistance above T_c

From section 5.5 we know that there is a hysteresis in the resistance above the superconducting transition when approaching the metal insulator transition for κ -Cl. The heat pulses are said to act like "negative pressure" and shift the sample in the phase diagram towards the metal insulator phase transition boundary or over it was demonstrated by Müller et al. [22]. Müller et al. used a sample that consisted of 80 % fully deuterated ET molecules and 20 % fully hydrogenated ET molecules. We now want to investigate how close we can get with fully hydrogenated samples to the metal insulator transition. We see that for the heat pulsed states we see hysteresis appearing above the superconducting transition. Each hysteresis was measured two times to ensure reproducibility, by cooling down below T_c then warming up above the end of the hysteresis and repeat by cooling below T_c and then warming up again. The results are shown in fig. 5.24.

We see that for all states quenched by heat pulse, the hysteresis starts at around 19 K or higher. For the heat pulsed states with a final temperature below 100 K, it is difficult to determine if the hysteresis seen in fig. 5.24 are due to the hysteresis in the resistance or due to a sweep induced hysteresis due to a mismatch between thermometer and sample temperature. However, the hystereses due to disordering by heat pulse in κ -Br are strongly different from the hystereses in κ -Cl. In κ -Cl the hystereses have a clear defined start which depends on pressure and are clearly visible as seen in section 5.5. For the quenched states of κ -Br, where the hysteresis is clearly visible, the hysteresis starts at about 20 K, independent from the amount of disorder. If we can map disorder to pressure, the starting points of the hystereses for κ -Br should be similar to the ones shown in fig. 5.22. However we see that the starting temperature of the hystereses is independent of disorder. This may imply that either the starting points in temperature for κ -Br behave very different from κ -Cl or we are not approaching the Mott metal-insulator transition but rather the Mott-Anderson metal-insulator transition. The Mott-Anderson metal-insulator transition might lead to different hystereses in its vicinity, where dependence is rather on disorder than on pressure. This would then be an argument against a similarity between pressure and disorder.

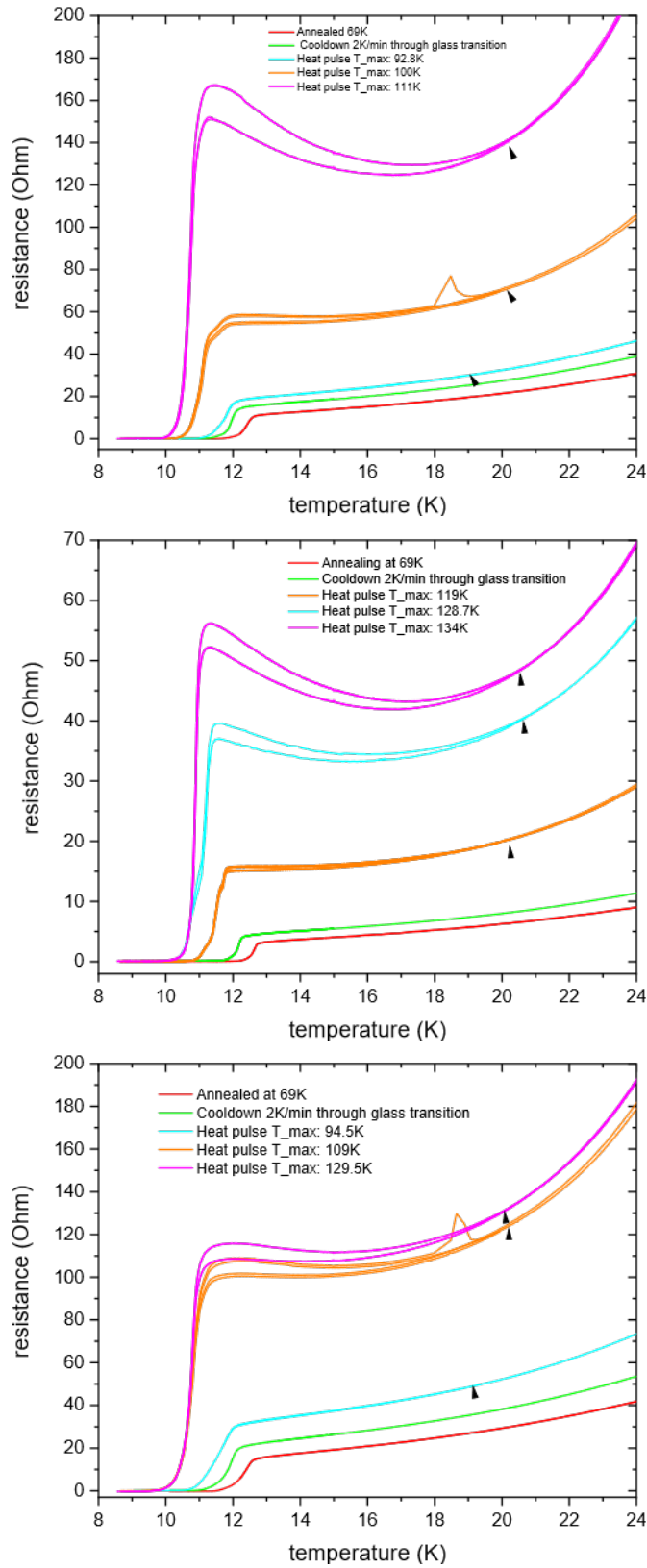


Figure 5.24 Resistance over temperature for samples **Top:** Nizza, **Middle:** Crumb and **Bottom:** NKG11. For all samples arrows indicate the beginning of the hysteresis. In the orange cooling curves at the first warming the sample were heated above 25 K by accidentally opening a valve that separated sample space and helium recovery line. This can be seen as a sharp upturn and hysteresis above 18 K till 19 K.

5.7 T_c dependence on thermal treatment

Looking at fig. 5.24 we can see that the critical temperature of superconductivity T_c and the broadness of the superconducting transition depends on the ordering of the ethylene endgroups.

5.7.1 T_c value

We find the following values of T_c, by using the mid point rule that defines T_c as the temperature where in the superconducting transition, the resistance is half that of the resistance at the superconducting entrance. The result is shown in fig. 5.25.

We see that the T_c is the highest the better the ethylene endgroups were annealed. The theory for this is put together by Powell and McKenzie [42]. They state the result from Anderson [43] that for s-wave pairing impurities that are nonmagnetic do not change T_c. Anderson states that as Cooper pairs are formed from time reversed states but nonmagnetic impurities do not break time reversal symmetry. Powell and McKenzie further state the result by Abrikosov and Gorkov [44] that magnetic impurities do change T_c and give the formula

$$\ln\left(\frac{T_{c,0}}{T_c}\right) = \Psi\left(\frac{1}{2} + \frac{\hbar}{4\pi k_B T_c \tau_M}\right) - \Psi\left(\frac{1}{2}\right), \quad (5.14)$$

where T_{c,0} is the critical temperature for the system without impurities and Ψ the digamma function and τ_M is the quasi particle life-time due to scattering at magnetic impurities. They further state the formula for nonmagnetic impurities for non s-wave coupling which is eqn. 5.14 with the $\frac{1}{\tau_M}$ replaced by $\frac{1}{\tau_N}$ assuming isotropic scattering. τ_N is the quasi particle life time due to scattering at nonmagnetic defects. Powell and McKenzie state that Hasegawa and Fukuyama [45] found another way how in s-wave paired superconductors T_c is reduced, but argue against it.

Powell and McKenzie then do an approximation of equation 5.14 for a low number of impurities $\hbar/\tau \lll k_B T_c$ by using

$$\Psi\left(\frac{1}{2} + x\right) = \Psi\left(\frac{1}{2}\right) + \frac{\pi^2 x}{2} + O(x^2), \quad (5.15)$$

getting

$$T_{c,0} - T_c \approx \frac{\pi \hbar}{8 k_B \tau} \quad (5.16)$$

for both types of impurities. The impurities we get by disordering the ethylene endgroups are nonmagnetic but looking at the phase diagram 2.6, we are close to the antiferromagnetic transition which we might even reach using heat pulses. As Powell and McKenzie state, Zn substitution for Cu in the cuprate superconductor YBCO can form local magnetic moments, also our defects introduced by disordering of the ethylene endgroups may also form magnetic moments. As we can see in figure 5.25 this disorder changes T_c. Powell and McKenzie state, that either the disorder by disordering the ethylene endgroups forms magnetic moments, which would allow for s-wave pairing or if the pairing of superconductivity is non s-wave then the defects may be non magnetic. Powell and McKenzie give the formula for the residual resistivity by,

$$\rho_0 = \frac{\pi \hbar^4}{2e^2 m^* c t_{\perp}^2} \frac{1}{\tau_t} \quad (5.17)$$

where τ_t is defined by

$$\frac{1}{\tau_t} = \frac{1}{\tau_s} + \frac{1}{\tau_c} \quad (5.18)$$

with τ_s the quasi-particle life time due to structural disorder and τ_c the life time due to defects depending on the cooling rate. Further c is the inter-layer spacing, m* the effective mass of the quasi-particles and t_⊥ the inter-layer hopping integral. With this they formulate using equation 5.16 the simplified equation for the dependence of T_c by

$$T_c \approx T_{c,0} - \frac{e^2 m^* c t_{\perp}^2}{4 k_B \hbar^3} \rho_0. \quad (5.19)$$

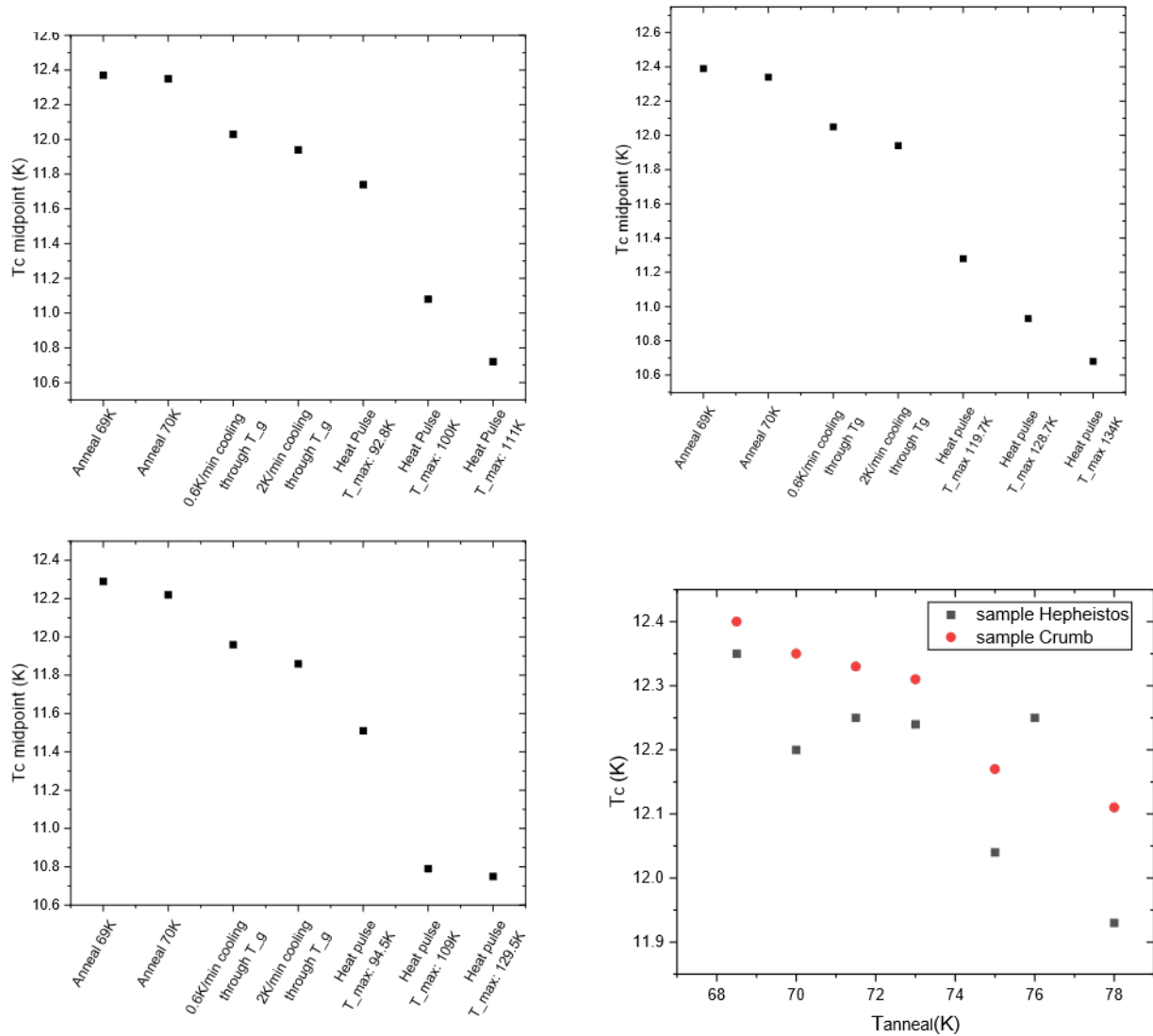


Figure 5.25 Midpoint of T_c for **Top left:** Nizza, **Top right:** Crumb and **Bottom left:** NKG11. The results are shown for the full range of states available by preparing by thermal treatment. This data was acquired with the optimization of temperature stabilization described in subsection 4.3.2. **Bottom right:** The midpoints of T_c found after annealing. As can be seen from fig. 5.3, the thermal stabilization and equilibration to the thermometer for sample Hepheistos are much worse than for sample Crumb, resulting in a T_c measurement with big variation. This is as this measurement was done before the improvements in thermalization described in subsection 4.3.2.

sample	A[K/(Ohm cm)]	$T_{c,0}$ [K]
Nizza	1.0343±0.0917	12.8118 ± 0.0591
NKG11	0.8951±0.0879	12.6812 ± 0.0612
Crumb (all)	0.3129±0.0298	12.4841 ± 0.0612
Crumb (part)	1.7579±0.1182	12.9086 ± 0.0377

Table 5.3 Results from fitting the T_c midpoints for the residual resistivity below 1 Ohm cm with equation 5.19. The data of sample Crumb was fitted twice once with all data including the results from the annealing studies and once only with the part of the data from the top right of fig. 5.25.

We now plot the T_c we found over the residual resistivity shown in fig. 5.26. For all states except the heat pulsed states we see the linear behaviour predicted. We can fit the linear parts with equation 5.19 and for simplicity name $A = \frac{e^2 m^* c t_1^2}{4k_B \hbar^3}$. We get We see that for samples Nizza and NKG11 the result for the slope A is in good agreement with Powell and McKenzie [42] who state a result for A of 0.9 K/(Ohm cm). However they state that $T_{c,0}$ is 11.7 K which might mean that our thermometry is still not correct even with our improvements as described in subsection 4.3.2. A $T_{c,0}$ of 11.7 K was also reported by Stalcup et al.[10]. The values we find for sample Crumb is not in good agreement with the other samples and Powell and McKenzie. This may be as the resistance at superconductivity entrance is already low making it difficult to fit the residual resistance with high enough accuracy.

The linear behaviour does not hold anymore for the heat pulsed states, where the reduction in T_c is slower than expected from equation 5.19. This might mean that the linear approximation of the digamma function is no longer valid as we have to many impurities. Otherwise as we may approach the antiferromagnet-superconductor-coexistence range by the heat pulses, this may imply that the scattering by the frozen in defects from the ethylene endgroups has much more complicated dependence on the residual resistivity as we may now not only have either scattering from nonmagnetic and magnetic impurities but scattering from both. This is somewhat surprising as the increase in scattering should intuitively increase the reduction of T_c . Otherwise we might just reach a saturation of the decrease of T_c from scattering which might occur in a superconductor with a combined s- and non s-wave pairing. However Powell and McKenzie argue against that with details found there.

[42]

We rewrite equation 5.14 to

$$T_c = T_{c,0} * \exp \left(-\Psi \left(\frac{1}{2} + \frac{\hbar}{4\pi k_B T_c \tau_M} \right) + \Psi \left(\frac{1}{2} \right) \right). \quad (5.20)$$

With the values of A from the linear fit we can solve equation 5.20 numerically and plot the result in fig. 5.27 for A=0.9 K/(Ohm cm) and $T_{c,0} = 12.7$ K. Also for A=1.5 K/(Ohm cm) and A=0.5 K/(Ohm cm) the result is shown. We get an even sharper decrease of T_c from A=1.5 K/(Ohm cm) we get an even sharper decrease of T_c and hitting 0 at 9.8 K while for A=0.5 K/(Ohm cm) the resulting T_c is quasi linear over the entire range. This means that changing A away from 0.9 K/(Ohm cm), would not change equation 5.20 in such a way that we would see the change in T_c we observe. Rather A is only scaling the residual resistivity. We see that A=0.9 K/(Ohm cm) and $T_{c,0} = 12.7$ K fit our results nicely except for the heat pulsed states.

It may be that our residual resistivity is increase by the fact that we approach a metal-insulator-transition and therefore the residual resistivity is increased not only by the increase in scattering, as also Taylor et al. [46] argue. This may mean that the true residual resistivity from scattering is much lower and the T_c points from heat pulsing might be nicely the values we expect from theory when plotted over the residual resistance from scattering only. Looking at the occupation probabilities of eclipsed conformation, which is the ground state shown in figure 2.2, we see that for temperatures below 130 K the ethylene endgroups are mostly in the ground state, therefore we can, as we did in section 3.1, treat the staggered conformation as defects in a crystal lattice were all ethylene endgroups are in the eclipsed ground state. The defect density is then the density of the ethylene endgroups minus the density of the ethylene endgroups in the eclipsed state. Hartman et al. reports that for a cooling rate of $q = 0.01$ K/min, 97.8% of the ethylene endgroups

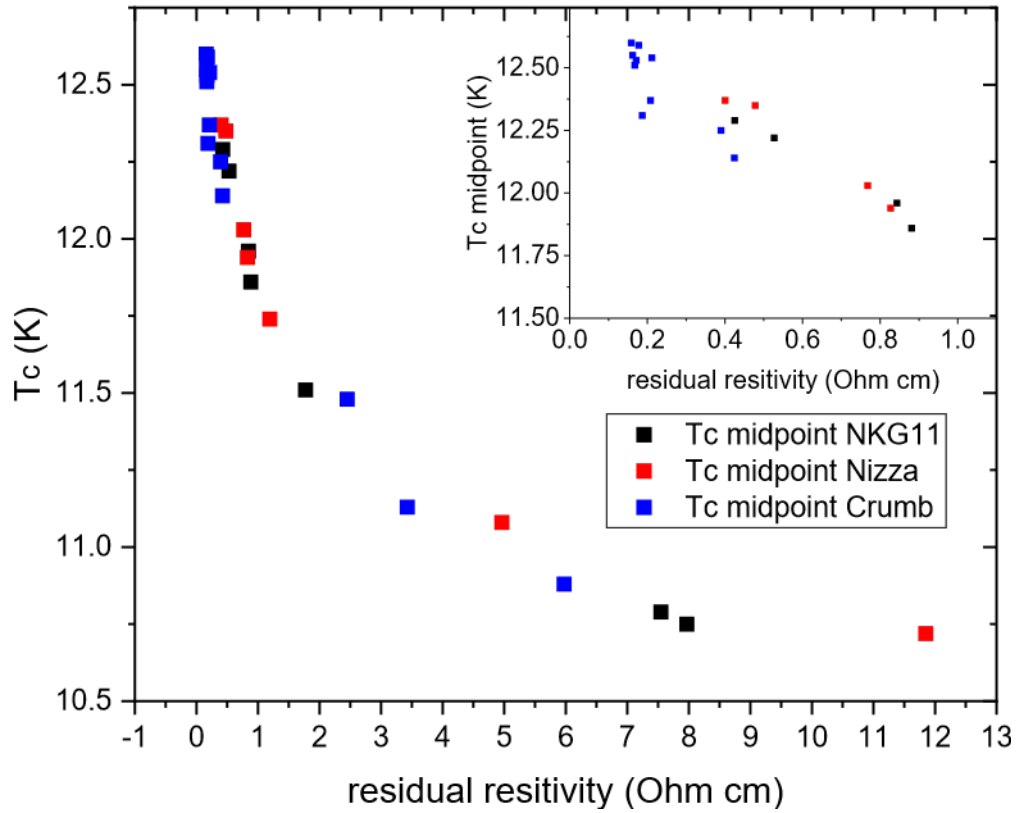


Figure 5.26 T_c midpoints over the residual resistivity. The insert shows all states except the heat pulsed states.

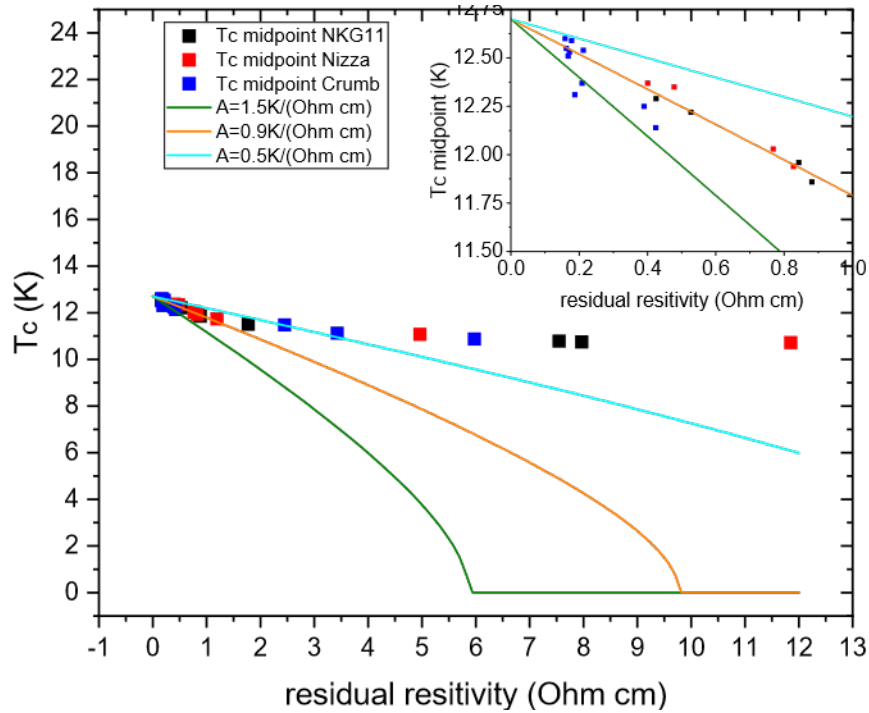


Figure 5.27 T_c midpoints over the residual resistivity. The insert shows all states except the heat pulsed states. Also shown the results of the solution for the digamma function.

are in the ground state, 96.8 % for a cooling rate of 2 K/min and 94 % for their heat pulsed state. This would give an increase in the defect density from 2.2 % to 6 %. Our heat pulses might have led to more disorder but may not have been able to get more than the 15 % disorder from reaching 130 K, as shown in figure 2.2 and completely freezing the disorder in. Even in this case, we would at maximum get an increase of the defect density by a factor of 6.8, from least to highest ordered. This is much less than the factor of 20 to 30 in the change in residual resistance we see. If the scattering cross section does not change significantly with disorder, we could then estimate that the highest residual resistance only from increase of defect density would be no more than 2 to 3 Ohm cm. This then would bring all T_c values found, back to the line from Abrikosov-Gorkov theory. Erkenov [47] found that the change in the Dingle temperature is about a factor of 4 to 5 for the states shown here. Looking at the definition of T_D in equation 3.21, we see that it is proportional to one over the particle relaxation time and therefore directly proportional to the scattering rate. This agrees with our estimate for the change in defect density.

5.7.2 Change in Broadness of transition

We see, looking at fig. 5.24 that the broadness of the resistance changes depending on the thermal treatment. To better understand this and to rule out effects of changing residual resistance the figure is repeated here as fig. 5.28, with all resistances normalized to 1 at 14 K. As in fig. 5.24 the cooling with 0.6 K/min through T_g and the annealing at 70 K over night are not shown as they are very close to the cooling with 2 K/min and the annealing at 69 K and would make the graph much harder to read. We can see that the broadness of resistance increases with increasing disorder and sometimes we see some step like features in the heat pulsed states which were not done till the highest temperature, like for example the orange curve for sample Nizza or the orange and magenta curve for sample Crumb. The reason for this feature is unknown, it may be due to some inhomogeneity in either the sample or the heat pulsing and cooling after the heat pulse. We can read the broadness of the superconducting transition, where we set the broadness by the temperature difference between the temperature where the resistance is 5 % and 95 % of the resistance at the entrance of superconductivity. The result is shown in fig 5.29

It is noteworthy that only the layers of the organic molecules ET become superconducting but not the anion $\text{Cu}[\text{N}(\text{CN})_2]\text{Br}$. We are measuring the resistivity orthogonal to the organic layers and therefore we see the superconducting transition by the onset of Josephson hopping across the anion. Effectively the organic layers form together with the anions Josephson junctions. We see for all states that the broadness first increases with increasing disorder. However for the strongest heat pulsed states the broadness decreases again, where the broadness of the superconducting transition decreases even below that of the annealed state. This would imply that the disorder after some point enhances the onset of Josephson hopping.

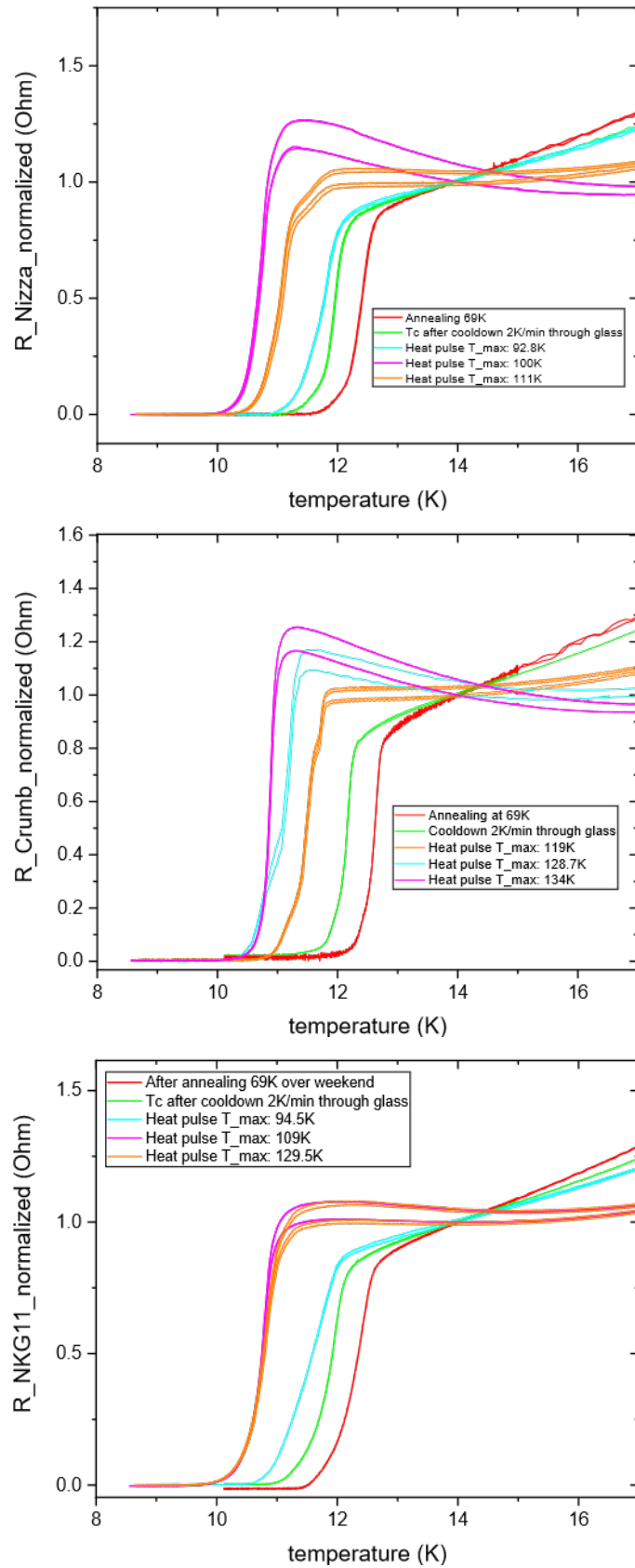


Figure 5.28 Resistance over temperature for samples, where the resistance is normalized to its value at 14 K. **Top:** Nizza, **Middle:** Crumb and **Bottom:** NKG11

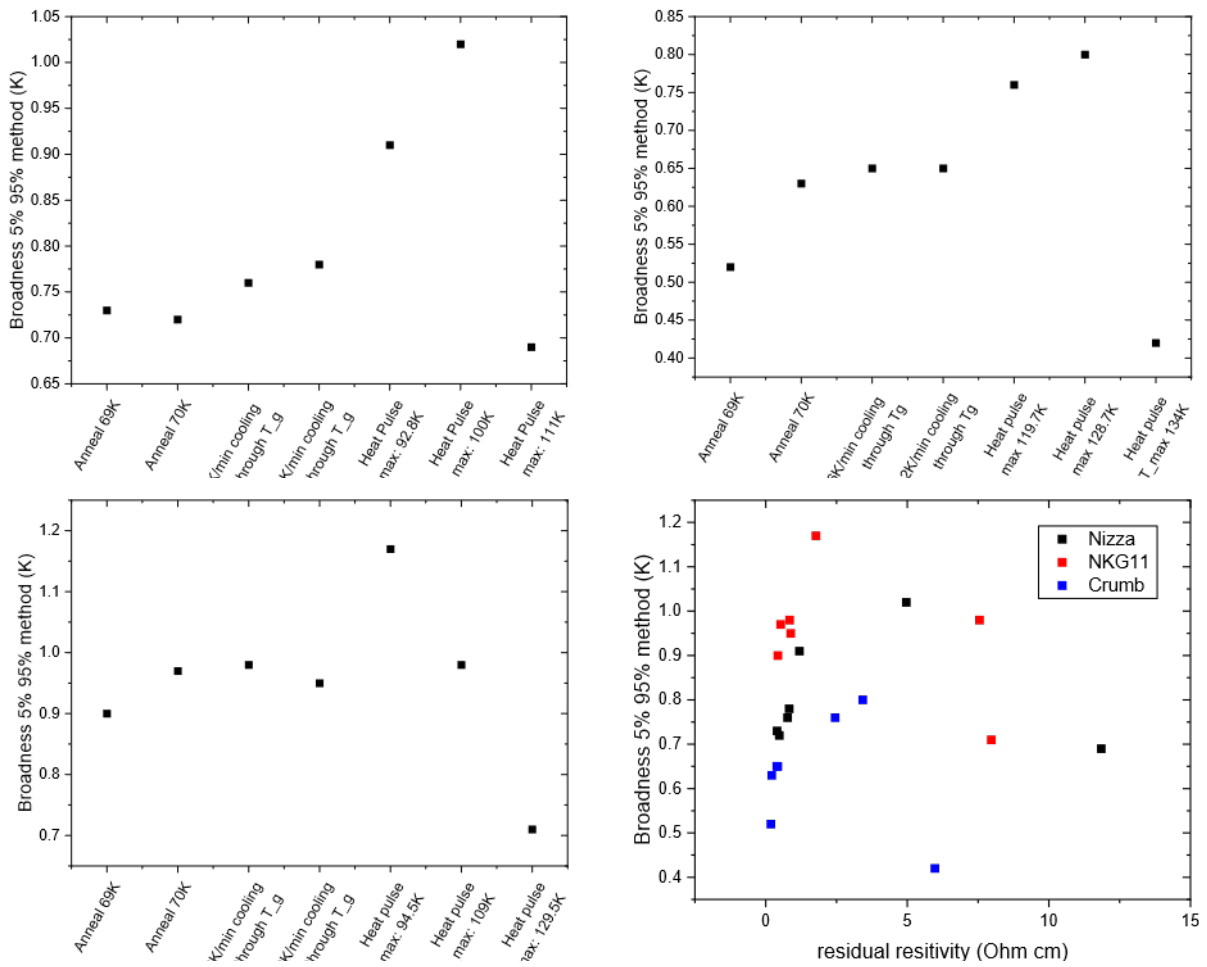


Figure 5.29 Broadness of the superconducting transition for **Upper left:** sample Nizza, **Upper right:** sample Crumb and **Lower left:** sample NKG11. **Lower right:** Broadness of the superconducting transition for all three samples over the residual resistivity.

5.8 Oscillations in magneto resistance

5.8.1 Critical field of superconductivity

When measuring the oscillations in magnetoresistance for a superconductor, the first thing observed is the breaking of superconductivity by the magnetic field. As we have seen that the critical temperature of superconductivity decreases upon increasing disordering of the ethylene endgroups, we would also expect that the critical field changes. We therefore evaluated the critical field by the definition that the critical field is the field where the resistance has reached 50% of the resistance just above superconductivity. The results are shown in Fig. 5.30.

We can see that the critical field increases with disorder for samples Nizza and NKG 11. For sample Crumb the behaviour is different. For this sample one has to take into account that due to the low resistance of sample Crumb, the signal to noise ratio for the annealed and normally cooled state is very bad and determining the critical magnetic field is difficult and not precise enough. Therefore only the partially and strongly quenched states can be evaluated accurately enough. They show that the critical magnetic field increases with disorder also for this sample.

This is at first against the intuition as disorder decreases the critical temperature and therefore is detrimental for the superconducting phase. However an explanation for this behaviour can be that the defects caused by the disordering form attractive potentials for the magnetic flux lines formed in the Shubnikov phase of the type II superconductor as shown in [48]. These defects are then called pinning centers as they "pin" the flux lines. The flux lines are prevented from rearranging upon increasing and decreasing the magnetic field. Once the magnetic flux lines start to move through the superconductor they locally heat the superconductor, as the centers of the flux lines are normal conducting and moving them means a normal conducting current. The critical field is then reached when the force driving the flux lines overcomes the attractive potential of the pinning center. However Yoneyama et al [49] report that the critical current density decreases with increasing disorder and conclude from that that the pinning forces of the magnetic flux vortices decrease with disorder.

Sasaki et al. [18] report that there is a phase separation upon advancing to and crossing the phase transition from metal to insulator, by increasing deuteration of the ET molecules. The remainder of the metallic phase becomes superconducting producing many thin sheets of superconductivity which then have an increased critical field. However even for the comparison of normal cooled and annealed state we get a change in critical field, where we are far from the transition. This would then be in favour of the explanation with increasing flux pinning.

5.8.2 Change in frequency

We want to have a look at the frequencies of the Shubnikov-de-Haas oscillations found by Fourier transform. We will focus on the first order frequencies as higher order oscillation frequencies are just integer multiples of the first order frequency. We see only the oscillations of the β -orbit of the Fermi surface at around 3850 Tesla, as according to Weiß [9] the oscillations of the α -orbit at 530 ± 15 T are almost invisible even in the best samples for the magnetic field orthogonal to the conductive layers. The results are shown in fig. 5.31. We see that the frequencies on the in the up sweep of the magnetic field, marked in red, are higher than the frequencies on the down sweep of the magnetic field, marked in black. We see that the frequencies of sample Crumb are about 30 T higher than of samples Nizza and NKG11. Guterding et al. [14] report that the band structure changes when changing the conformation of the ethylene endgroups. This might then change the area of the Fermi surface, however the change may be small. We do not see a difference in the frequency for the different states. This implies that the area of the Fermi surface of the β orbit did not change.

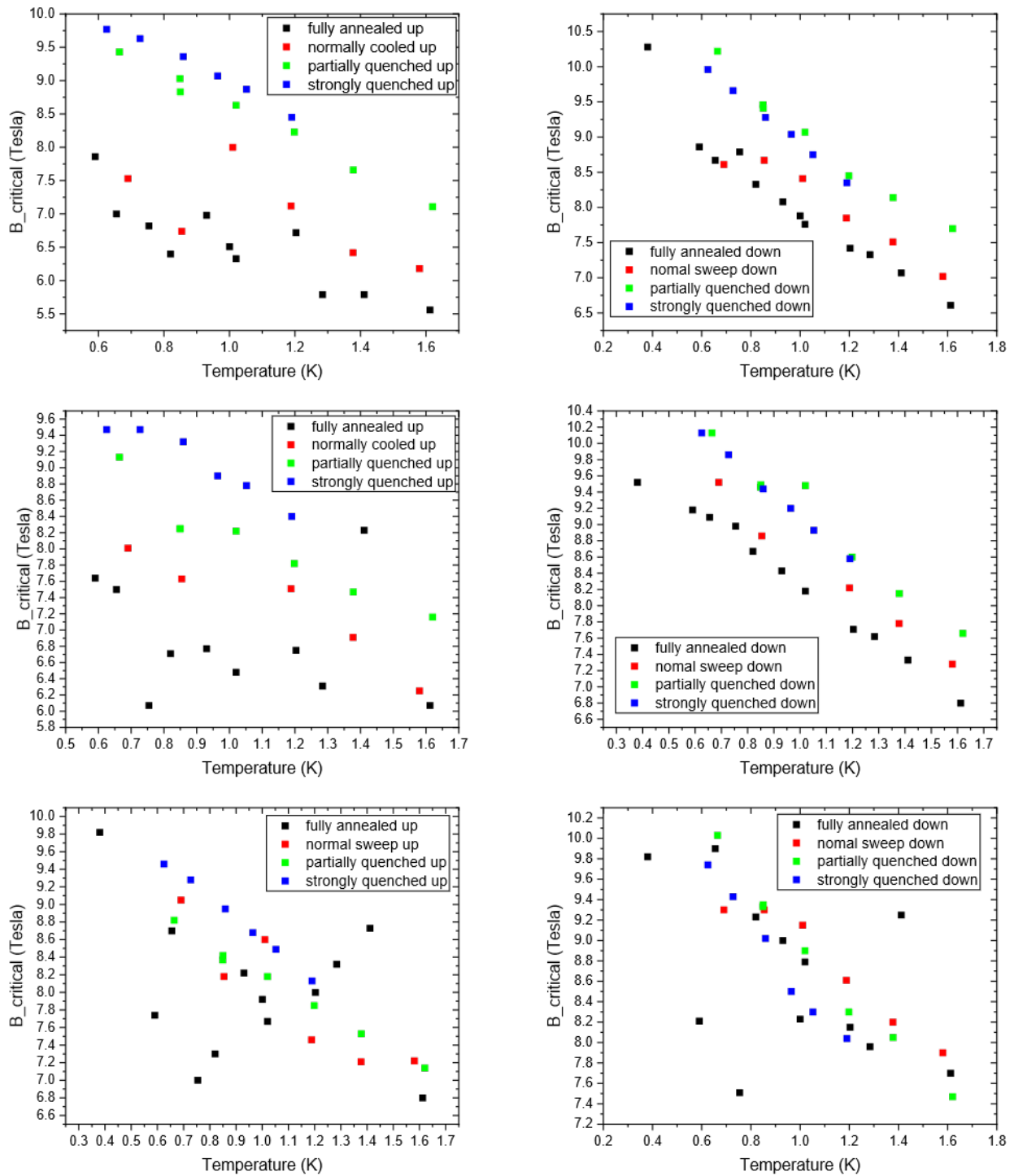


Figure 5.30 Critical magnetical field. Where there was data available from the characterisation measurements done in Garching the field was added for comparison. The rest is from the pulsed magnetic field experiments done in Dresden. **Left column** up sweeps **Right column** down sweeps **Upper row** sample Nizza κ -Br, **Middle row** for sample NKG 11 **Lower row** for sample Crumb

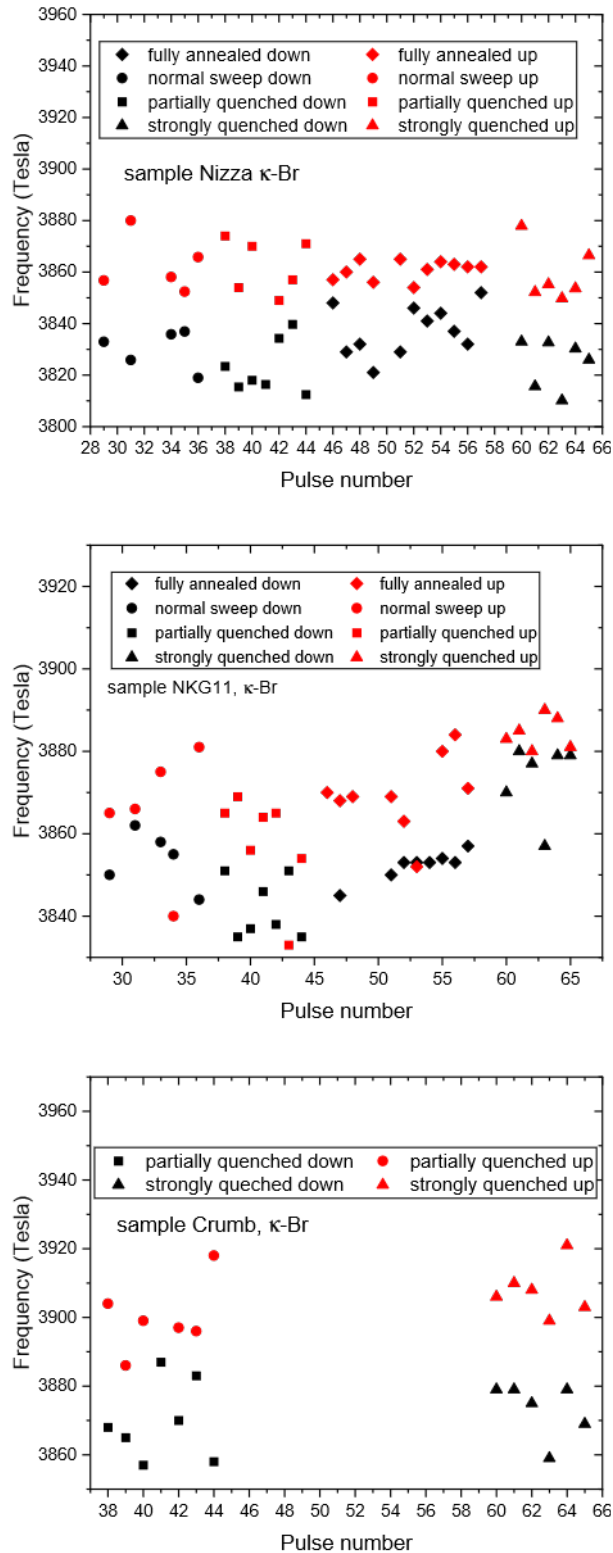


Figure 5.31 Frequencies for the states fully annealed, which is annealing of the samples at 69 K for 60 hours and normally cooled, which is cooling the sample with 1.5 K/min through the glass transition. Further partially quenched which is, running a heat pulse through the sample with a heat pulse duration of 2 s and a maximal temperature of around 100 K and strongly quenched which is running a heat pulse through the sample with a duration of 2 s and a maximal temperature around 120 K. 120 K to 130 K is the range up to which heating up with a heat pulse increases disorder, as shown in section 5.3. **Upper:** sample Nizza, **Middle:** sample NKG11, **Lower:** sample Crumb. The frequencies are plotted over the magnet pulse number, with which they were measured. Pulses 29 till 36 are the measurement of the normal cooled state, pulses 38 till 44 are the measurements of the partially quenched state, pulses 46 till 57 are the measurements for the fully annealed state and pulses 60 till 65 are for the strongly quenched state. The frequencies of the oscillations are only shown for partially and fully quenched states in sample Crumb, as the signal to noise ratio for annealed and normal cooled state is so bad that no oscillations are visible.

5.8.3 Effective masses

At first we want to have a look at the oscillations measured. The oscillations are normalized to the background resistance as the Lifshitz Kosevitch formula gives the amplitude of the Shubnikov-de-Haas oscillations relative to the background magneto-resistance without the oscillations. The background is found by fitting the resistance measured with a parabola in the range from 20 T to 70 T. As an example for the result and the processing to get the effective electron mass, the steps for sample Nizza for the normal sweep cooled state is shown. The data shown is for the down sweep of the magnetic field. The mean magnetic field B_{mean} we need for the fit with the temperature damping we get from the mean of the inverse magnetic field, as the temperature damping factor depends on the inverse of the field.

$$\frac{1}{B_{mean}} = \left(\frac{1}{B_{low}} + \frac{1}{B_{high}} \right) / 2 \quad (5.21)$$

Here B_{low} and B_{high} are the ends of the Fourier transform window. We need the mean magnetic field as we have averaged over the Fourier transform window the magnetic field.

We see that for sample Crumb, that the error bars are quite low, compared to the other samples. Looking at the sample holder used for measuring the effective masses, seen in fig. 4.12, sample Crumb is close to the thermometer at the same height and should therefore be well coupled and equilibrated with the thermometer. This reduces the error in temperature and this way the error bar for the quenched states is lower than for the other two samples. Sample Crumb shows in about the same effective mass for both quenched states for the up and down sweep of the magnetic field. We do not have the effective masses for annealed and normal cooled state as we do not see oscillations above noise level there. Comparing to Stalcup et al. [10] and Weiß [9], who both report $m_c/m_e = 6.4$ for the annealed state, the effective cyclotron masses of about 6.6 to 6.7 for quenched state would be increased. For the other samples, where we see oscillations in the annealed state, we find also an effective mass of about 6.4 ± 0.2 although with a considerable error bar. It is noteworthy that the annealed state was measured for 12 different temperatures, which by statistics should give a more accurate result. The normal cooled state for sample Nizza measured for the down- and up-sweep of the magnetic field do show are strongly reduced mass of 5.8 although with a high error bar. For sample NKG11 for the down sweep, the effective mass is about 6.4 also with a high error bar. For the up sweep however the mass is strongly reduced but also depends strongly on the chosen field window for the Fourier transform. Looking at the field over time curve, shown in fig. 4.11, we see that the field sweep is much faster for the up sweep than for the down sweep. Therefore the down sweep is more accurate as the up sweep as it is slower. Looking again at the sample holder, seen in fig. 4.12 samples NKG11 and Nizza are far from the thermometer and no good heat conductor is in between. Further the normal cooled state was the first state, therefore it may be that the cooling and thermalization procedure was not well enough developed. Further the annealed, and the quenched states were only measured for 6 temperatures, it is unclear if the masses found are due to bad thermalization and equilibration of the samples with the thermometer or if this change in the effective mass is a real physical effect. For the partially quenched state we see an increased mass for sample Nizza for both up and down sweep of magnetic field and for the up sweep of sample NKG11. The mass found is increased to almost 7 ± 0.5 . However on the down sweep of the magnet field for sample NKG11 we do not well see this change in the effective mass. For the strongly quenched state we see even a stronger dependence of the found effective mass on the field window. We can say that the effective mass should be around 6.5 for sample NKG11 but it is hard to tell the true effective mass for sample Nizza. From what we have seen here we can conclude several improvements for the following measurements, listed in subsection 5.8.4.

5.8.4 Conclusions on measuring effective mass

The measurement of effective electron masses proves difficult given the current setup. Although the measurement of oscillations we achieved, setting and controlling the temperature precise enough was not possible with the necessary accuracy in some cases. This led to big scattering in the measured effective masses. The following ideas may reduce the encountered problems.

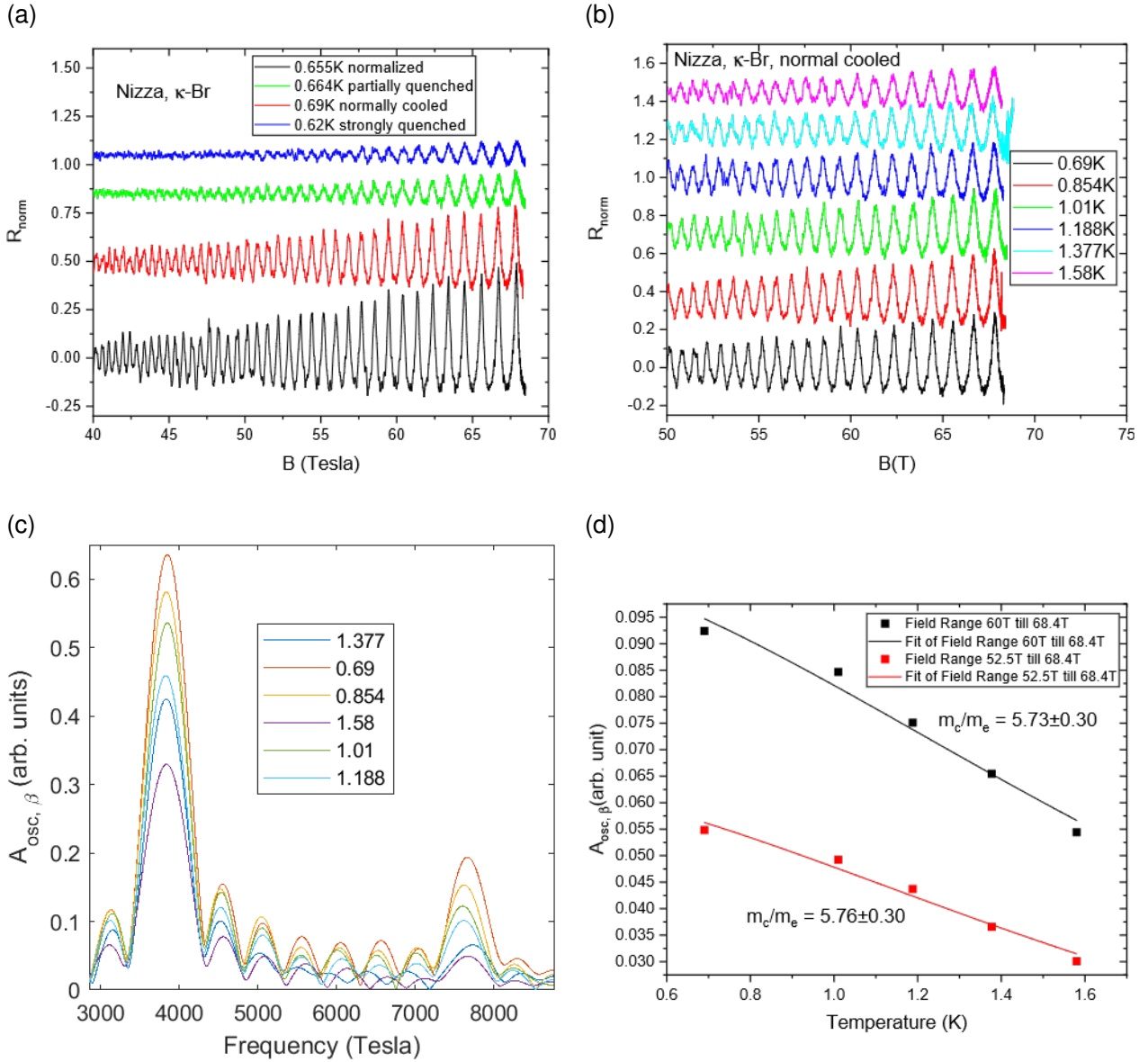


Figure 5.32 States of samples as described in fig.5.31 **Upper left (a)**: The magneto-oscillations at base temperature measurements for each state. Clearly visible is a strong decrease in amplitude with increasing disorder. **Upper right (b)**: For the normal cooled state, the measured magneto-oscillations are shown for all temperatures measured. **Lower left (c)**: The Fourier transforms of the measurements shown in (b) for a field window from 60 T to 68.5 T. We see the first order of the β -orbit and the first higher order at twice the frequency. **Lower right (d)**: The fits to the amplitudes of the Fourier transform with the temperature damping of the Lifshitz-Kosevitch formula. We get for the effective electron masses $m_c/m_e = 5.73 \pm 0.30$ and 5.76 ± 0.30 .

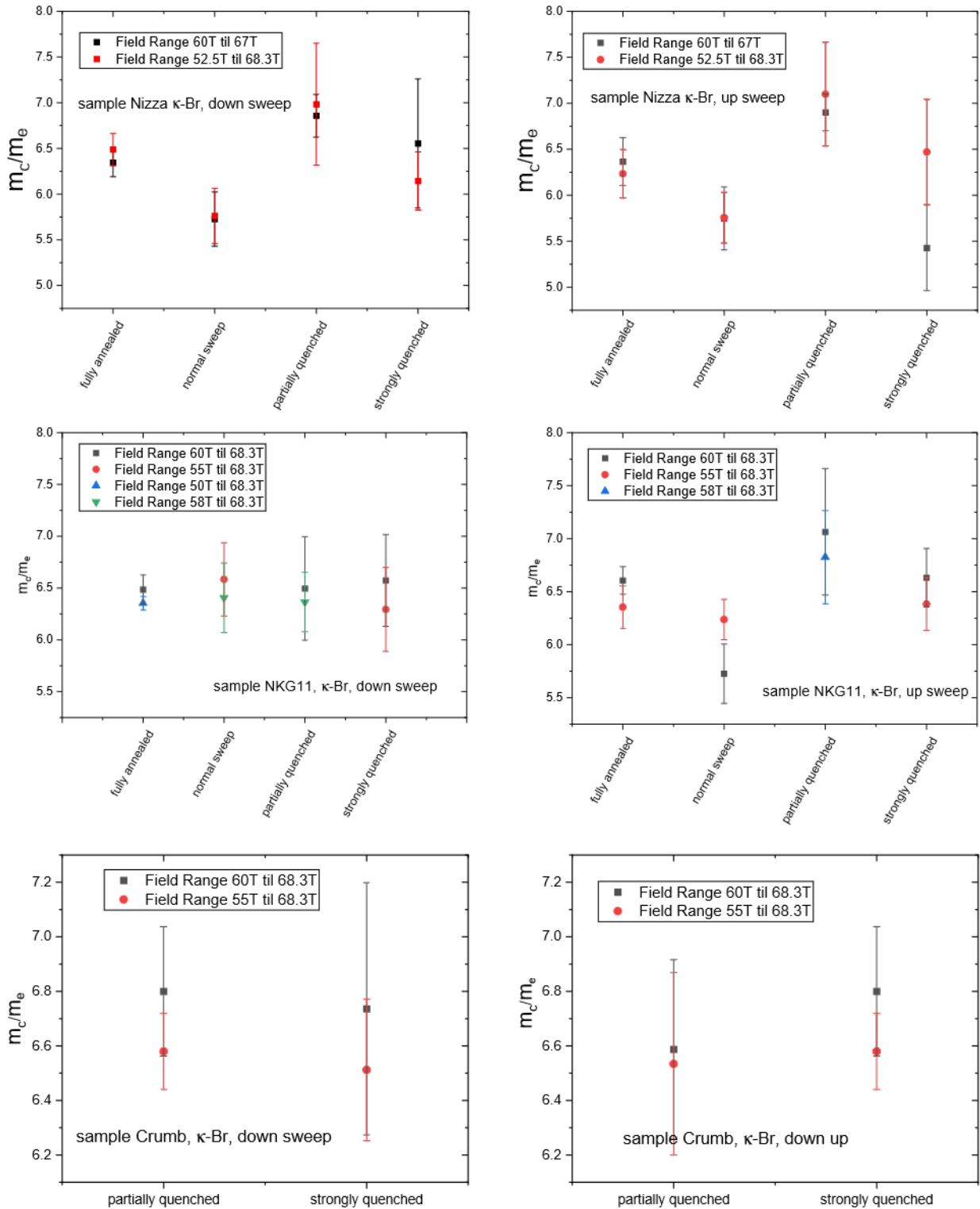


Figure 5.33 Effective electron masses for the states fully annealed, normally cooled, further partially quenched and strongly quenched. The states are described in fig. 5.31.

- Couple thermometer and samples thermally well, eg. via a good heat conducting insulator. An electric conductor would conduct heat well but would also have strong eddy currents which would heat samples and thermometer strongly. This would lead to temperature of samples and the thermometer changing significantly during the pulse and would make the analysis more complicated.
- Mount the samples as close to the thermometer and each other as possible to minimize temperature differences due to temperature gradients. This should allow for a better comparability of the samples.
- Do not do test magnet pulses once the final temperature is reached. A test magnet pulse may only be done at 4.2K, the normal state of the cryostat or at 1.4K respectively 1.6K when the cryostat is pumped to lower the temperature. Once the pumping of He3 has started only the magnet pulse for measuring should be done due to the very delicate nature of cooling and stabilizing temperature with the He3 system.
- Do not wait too long once the temperature is stabilized. In some cases already after 8 minutes especially for the lowest temperatures, the temperature starts to rise and jump. It is recommended not to wait longer than 7 minutes.
- Use a compound closer to the Mott-metal-insulator transition from which to expect a stronger change in the effective mass.
- Get pick-up coil and samples as close together as possible to minimize undetected mismatches, between samples and pick-up coil, in the local magnetic field .
- Increase the number of temperatures at which oscillations are measured to improve statistics. As was found for the annealed state, 12 different temperatures may well decrease the error bar down compared to the error bars for the other measurements where the oscillations were measured only at 5 to 6 different temperatures. This can be well seen on the down sweep of sample NKG11. It may also be beneficial to repeat temperatures after stabilization and other errors might average out this way.

In general it should be possible to measure the effective masses with the pulse magnets. We found some difficulties but in general we can say that we succeeded in finding the magneto-resistance oscillations and were able to extract the effective mass, but some improvements are possible and would increase accuracy.

6 Summary and Outlook

We have improved the heat pulse technique developed by Hartman et al. [8], such that we can record $R(t)$ during the entire heat pulse which allows, using $R(T)$ measured before and after the pulse, to calculate $T(t)$ and $dT(t)/dt$, as shown in section 4.5 and section 5.3. We can qualitatively investigate phenomena with a time dependent resistance, as shown in subsection 5.4.1. Further we can easily find the final temperature of the pulse, which allows to rapidly heat up the sample and cool it down, without the need to stay at a certain temperature for prolonged time, trying to find the final temperature. This avoids heating the cooling surroundings unnecessarily and allows for higher cooling rates.

We have found a hysteresis in the resistance at the glass transition, for both κ -Br and κ -Cl, shown in section 5.4, which has not been previously reported. We found that it can be shifted in temperature by different cooling and warming rates in the same way as the glass transition is shifted, which implies a common cause. In κ -Cl we found that it should end at a pressure of around 1350 bar, however more measurements are necessary to exactly determine the pressure at which the hysteresis ends. Further it should be investigated if we still see a glass transition once the hysteresis has ended. As we have found a hysteresis in κ -Cl and κ -Br, it may be interesting to investigate the hysteresis in their deuterated variants, as well as for other materials in the family of κ -(BEDT-TTF)₂X salts and other organic charge transfer salts that show a glass transition.

We have been able to move κ -Cl in the phase diagram, by disordering the ethylene endgroups with a heat pulse. The movement we found to be equivalent to 20 to 40 bar of pressure, as shown in section 5.5. It is shown by Hartman et al. [8] that one can move partially deuterated κ -Br in the phase diagram by disordering the ethylene endgroups, similar to applying hydrostatic pressure. We have seen that the starting temperature of the hysteresis above the superconducting transition in κ -Cl has a strong dependence on the pressure applied, as shown in section 5.5. However looking at the hysteresis above the superconducting transition in κ -Br, we find a strongly different behaviour. The starting temperature of the hysteresis is about 20 K, independent of the disorder of the ethylene endgroups, as shown in section 5.6. This then would be an argument against disorder acting purely as hydrostatic pressure.

We found a change in the critical temperature of superconductivity T_c with increasing disordering of the ethylene endgroups. Anderson's theorem [43] states, that in case of s-wave pairing in superconductors, impurities that are nonmagnetic, do not change T_c . This implies that we either create magnetic impurities by disordering the ethylene endgroups, which is possible as we approach a transition to an antiferromagnetic state. Otherwise we might have a non pure s-wave pairing in the superconductor, as Powell and McKenzie discuss [42]. We can calculate the expected change in T_c over the residual resistance, by the formula of Abrikosov and Gorkov [44] and we find that our results do not agree with their formula, as the decrease of T_c apparently saturates with increasing residual resistivity, as shown in section 5.7. A possible explanation for our result is that we have a superconductor with s- and non s-wave pairing where only the non-s-wave pairing is suppressed. Another explanation might be, that, as we approach a transition to an insulator, we overestimate the change in the defect density from the change of residual resistivity. The change of T_c over the true defect density then may follow the formula of Abrikosov and Gorkov [44].

We measured and found Shubnikov-de-Haas oscillations in κ -Br, for the entire range of states of ordered and disordered ethylene endgroups, shown in section 5.8. We see that the effective carrier mass stays constant within the error bars. The error bar is quite considerable, which for future measurements should be reduced by changes to the setup, as described in subsection 5.8.4. This includes measuring the change in the carrier effective mass in deuterated κ -Br as it is closer to the Mott-metal-insulator-transition and we therefore expect a larger change.

A Appendix

A.1 Table of Samples

To simplify the tracking of samples over different measurements, the samples were given names. Sample name, reason for name, compound and fabrication batch are given in table A.1. Resistance at room temperature $R(293\text{K})$, peak temperature T_{peak} , resistance at peak R_{peak} and resistance at superconductive entrance $R(14\text{K})$ are given in table A.2. Area locking onto the layers A, sample thickness d and a view onto layers of each sample are given in tables A.3, A.4 and A.5. The area A is the area of the conducting layers.

A.2 Hints on soldering small wires

Soldering small wires, as for example on the pressure setup can be very tedious. The much bigger tip of the soldering iron tends not only to solder the desired contact but also the nearby contacts which may have already been soldered and destroys the soldering or undesirably connects two contacts. To mitigate this one can cover the contacts with colophony entirely, a soldering fluxant. This has the beneficial effects

- The colophony protects the contacts that should not be heated from the heat of the soldering iron such that they do not melt unless directly touched by the soldering iron.
- It makes sure that the entire soldered contact is covered in fluxant therefore avoiding oxidation and giving best coverage of wires with the soldering tin.
- It stabilizes the tin on the soldering iron's tip such that it does not easily flow to neighbouring contacts and prevents further oxidation once the tip is inside the colophony.

Due to the simplicity of the technique and the long history of soldering it is sure that the author of the thesis is not the first to discover this. It was however redeveloped by the author during the thesis and found to be highly useful, thus sharing this hint in the appendix of the thesis.

sample name	reason for name	compound	batch
Crumb	named after its rough surface	κ -Br	EK89
Nizza	found with only information about material and that it was measured in Grenoble, therefore named after another french city close to Grenoble	κ -Br	batch unknown
NKG 11	named after sample batch	κ -Br	NKG 11
NKG 7	named after sample batch also named after its resistance ratio $R_{peak}/R(T=14K)=215$ ratio	κ -Br	NKG7
Atlas	like Crumb named after his shape named after a mountain range	κ -Br	EK89
Hepheistos	most of the heat treatment technique development was done on this sample therefore named after the greek good of fire and forging.	κ -Br	EK89
Vesuv	burned during heat pulse technique development, therefore named after a vulcan	κ -Br	EK891B
Wedge	looks like a wedge	κ -Br	EK 89
Superhero	named as used in many measurements previous to this	κ -Cl	
Secret hero	first measurement together with Superhero, used for measuring annealing in Cl under pressure and heat pulsing under pressure	κ -Cl, deuterated	NKG 57-78
AFCL3	named after batch measured by Sebastian Oberbauer in 2015	κ -Cl	AFCL3
LBS	Little Big sample for full, was named as it is a small piece of a much bigger sample	κ -Cl	PC17

Table A.1 Table of samples part 1.

sample name	R(293k)[Ohm]	T_{peak} [K]	R_{peak} [Ohm]	R(14K)[Ohm]
Crumb	435	flat peak	-	4.51
Nizza	794	65.57	1754	15.07
NKG 11	656	63.35	1619	20.83
NKG 7	1115	91.97	1717	7.69
Atlas	294	69.98	534	12.04
Hepheistos	276.5	65.86	689	8.14
Vesuv	27.69	flat peak	-	2.79
Wedge	1641	50.32	7732	609
Superhero	580	-	-	R(14k)[Ohm]
Secret hero	143	-	-	R(14k)[Ohm]
AFCL3	1148	25.71	166115	664703(@10K)
LBS	474	13	32 MOhm	23.1 MOhm(@10K)

Table A.2 Table of samples part 2. All values that depend on thermal history are for a cooling of 2K/min through T_g

sample name	A[μm^2]	d[μm]	view onto layers
Crumb	422009	255.15	
Nizza	307242	333.17	
NKG 11	360927	389.25	
NKG 7	168900	587.82	

Table A.3 Table of samples part 3.

sample name	A[μm^2]	d[μm]	view onto layers
Atlas	498612	335.33	
Hepheistos	650247	511.51	<p>In the middle, the hole is visible, that was burned through the sample</p>
Vesuv	-	-	
Wedge	85209	162.15	

Table A.4 Table of samples part 4.

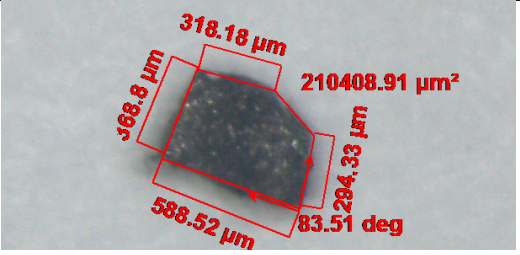
sample name	A[μm^2]	d[μm]	view onto layers
Superhero	-	-	-
Secret hero	210408	162.15	
AFCL3	-	-	-
Little Big sample	-	-	-

Table A.5 Table of samples part 5.

A.3 Heat pulse program and data evaluation

A.3.1 The measurement program.

This program was developed from the Zurich Instruments MFLI tutorial "204_SubscribePoll_StreamingNode.vi", but heavily modified. The tutorial only explains how to use the different .vi files provided by Zurich Instruments to facilitate operation of the lock-ins. All of the named .vi files in the following are provided by Zurich Instruments together with the MFLI lock-ins. The measurement program does the following:

- Connects to the MFLI lock-ins, maintains the connections and closes them when the program is stopped, via the LabView programs "ziOpen.vi" and "ziClose.vi".
- Upon pressing the "request heat pulse" button
 1. the program subscribes to the measurement channels of the MFLI lock-ins via "ziSubscribe.vi"
 2. checks if the measurements are running by making sure that the first two packets of measurement data arrives and no errors are reported. This is done by waiting in "ziPollDataEx.vi" for the measurement data to be available. Then by "ziGetEvent.vi" in the "Demod Sample" configuration the measurement data is fetch from the MFLI lock-ins data server.
 3. if everything is working, a request for a heat pulse is written into a shared variable by setting this variable to True. This is interpreted by the heat pulse program and will be further described there.
 4. the data is read from the MFLI lock-ins in a for loop until the set measurement duration is reached. Reading from the MFLI lock-ins works in the same way as getting the two test measurements. The read data is displayed on two waveform graphs and the time of start of the measurement is noted. The waveform graphs allow to display a continuous stream of measured data and already give an idea during measuring the heat pulse on how successful the heat pulse was.
 5. after the measurement duration is reached, the measurement channels are unsubscribed via the respective "ziUnSubscribe.vi"
 6. To calculate the resistance the measured voltage drop over the sample and the measured voltage drop over the reference resistor are interpolated. Further they are synchronised owing to different measurement starting times. From this, the resistance over time is calculated and displayed in a graph for immediate evaluation.
 7. The calculated resistance over time together with the settings of pulse and data acquisition as well as the raw data are stored in the set storing folder.
- The subscribe model is used by the MFLI lock-ins to quickly transfer large amounts of data by

- Subscribing to a measurement channel. This tells the data server of the MFLI lock-ins that somebody is ready to receive the measurement data. It is possible to subscribe to different channels as the MFLI lock-ins with hardware upgrades can have multiple demodulators and therefore multiple measurement channels which measure different inputs but this was not used.
- Wait for data to arrive via "ziPollDataEx.vi". This allows a synchronisation of measurement program and data server and reduces load on the data server. This means that the measurement program doesn't have to constantly ask the data server if new data has arrived. Once new data has arrived the measurement program is notified by the MFLI lock-in data server.
- The measured data is transferred in packets which reduces communication overhead.

The measurement is terminated after the set measurement duration as this is a simple and fail-safe yet well predictable way to limit the data acquisition. To save time and storage space, different termination criteria, like having constant measured current and voltage, are thinkable. This could be used additionally to the time based criteria, but were not implemented in this thesis, as the time based criterion was found to be sufficient.

A.3.2 The heat pulse program.

The main objective of the heat pulse program is to maintain the sample and make sure that a heat pulse is only applied to the sample if all pulse parameters are within the specified limits. The limits are max pulse duration, max current/voltage and maximum deposited energy in the sample. The heat pulse program works in the following.

1. It connects to the source of the heat pulse and in case of the MFLI lock-in maintains this connection and closes the connection when terminating the program. Implemented as heat pulse sources were Keithley 2400 and MFLI lock-in.
2. it checks that all heat pulse parameters are within the specified limits.
3. it makes sure that the output of the heat pulse source is zero when not explicitly applying a heat pulse.
4. it applies the heat pulse via a time sequence in LabView which should allow for precise timing of the pulse.

A.3.3 The steps when applying a heat pulse

The steps when applying a heat pulse are then the following

1. Cool the sample to the desired starting temperature. In our case this was usually 35 K.
2. Connect the sample according to the wiring plan shown in figure 4.7.
3. Settings on the MFLI lock-in
 - Set the sensitivity on both MFLI lock-ins to the maximum value of 3V, to protect them from the pulse voltages.
 - Set the voltage MFLI to external reference AUX In 1
 - Set Input to AC coupling and Differential on both MFLI loc-ins.
 - Set voltage output to 40.03 mV root mean square for the Voltage MFLI and to 700 mV root mean square or peak for the current MFLI. The value for the current MFLI is not so important as this is only for synchronizing both MFLI lock-ins, and both values work well.

- Set frequency and time constant. For all pulses in this master thesis 2474.63499 Hz, 2301 Hz or 2452.18 Hz oscillator frequency and a time constant of 4.078 ms was used. The frequency was chosen to be a multiple of one over the time constant. It was found that also a slight deviation from this frequency works.
 - enter the reference resistance into the measurement program.
4. Start the read out program and make sure that storing folder, notes on the sample, measurement duration and reference resistance value are filled correctly
 5. Start the heat pulse program. Set device, device address, current or voltage source and average sample resistance. Further set all maximal parameter values correctly by first pushing the change the max value button and then setting the new value, as otherwise the changes are rejected. Last, activate the pulse program, by setting the corresponding switch to true.
 6. Do a test pulse, either via the request heat pulse button in the measurement program or in the heat pulse program directly, with zero output to check if everything is working correctly.
 7. Apply the heat pulse, and read from the output graphs if the pulse was successful.
 8. Repeat heat pulse until the desired result is achieved

The 35 K was used as a starting temperature as it does not put too much thermal stress on the sample, but was enough to achieve high enough cooling rates. This in general is part of the strategy to heat the sample only as much as necessary to archive good disordering but also to keep the thermal stress low. It was therefore also avoided to keep the sample at a temperature far above the surroundings longer than necessary. This method has the advantage that it works with lower thermal stress on the sample, which is important especially for samples and compounds with lower mechanical stability.

It was shown by [8] that a partially deuterated κ -Br sample can survive being heated to 307K with the surrounding bath at 6K and then rapidly cooled by turning of the heating voltage through the sample. This should also hold for the fully hydrogenated κ -Br. However, as it is very difficult and time consuming to change a sample in a Helium 3 cooling setup and good samples are best treated with care. Therefore in our case less stressful parameters were chosen. Further keeping a sample at a higher than surrounding temperature warms the surroundings of the sample effectively reducing the achieved cooling rates, especially in the important temperature range several dozen Kelvin above the glass transition. This thermal region is important as we later show in the experimental results region, as it is the one were the annealing rates are on the order of milliseconds and seconds. This means there the ordering rate is not much faster than the cooling rate.

It is highly recommended to apply heat pulses at least in a team of two, to make sure no errors are made. Even with the above safety measures it is possible to make mistakes and potentially damage or destroy the sample.

A.3.4 Getting from R(time) to T(time)

To get from R(time) to T(time), the sample is used as a thermometer. R(T) curves before and after the heat pulse are then matched to the R(time) curve, to get T(time). Using an example pulse, the corresponding measured R(T) and R(time) are shown in each step. The sample pulsed was NKG11 with a heat pulse had duration of 2 s and a pulse voltage of 7.50 V.

Correction resistance measurement for changing measurement current due to changing resistance

To do this precisely one has to correct the measured R(T). The output of the lock-in amplifier is a constant voltage and no correction to keep the current constant exists in the used lock-ins. To avoid to strong

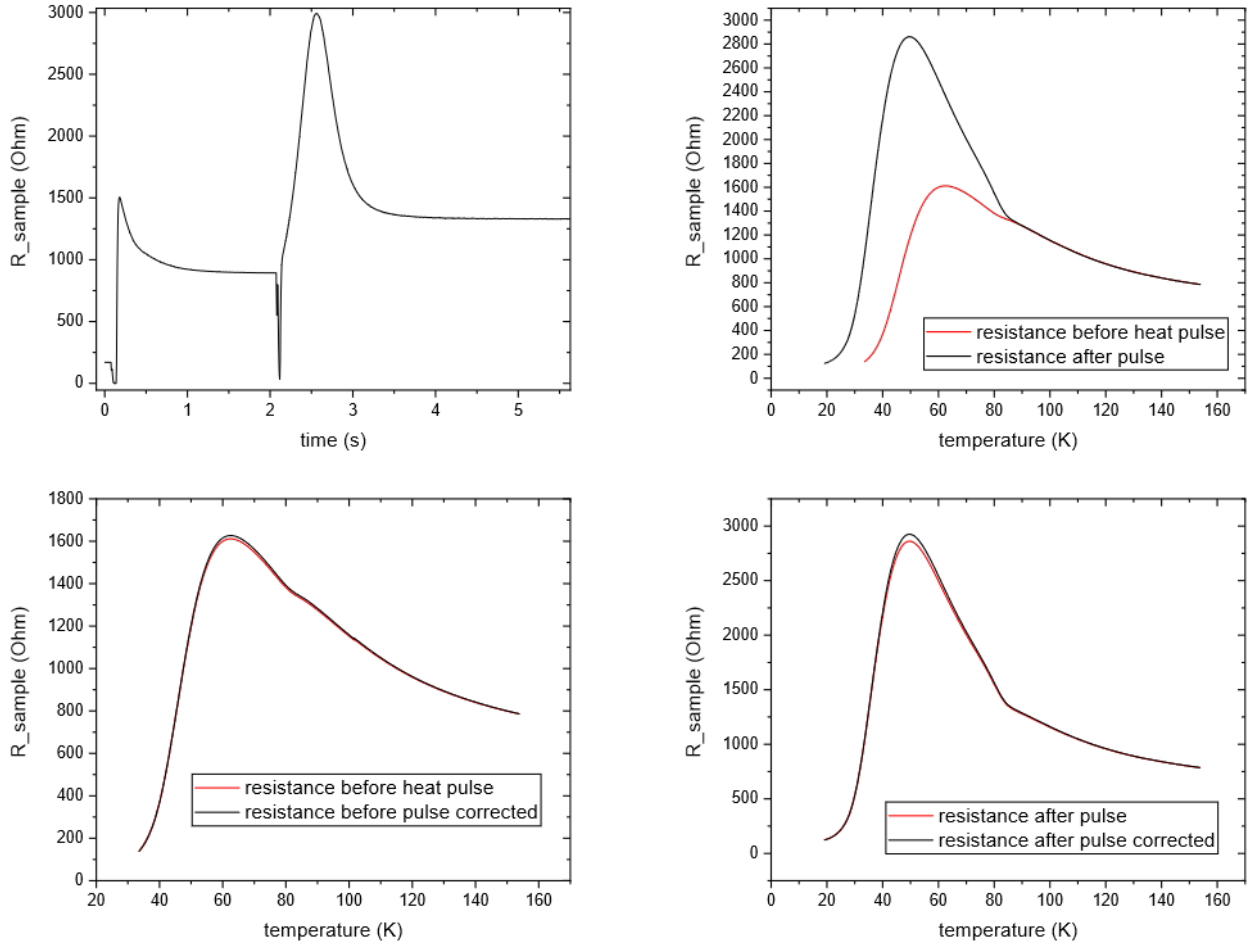


Figure A.1 Upper left: Heat pulse measured. Noticeable are the start and end of applying the pulse voltage, which are marked by very sharp drops at 0.1 s and 2.1 s where the resistance measurements are not possible. This is as there the dc bias voltage off the MFLI lock-ins is switched on and off which makes measuring there difficult for the lock-ins. The pulse duration was 2 s and the pulse voltage 7.5 V. The entire recording duration of the pulse is 25 s, to be sure that if anything happens it is recorded although after 5 s everything has been found to be in a steady state. **Upper right:** The measured resistances over temperature before and after the pulse **Lower row:** Resistance over temperature corrected by equation A.11

changes in current and to be able to use that the current is approximately constant a load resistance is chosen that is several orders of magnitude larger than the sample resistance.

This approximation is not good enough when trying to match the measured $R(T)$ to $R(\text{time})$. One therefore has to correct for the change in current as derived in the following. Looking at the resistance measurement wiring plan 4.1 the measurement current I_{meas} through the sample is

$$I_{meas} = \frac{V_{osc}}{R_{load} + R_{sample} + 100\Omega} \quad (\text{A.1})$$

with V_{osc} the voltage output of the lock-in amplifier and R_{sample} the resistance of the sample. We omit to write the T dependence for simplicity. From this, the voltage drop over the sample V_{meas} can be calculated

$$V_{meas} = I_{meas} R_{sample} \quad (\text{A.2})$$

The resistance of the sample then can be calculated from the measured voltage drop by

$$R_{sample} = \frac{V_{meas}}{I_{meas}} = \frac{V_{meas}(R_{load} + R_{sample} + 100\Omega)}{V_{osc}}. \quad (\text{A.3})$$

Rearranging we get

$$R_{sample} \left(1 - \frac{V_{meas}}{V_{osc}} \right) = (R_{load} + 100\Omega) \frac{V_{meas}}{V_{osc}} \quad (A.4)$$

$$R_{sample} = (R_{load} + 100\Omega) \frac{V_{meas}}{V_{osc}} \frac{V_{osc}}{V_{osc} - V_{meas}} = (R_{load} + 100\Omega) \frac{V_{meas}}{V_{osc} - V_{meas}} \quad (A.5)$$

V_{osc} is set such that at room temperature, the voltage drop over the 100Ω reference resistor is $1 V \frac{100\Omega}{R_{load}}$. This means that we get an factor c_{VtoR} as a power of 10 to convert from measured voltage to sample resistance. At room temperature we have

$$R_{sample}(T_{room}) = c_{VtoR} V_{meas}(T_{room}). \quad (A.6)$$

Further we have that the resistance stored R_{stored} in the measurement data files follows the equation

$$R_{stored} = c_{VtoR} V_{meas}. \quad (A.7)$$

Inserting this into A.5 we get

$$R_{sample} = (R_{load} + 100\Omega) \frac{\frac{R_{stored}}{c_{VtoR}}}{V_{osc} - \frac{R_{stored}}{c_{VtoR}}} \quad (A.8)$$

We know that $R_{stored}(T_{room}) = R_{sample}(T_{room})$ as we did set everything to have this equality. Together with equation A.8 we get

$$1 = \frac{R_{load} + 100\Omega}{c_{VtoR}} \frac{1}{V_{osc} - \frac{R_{stored}(T_{room})}{c_{VtoR}}} \quad (A.9)$$

This can be rewritten to

$$V_{osc} - \frac{R_{stored}(T_{room})}{c_{VtoR}} = \frac{R_{load} + 100\Omega}{c_{VtoR}} \quad (A.10)$$

Inserting this again into equation A.8 we get

$$R_{sample}(T) = R_{stored}(T) \frac{V_{osc} - \frac{R_{stored}(T_{room})}{c_{VtoR}}}{V_{osc} - \frac{R_{stored}(T)}{c_{VtoR}}}. \quad (A.11)$$

Here for the final equation the temperature dependence was explicitly noted. This formula can be understood that for resistances above $R_{sample}(T_{room})$ the sample resistance is increased. This is as the measurement current due to the higher resistance is reduced and the voltage drop over the sample is decreased. To get the true resistance the stored resistance has to be increased and vice versa for resistances below the room temperature resistance.

Matching peaks of resistance over time and resistance over temperature

As the the next step the the peaks of $R(\text{time})$ and $R(\text{temperature})$ are matched. This is useful for numerical reasons as this way for each value of $R(\text{time})$ there is a value in $R(\text{temperature})$ and there is no jump in $T(\text{time})$. Further it is possible that the resistance measured during the pulse is slightly incorrect due to the fast changes of $R(\text{time})$. On one side this is due to the averaging over a time window which leads to the peak being lowered due to averaging over it. On the other hand the change in $R(\text{time})$ may introduce a frequency component of the same frequency as the lock-in frequency, which is then measured as a higher or lower resistance. Further it may be that the reference resistance used for measuring the current through the sample is slightly higher than the 100Ω we used in the calculation. The device and setup used were never designed for this task therefore some extra contact resistances may have to be taken into account.

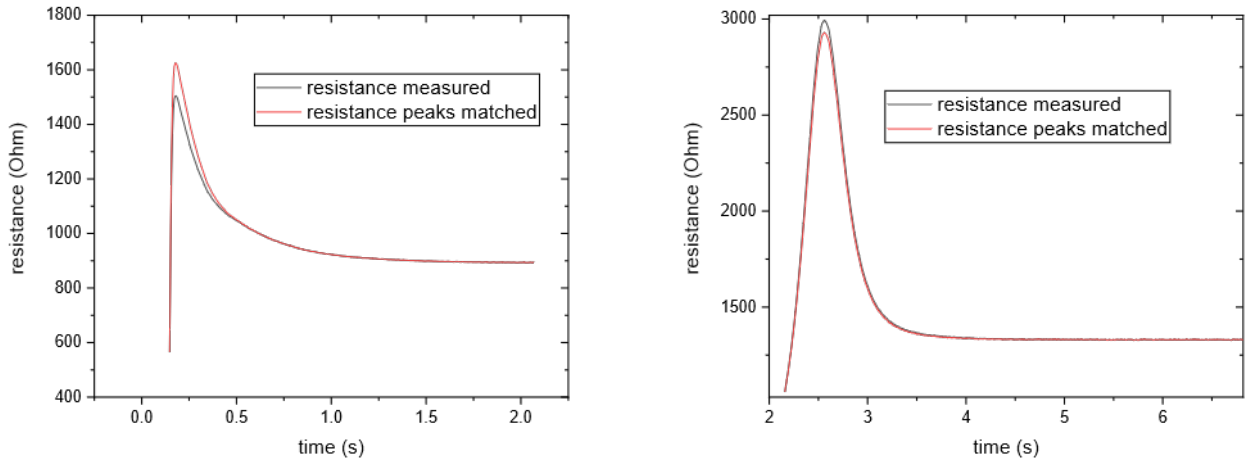


Figure A.2 Left: Resistance during heat pulse. The change due to the matching is quite big as the peak has been reached very early and due to the averaging process of the lock-in it is reduced in height. **Right:** Resistance after the heat pulse. Only the first part is shown where the matching changes the resistance.

For this the resistances in $R(\text{time})$ are modified by mapping the resistances linearly $[\min(R(\text{time})), \max(R(\text{time}))] \mapsto [\min(R(\text{time})), \max(R(\text{temperature}))]$. The matched $R_{\text{peak-matched,inter}}(\text{time})$, with t short for time, is calculated via the formula

$$R_{\text{peak-matched,inter}}(t) = \frac{R(t) - \min(R(t))}{\max(R(t)) - \min(R(t))} \max(R(T)) + \frac{\max(R(t)) - R(t)}{\max(R(t)) - \min(R(t))} \min(R(T)) \quad (\text{A.12})$$

As the mismatch in the resistances is a dynamic effect the resistance correction should be reduced at lower temperature gradients. For simplification this is done by exponentially damping the correction with time. Precisely this is done by a Gaussian function centered at the peak, as this allows to match the peaks exactly but does not change the resistance strongly elsewhere. A disadvantage is that the rising resistance at the very beginning is not corrected. Correcting this resistance is very difficult and could be done by lowering the time constants of the lock-in, which then might bring other problems with it. The solution taken here is to consider a large error for the temperature gradient at the beginning of the pulse and the cooling phase after the pulse. The final $R_{\text{matched}}(t)$ is then calculated by

$$R_{\text{peak-matched}}(t) = \left[\left(\frac{R_{\text{peak-matched,inter}}(\text{time})}{R(\text{time})} - 1 \right) \exp\left(-\frac{(t - t_{\text{peak}})^2}{\sigma^2}\right) + 1 \right] * R(t) \quad (\text{A.13})$$

where σ is the broadness of the Gaussian and was chosen as 0.3 in for this thesis. This formula works by taking the change factor from A.12, reducing it by 1 and multiplying with a Gaussian and then adding the 1 again to get the change factor. This way the change of the resistance is damped and once the Gaussian is close to zero the resistance remains the unchanged. Further by subtracting the one, it is made sure that if the peaks already match perfectly the resistance is untouched. This factor is then multiplied to $R(\text{time})$ to match the peaks of $R(\text{time})$ and $R(T)$. A Gaussian was chosen as it is one at the center and therefore the peaks are matched perfectly. It is also smooth and has a smooth derivative, which is important when it comes to calculating the gradient of $T(\text{time})$.

Matching resistance over time to resistance over temperature.

Finally the resistances in $R_{\text{peak-matched}}(\text{time})$ are matched to the resistances in $R(T)$. This is done for the part of $R_{\text{peak-matched}}(\text{time})$ during the heat pulse and after the heat pulse separately. The procedure is the same for both parts.

To match $R_{\text{peak-matched}}(\text{time})$, it is necessary to interpolate $R(T)$. This is done by interpolating $R(T)$ in two parts one before the peak and another after the peak. This is to make sure that everything before and

after the peak in $R_{peak-matched}(time)$ is matched accordingly to $R(T)$. Namely for $R_{peak-matched}(time)$ during the pulse, the part before the peak in $R_{peak-matched}(time)$ is matched to the part of $R(T)$ before the peak and the part in $R_{peak-matched}(time)$ after the peak to the part after the peak in $R(T)$. For the part after the pulse this is done with swapped $R(T)$ before and after the pulse as the temperature now changes in the opposite direction. For the interpolation a cubic spline was used. Calculating the $T(t)$ during cooling is made difficult above the glass transition as in the cooling phase of the heat pulse the disorder is frozen in while during measuring $R(T)$ after the pulse when going above the glass transition the disorder is relaxed leading to a different $R(T)$ than with constant disorder. This shows above 80 K in the temperature gradients for the cooling.

The matching for each value $R_i(time)$ in $R_{peak-matched}(time)$ is done by minimizing

$$\min_T (R_{interpolated}(T) - R_i(time))^2 \quad (\text{A.14})$$

where $R_{interpolated}(T)$ is the interpolated part of $R(T)$. To get unique results it was demanded that the temperature is constantly rising during the pulse and constantly falling after the pulse. Only when coming close to the final temperatures of cooling and warming this restriction was lifted, to avoid having problems with the noise of the resistance measurement.

It is noteworthy the difference in the maximum temperature found during the pulse and after the pulse. This difference is from the time during the switching off of the dc bias voltage, which due to the high cooling rates already allows for a significant cooling of the samples.

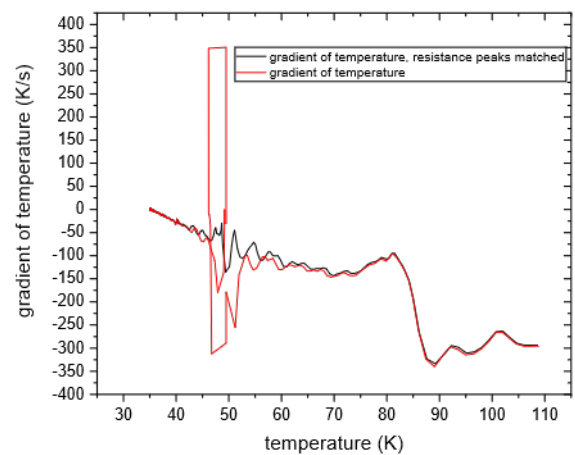
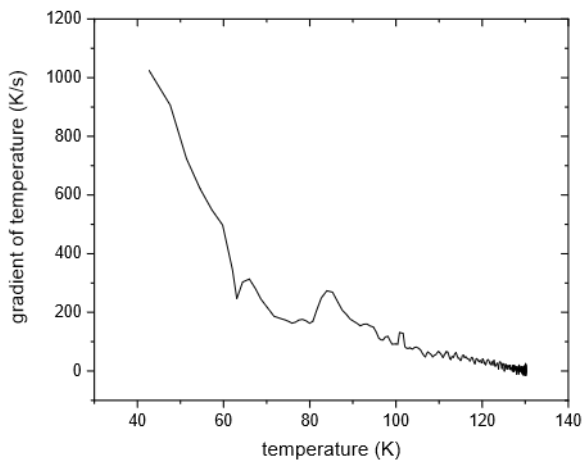
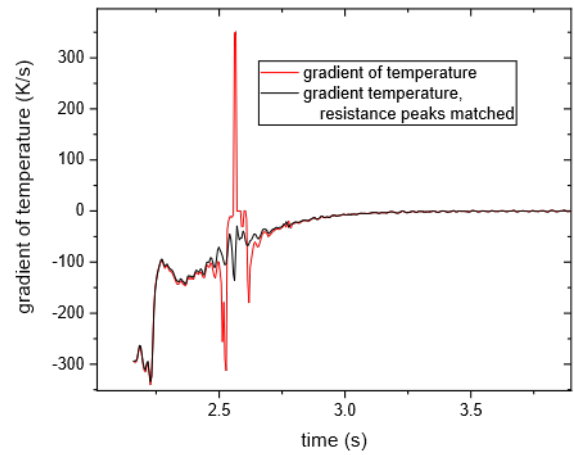
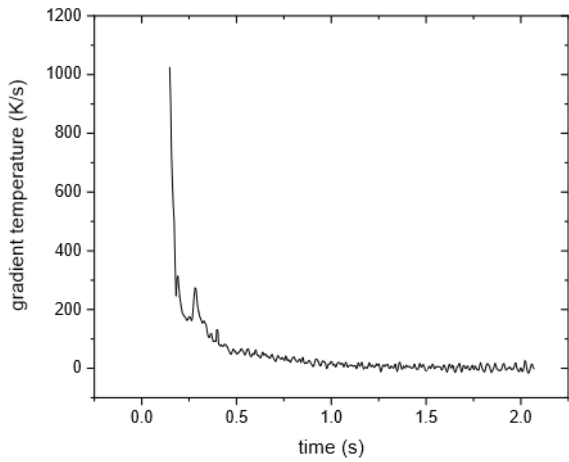
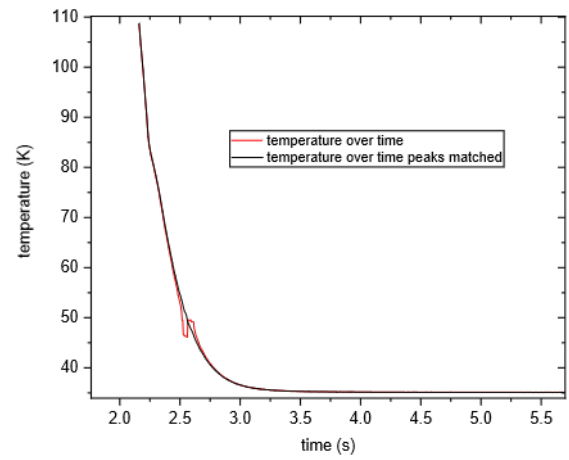
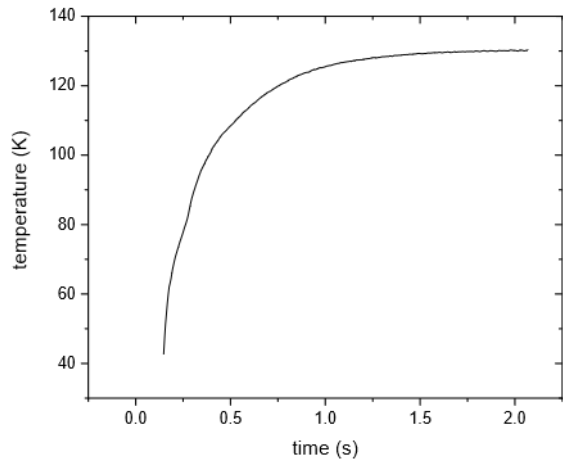


Figure A.3 The left column is during the pulse and the right column is after the pulse **Upper row:** temperature over time during and after the pulse. Especially during the pulse the first few measurement points are somewhat incorrect. **Middle row:** Gradient of temperature over time. The first points especially during pulse have a large error bar and should serve more as estimate. **Lower row:** Gradient of temperature over temperature

A.4 Remainder of figures from κ -Cl under pressure

Here are the figures for the comparison of the annealed states at 63 K and 64.5 K as described in section 5.5.

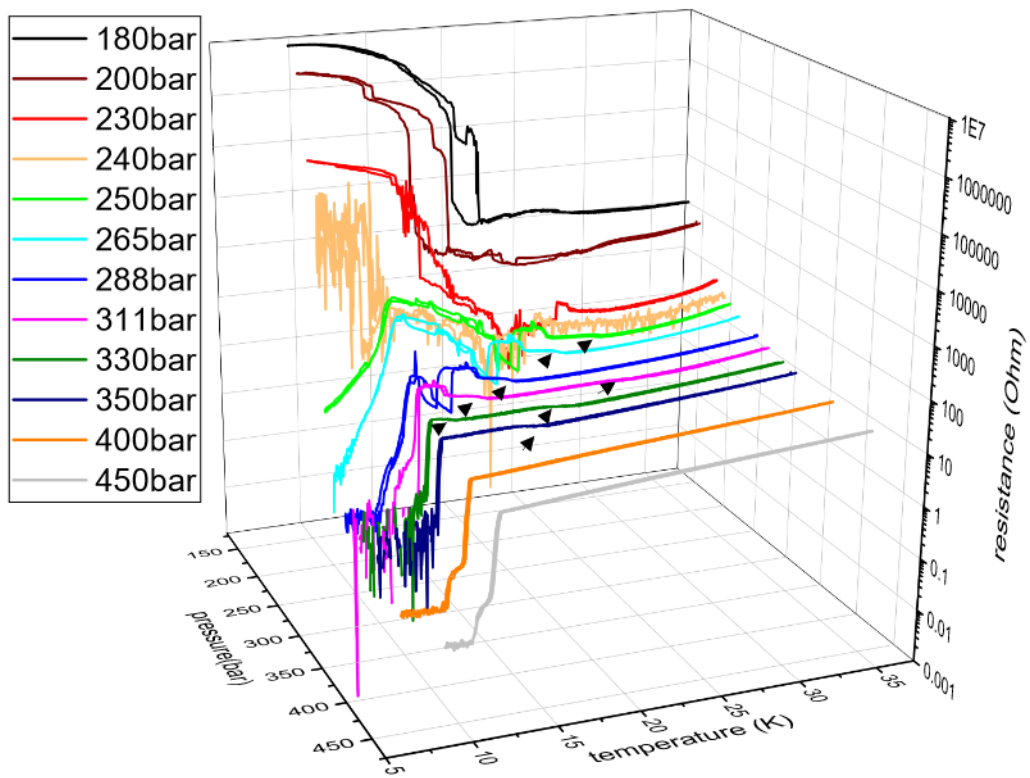
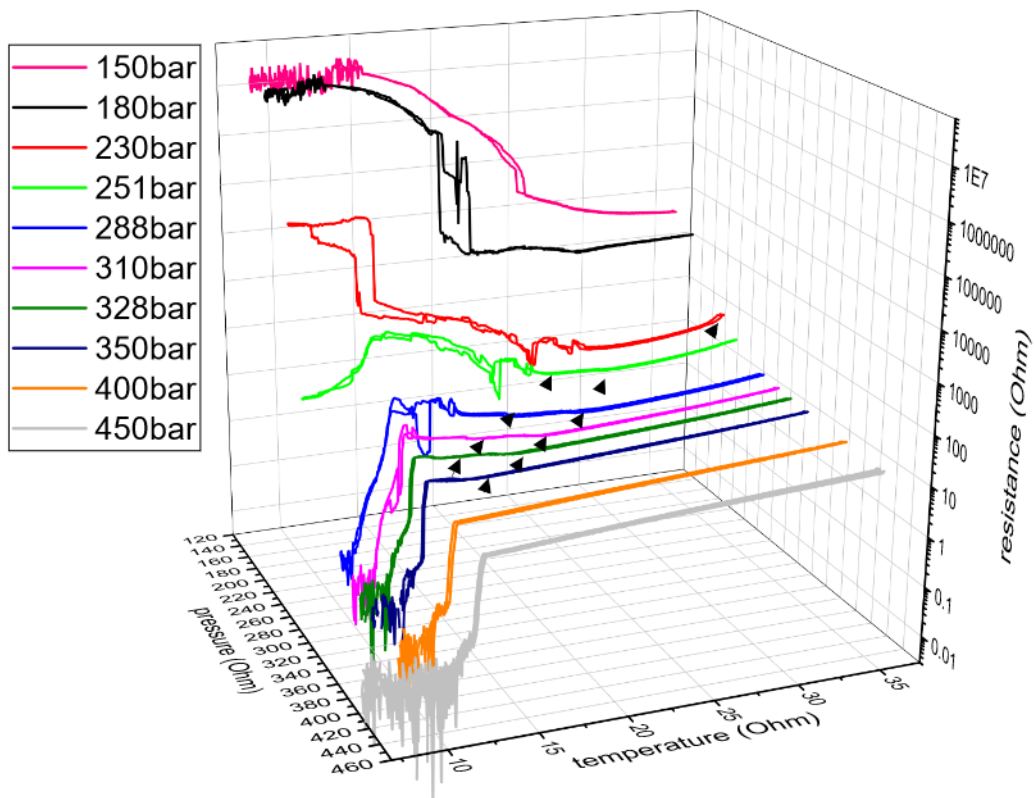


Figure A.4 Resistance over pressure and temperature for Little big sample **Top:** Annealed at 63 K for 50 h. **Bottom:** Annealed at 64.5 K for 24 hours. The arrows in both case indicate steps in the resistance.

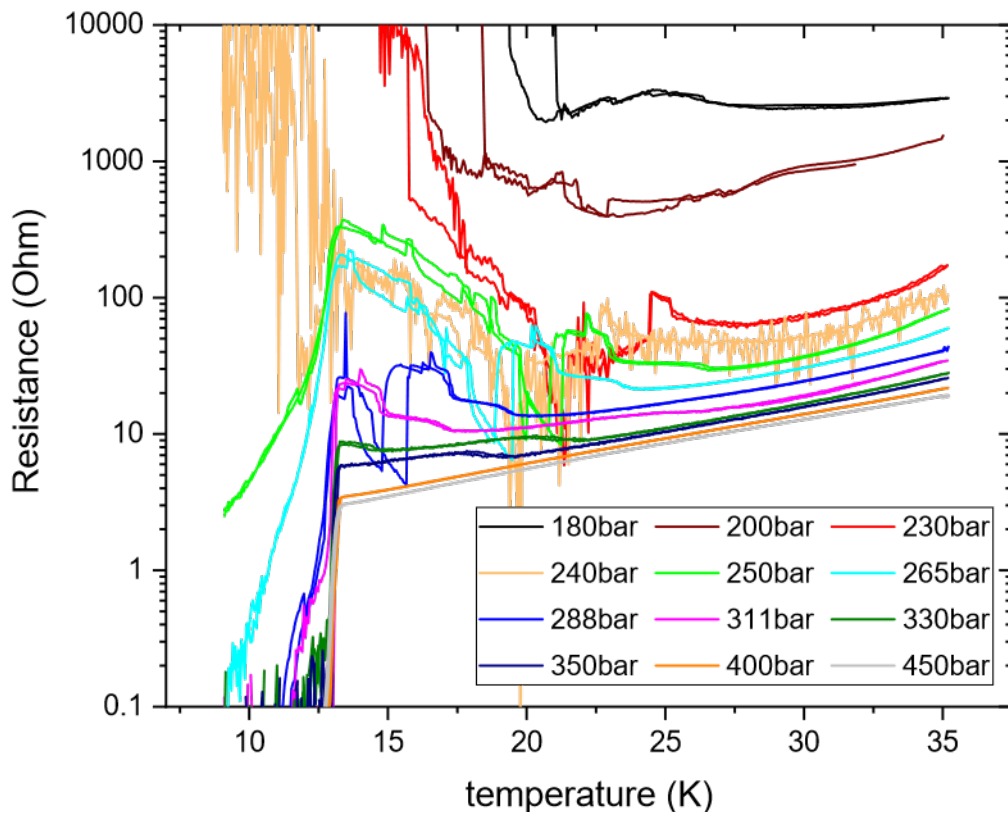
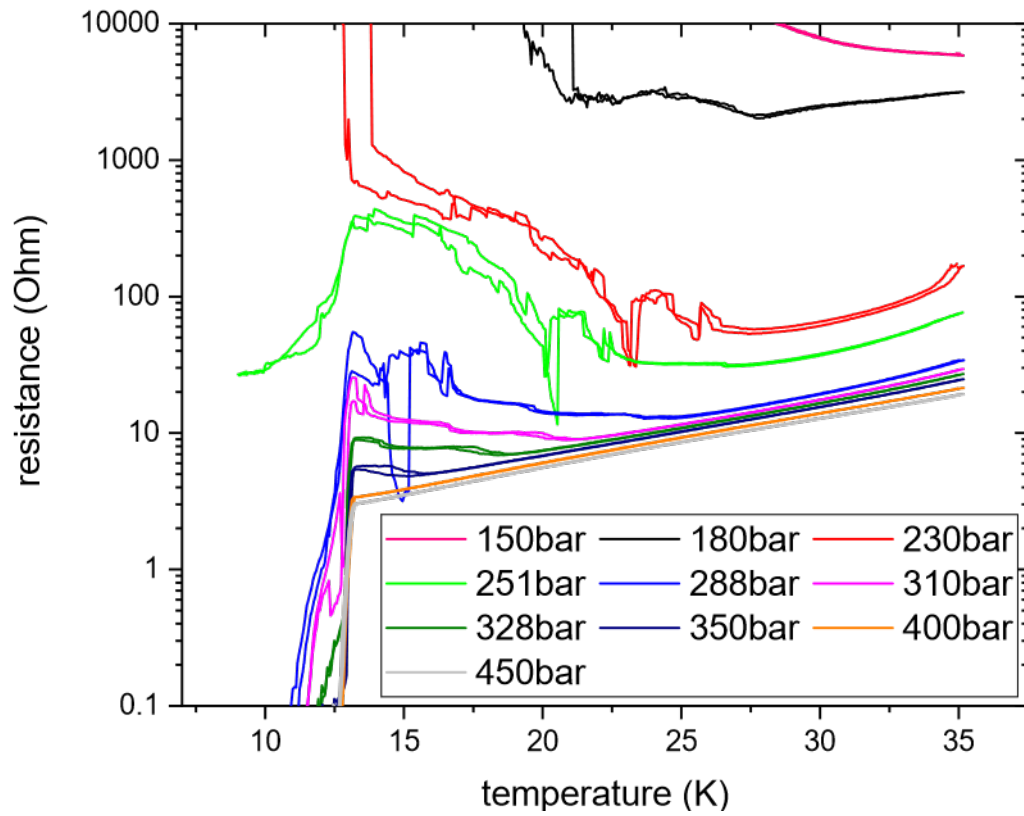


Figure A.5 Resistance over temperature for Little big sample. **Upper:** Annealed at 63 K. **Lower:** Annealed at 64.5 K for 24 hours. Colouring for each pressure is the same as in fig. 5.17.

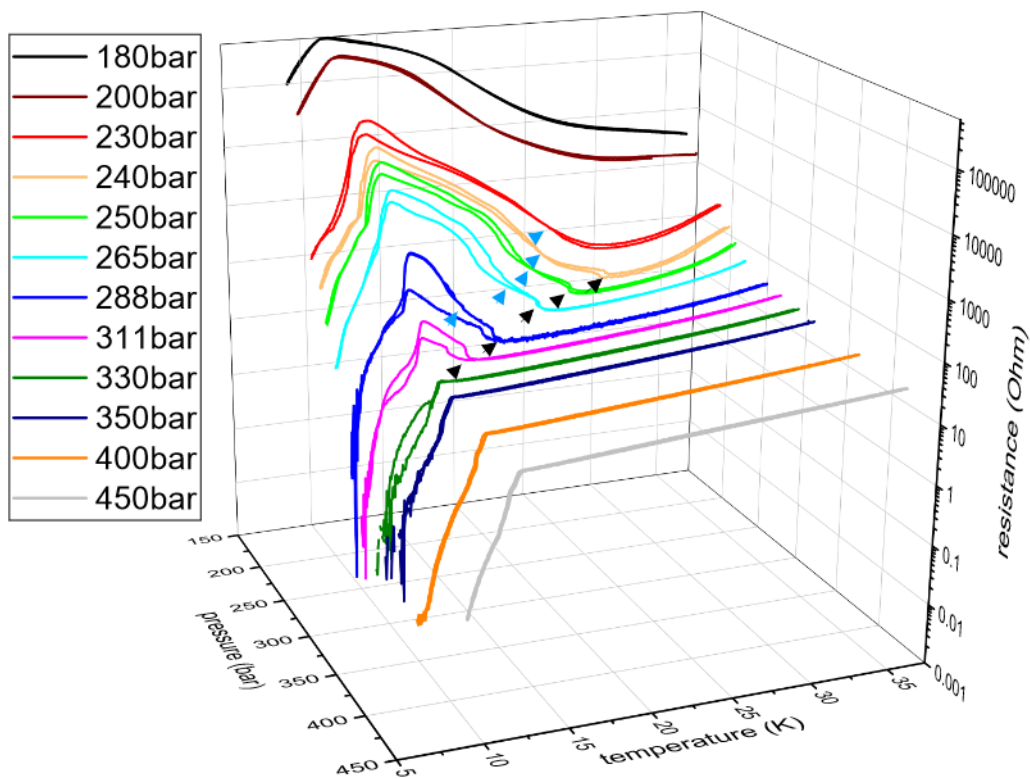
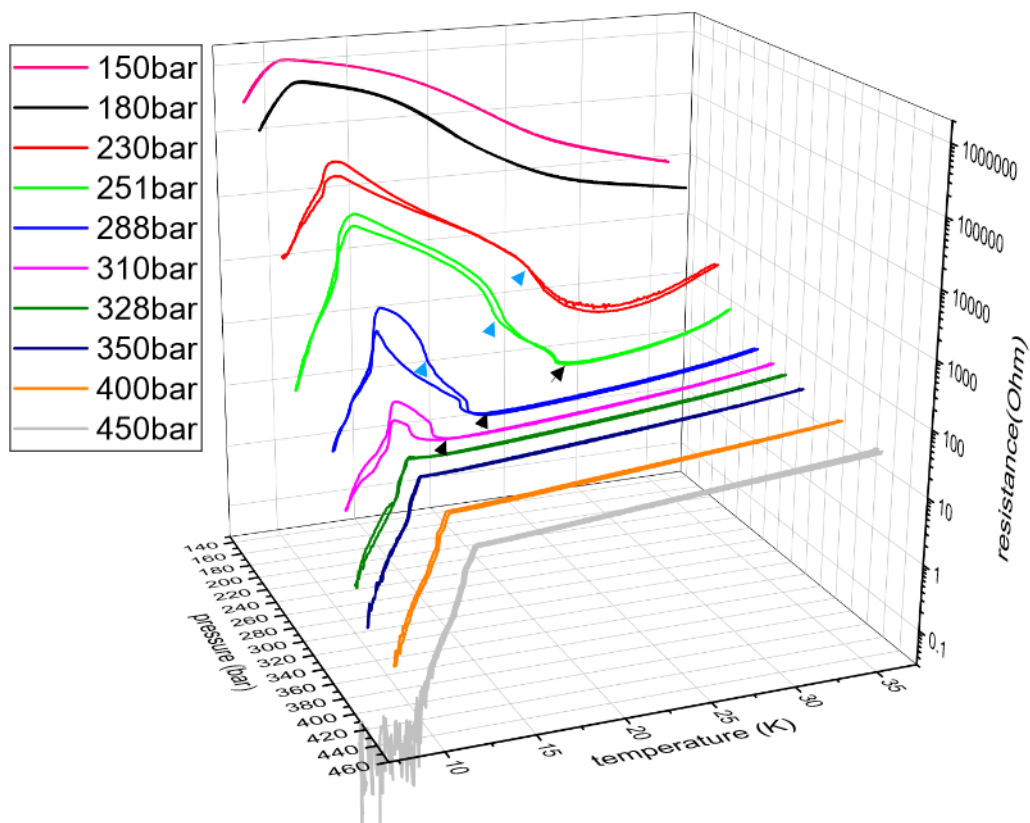


Figure A.6 Resistance over pressure and temperature for sample AFCL3 **Top:** Annealed at 63 K for 50 h. **Bottom:** Annealed at 64.5 K for 24 hours. The arrows in both case indicate steps in the resistance. The arrows in blue indicate where also steps may be read from fig. 5.20. That there are steps is clearer from the figure for the annealed at 64.5 K state. However these features may be also identified for 230 bar, 251 bar and 288 bar for the state annealed at 63 K.

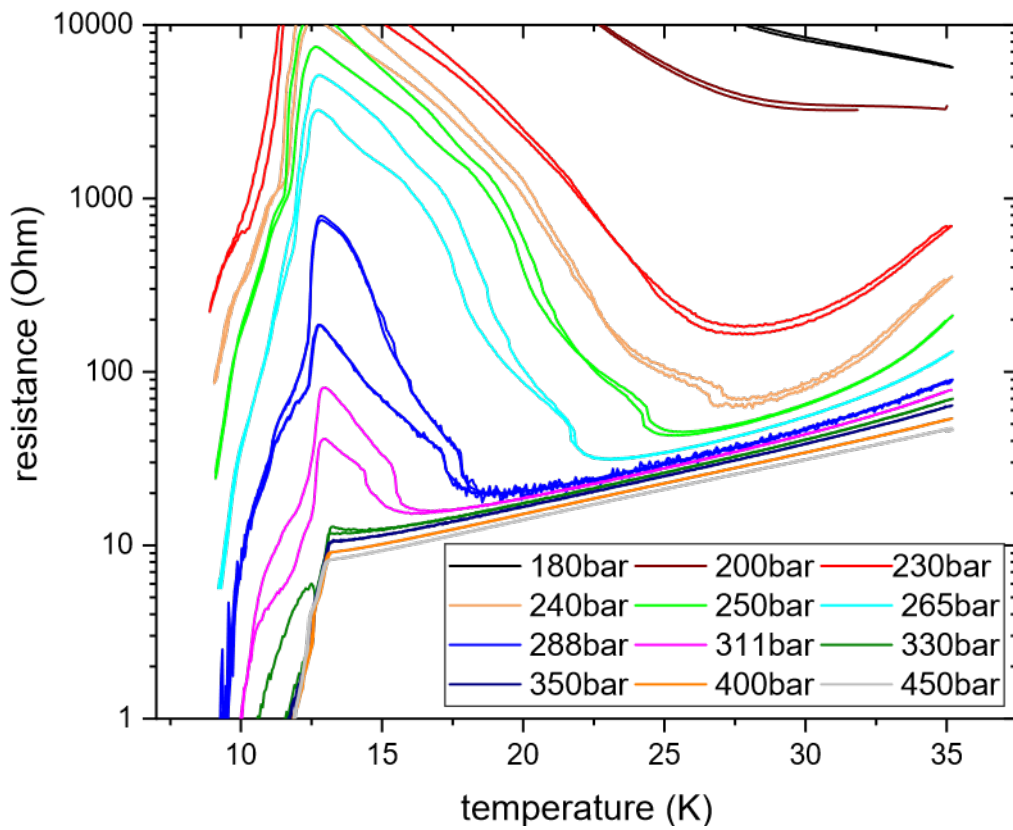
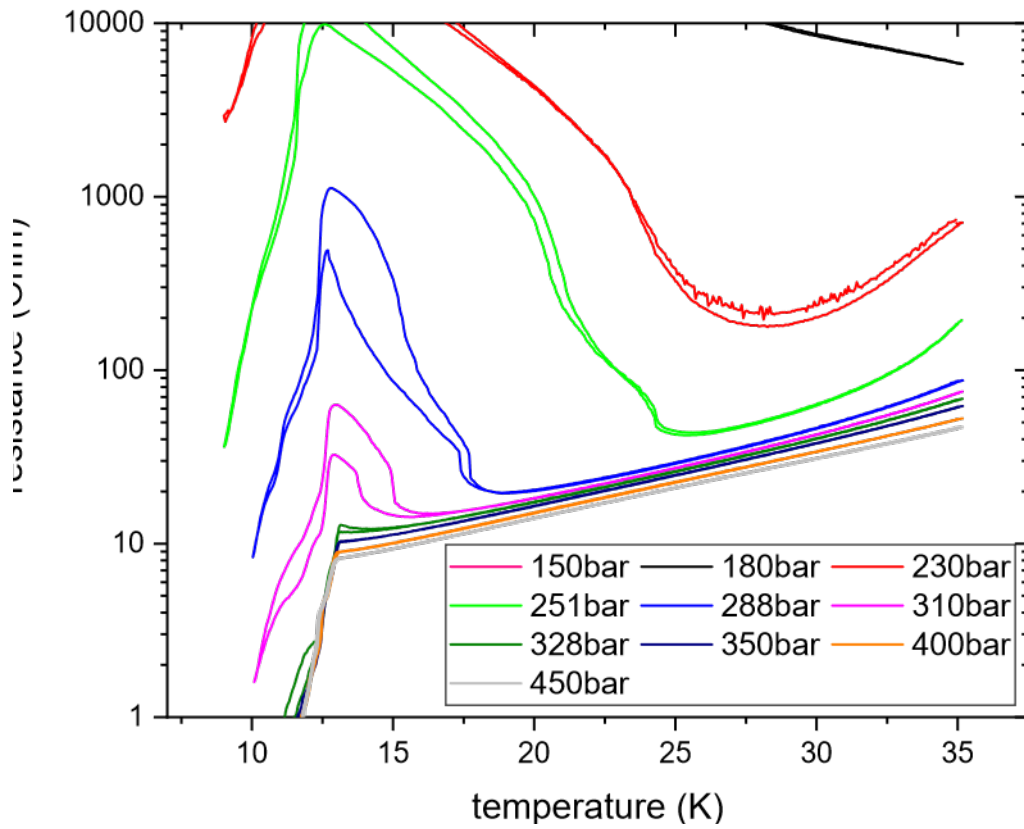


Figure A.7 Resistance over temperature for sample sample AFCL3. **Left:** annealed at 63 K **Right:** annealed at 64.5 K for 50 h. Colouring for each pressure is the same as in fig. 5.19.

Bibliography

- [1] D. Vollhardt. Dynamical mean-field theory for correlated electrons. *Annalen der Physik* **524**, 1–19 (2012). URL <https://onlinelibrary.wiley.com/doi/abs/10.1002/andp.201100250>. <https://onlinelibrary.wiley.com/doi/pdf/10.1002/andp.201100250>.
- [2] V. Dobrosavljević & D. Tanasković. *Chapter 1 Wigner–Mott Quantum Criticality: From 2D-MIT to 3He and Mott Organics* (Taylor and Francis, Registered in England and Wales No. 3099067 5 Howick Place | London | SW1P 1WG, 2017).
- [3] P. A. Lee, N. Nagaosa & X.-G. Wen. Doping a Mott insulator: Physics of high-temperature superconductivity. *Rev. Mod. Phys.* **78**, 17–85 (2006). URL <https://link.aps.org/doi/10.1103/RevModPhys.78.17>.
- [4] G. Rohringer, H. Hafermann, A. Toschi, A. A. Katanin, A. E. Antipov, M. I. Katsnelson, A. I. Lichtenstein, A. N. Rubtsov & K. Held. Diagrammatic routes to nonlocal correlations beyond dynamical mean field theory. *Rev. Mod. Phys.* **90**, 025003 (2018). URL <https://link.aps.org/doi/10.1103/RevModPhys.90.025003>.
- [5] S. Oberbauer, S. Erkenov, W. Biberacher, N. D. Kushch, R. Gross & M. V. Kartsovnik. Coherent heavy charge carriers in an organic conductor near the bandwidth-controlled Mott transition. *Phys. Rev. B* **107**, 075139 (2023). URL <https://link.aps.org/doi/10.1103/PhysRevB.107.075139>.
- [6] P. Limelette, P. Wzietek, S. Florens, A. Georges, T. A. Costi, C. Pasquier, D. Jérôme, C. Mézière & P. Batail. Mott Transition and Transport Crossovers in the Organic Compound κ -(BEDT-TTF)₂Cu[N(CN)₂]Cl. *Phys. Rev. Lett.* **91**, 016401 (2003). URL <https://link.aps.org/doi/10.1103/PhysRevLett.91.016401>.
- [7] X. Su, F. Zuo, J. A. Schlueter, M. E. Kelly & J. M. Williams. Structural disorder and its effect on the superconducting transition temperature in the organic superconductor κ -(BEDT-TTF)₂Cu[N(CN)₂]Br. *Phys. Rev. B* **57**, R14056–R14059 (1998). URL <https://link.aps.org/doi/10.1103/PhysRevB.57.R14056>.
- [8] B. Hartmann, J. Müller & T. Sasaki. Mott metal-insulator transition induced by utilizing a glasslike structural ordering in low-dimensional molecular conductors. *Phys. Rev. B* **90**, 195150 (2014). URL <https://link.aps.org/doi/10.1103/PhysRevB.90.195150>.
- [9] H. D. Weiß. *Fermi Surface Studies on the Organic Superconductor κ -(BEDT-TTF)₂Cu[N(CN)₂]Br and on the Alkaline Earth Subnitride NaBa₂N by means of Magneto-Quantum Oscillations*. Ph.D. thesis, University Konstanz (2001).
- [10] T. F. Stalcup, J. S. Brooks & R. C. Haddon. Temporal processes in a polymeric anion-based organic superconductor. *Phys. Rev. B* **60**, 9309–9312 (1999). URL <https://link.aps.org/doi/10.1103/PhysRevB.60.9309>.
- [11] N. Toyota, J. Müller & M. Lang. *Low-Dimensional Molecular Metals* (Springer Berlin, Heidelberg, Springer-Verlag Berlin Heidelberg 2007, 2007).
- [12] T. Sasaki. Mott-Anderson Transition in Molecular Conductors: Influence of Randomness on Strongly Correlated Electrons in the κ -(BEDT-TTF)₂X System. *Crystals* **2**, 374–392 (2012). URL <https://www.mdpi.com/2073-4352/2/2/374>.

- [13] A. U. B. Wolter, R. Feyerherm, E. Dudzik, S. Süllow, C. Strack, M. Lang & D. Schweitzer. Determining ethylene group disorder levels in κ -(BEDT-TTF)₂Cu[N(CN)₂]Br. *Phys. Rev. B* **75**, 104512 (2007). URL <https://link.aps.org/doi/10.1103/PhysRevB.75.104512>.
- [14] D. Guterding, R. Valentí & H. O. Jeschke. Influence of molecular conformations on the electronic structure of organic charge transfer salts. *Phys. Rev. B* **92**, 081109 (2015). URL <https://link.aps.org/doi/10.1103/PhysRevB.92.081109>.
- [15] J. Müller, M. Lang, F. Steglich, J. A. Schlueter, A. M. Kini & T. Sasaki. Evidence for structural and electronic instabilities at intermediate temperatures in κ -(BEDT-TTF)₂X for X = Cu[N(CN)₂]Cl, Cu[N(CN)₂]Br and Cu(NCS)₂ : Implications for the phase diagram of these quasi-two-dimensional organic superconductors. *Phys. Rev. B* **65**, 144521 (2002). URL <https://link.aps.org/doi/10.1103/PhysRevB.65.144521>.
- [16] K. Sano, T. Sasaki, N. Yoneyama & N. Kobayashi. Electron Localization near the Mott Transition in the Organic Superconductor κ -(BEDT-TTF)₂Cu[N(CN)₂]Br. *Phys. Rev. Lett.* **104**, 217003 (2010). URL <https://link.aps.org/doi/10.1103/PhysRevLett.104.217003>.
- [17] J. Müller, B. Hartmann, R. Rommel, J. Brandenburg, S. M. Winter & J. A. Schlueter. Origin of the glass-like dynamics in molecular metals κ -(BEDT-TTF)₂X: implications from fluctuation spectroscopy and ab initio calculations. *New Journal of Physics* **17**, 083057 (2015). URL <https://dx.doi.org/10.1088/1367-2630/17/8/083057>.
- [18] T. Sasaki, N. Yoneyama, A. Suzuki, N. Kobayashi, Y. Ikemoto & H. Kimura. Real Space Imaging of the Metal-Insulator Phase Separation in the Band Width Controlled Organic Mott System κ -(BEDT-TTF)₂Cu[N(CN)₂]Br. *J. Phys. Soc. Jpn.* **74**, 2351-2360 (2005). URL <https://journals.jps.jp/doi/pdf/10.1143/JPSJ.74.2351>.
- [19] F. Kagawa, T. Itou, K. Miyagawa & K. Kanoda. Transport criticality of the first-order Mott transition in the quasi-two-dimensional organic conductor κ -(BEDT-TTF)₂Cu[N(CN)₂]Cl. *Phys. Rev. B* **69**, 064511 (2004). URL <https://link.aps.org/doi/10.1103/PhysRevB.69.064511>.
- [20] S. Lefebvre, P. Wzietek, S. Brown, C. Bourbonnais, D. Jérôme, C. Mézière, M. Fourmigué & P. Batail. Mott Transition, Antiferromagnetism, and Unconventional Superconductivity in Layered Organic Superconductors. *Phys. Rev. Lett.* **85**, 5420-5423 (2000). URL <https://link.aps.org/doi/10.1103/PhysRevLett.85.5420>.
- [21] D. Fournier, M. Poirier, M. Castonguay & K. D. Truong. Mott Transition, Compressibility Divergence, and the *P-T* Phase Diagram of Layered Organic Superconductors: An Ultrasonic Investigation. *Phys. Rev. Lett.* **90**, 127002 (2003). URL <https://link.aps.org/doi/10.1103/PhysRevLett.90.127002>.
- [22] J. Müller, B. Hartmann & T. Sasaki. Fine-tuning the Mott metal-insulator transition and critical charge carrier dynamics in molecular conductors. *Philosophical Magazine* **97**, 3477-3494 (2017). URL <https://doi.org/10.1080/14786435.2017.1296200>. <https://doi.org/10.1080/14786435.2017.1296200>.
- [23] R. Gross & A. Marx. *Festkörperphysik* (De Gruyter Oldenbourg, Berlin, Boston, 2012). URL <https://doi.org/10.1515/9783110782394>.
- [24] F. Gebhard. *The Mott Metal-Insulator Transition* (Springer Tracts in Modern Physics, 1997).
- [25] J. Hubbard. Electron correlations in narrow energy bands. *Phys. Rev. B* **276**, 238-257 (1963).
- [26] G. W. Scherer. *Relaxation in glass and composites*. A Wiley-Interscience publication (Wiley, 1986).

- [27] K. M. V. High magnetic fields: a tool for studying electronic properties of layered organic metals. *Chemical review* **104**, 5737–5782 (2004). URL <https://pubs.acs.org/doi/pdf/10.1021/cr0306891>.
- [28] A. Abrikosov. *Fundamentals of the Theory of Metals* (North-Holland, Amsterdam, 1988).
- [29] D. Shoenberg. *Other oscillatory effects*. Cambridge Monographs on Physics (Cambridge University Press, 1984).
- [30] W. F. Brinkman & T. M. Rice. Application of Gutzwiller's Variational Method to the Metal-Insulator Transition. *Phys. Rev. B* **2**, 4302–4304 (1970). URL <https://link.aps.org/doi/10.1103/PhysRevB.2.4302>.
- [31] A. Georges, G. Kotliar, W. Krauth & M. J. Rozenberg. Dynamical mean-field theory of strongly correlated fermion systems and the limit of infinite dimensions. *Rev. Mod. Phys.* **68**, 13–125 (1996). URL <https://link.aps.org/doi/10.1103/RevModPhys.68.13>.
- [32] S. Jacob. *Magnetic field effects in the layered organic superconductor $\alpha - (\text{BEDT-TTF})_2\text{KHg}(\text{SCN})_4$* . Master's thesis, Technical University Munich (2007).
- [33] M. Kunz. *Magnetoresistance in the normal and superconducting states of the layered organic metal $\alpha - (\text{BEDT-TTF})_2\text{KHg}(\text{SCN})_4$* . Master's thesis, Technical University Munich (2011).
- [34] D. Andres. *Effects of High Magnetic Fields on a Charge-Density-Wave System*. Ph.D. thesis, Technical University Munich (2004).
- [35] H. R. Schwarz & N. Köckler. *Numerische Mathematik* (Vieweg+Teubner Verlag Wiesbaden, 2009). URL <https://doi.org/10.1007/978-3-8348-9282-9>.
- [36] D. A. Young. Phase diagrams of the elements (1975). URL <https://www.osti.gov/biblio/4010212>.
- [37] S. Oberbauer. *Effective cyclotron mass and electronic properties of κ -phase organic superconductors in the vicinity of the Mott-insulator transition*. Master's thesis, Technical University Munich (2017).
- [38] V. Dobrosavljevic & D. Tanaskovic. Wigner-Mott quantum criticality: from 2D-MIT to 3He and Mott organics. 1602.00131 (2016).
- [39] unknown. Hinweise zur Beurteilung von Messungen, Messergebnissen und Messunsicherheiten (ABW). Material zum Anfängerpraktikum an der Technischen Universität München.
- [40] M. Kund, H. Müller, W. Biberacher, K. Andres & G. Saito. Anomalous thermal expansion of the organic superconductor $\kappa - (\text{BEDT-TTF})_2\text{Cu}[\text{N}(\text{CN})_2]\text{Br}$. *Physica B: Condensed Matter* **191**, 274–280 (1993). URL <https://www.sciencedirect.com/science/article/pii/092145269390085K>.
- [41] M. A. Tanatar, T. Ishiguro, T. Kondo & G. Saito. Nonmetal to metal crossover and ethylene ordering in the organic superconductor $\kappa - (\text{BEDT} - \text{TTF})_2\text{Cu}[\text{N}(\text{CN})_2]\text{Br}$. *Phys. Rev. B* **59**, 3841–3844 (1999). URL <https://link.aps.org/doi/10.1103/PhysRevB.59.3841>.
- [42] B. J. Powell & R. H. McKenzie. Dependence of the superconducting transition temperature of organic molecular crystals on intrinsically nonmagnetic disorder: A signature of either unconventional superconductivity or the atypical formation of magnetic moments. *Phys. Rev. B* **69**, 024519 (2004). URL <https://link.aps.org/doi/10.1103/PhysRevB.69.024519>.
- [43] P. Anderson. Theory of dirty superconductors. *Journal of Physics and Chemistry of Solids* **11**, 26–30 (1959). URL <https://www.sciencedirect.com/science/article/pii/0022369759900368>.

- [44] A. A. Abrikosov & L. P. Gor'kov. Contribution to the theory of superconducting alloys with paramagnetic impurities. *Soviet physics JETP* **12**, 1243–1253 (1961).
- [45] H. Y. Hasegawa. Effects of Randomness on Critical Temperature of Organic Superconductors. *Journal of the Physical Society of Japan* **55**, 3717–3720 (1986).
- [46] O. J. Taylor, A. Carrington & J. A. Schlueter. Superconductor-insulator phase separation induced by rapid cooling of κ -(BEDT-TTF)₂Cu[N(CN)₂]Br. *Phys. Rev. B* **77**, 060503 (2008). URL <https://link.aps.org/doi/10.1103/PhysRevB.77.060503>.
- [47] S. Erkenov. to be disclosed (2024). PhD thesis, Walther Meißner Institut, Garching near Munich, Germany.
- [48] M. Wilde & C. Pfeleiderer. "Lecture notes on Magnetic and Electronic Measurement Techniques" ("2021").
- [49] N. Yoneyama, T. Sasaki, T. Nishizaki & N. Kobayashi. Disorder Effect on the Vortex Pinning by the Cooling-Process Control in the Organic Superconductor κ -(BEDT-TTF)₂Cu[N(CN)₂]Br. *Journal of the Physical Society of Japan* **73**, 184–189 (2004). URL <https://doi.org/10.1143/JPSJ.73.184>. <https://doi.org/10.1143/JPSJ.73.184>.

Acknowledgments

At the end of this thesis I want to thank all the people who helped me accomplish this mater thesis. I want to thank

- Prof. Dr. Rudolf Gross, for giving me the opportunity of doing this thesis
- Dr. Werner Biberacher, who helped me throughout this thesis with many aspects and whose was always available for asking for advice.
- Shamil Erkenov for supporting me, in the lab work as well as in analysing the data and understanding it. I want to thank him as well for the time we had together during this thesis.
- Dr. Mark Kartsovnik, for his supervision
- The workshop and the helium liquifier operators for helping me with the technical challenges that came up during this thesis and for a very precise manufacturing of the needed experimental equipment.
- The technical personal that keeps everything running.
- Sebastian Kammerer for help with the chemical work and nice conversations during breaks.
- Michael Kunz for proof reading
- The master-student office, room 128. Julian Franz, Catharina Broocks, Owen Huisman, Jan Wozniak, Florian Maier, Julias Feigl, Franziska Wilfinger and Georg Maier. For the awesome time and the memes. Your Swedish tea importer.
- All the other PhD students and employees of the WMI for nice conversations, the cake and the memes.
- For providing and synthesizing the samples used in this thesis.
 - Dr. Natalia Kushch from the Institute of Problems of Chemical Physics (Chernogolovka, R.F.)
 - Dr. Harald Müller, European Synchrotron Radiation Facility
 - Dr. H. Schubert (group of Prof. M. Lang), Goete Uni. Frankfurt
 - Peter Christ, WMI – he was a PhD student of W. Biberacher and was most likely assisted in the crystal growth by Werner and by Dr. A. Lorf